UNIVERSIDADE FEDERAL DE ITAJUBÁ
PROGRAMA DE PÓS-GRADUAÇÃO
EM ENGENHARIA ELÉTRICA

Mitigation of Torque Ripple and Vibration in Switched Reluctance Motor Drives: A Switching Optimization

Marcio Luiz Magri Kimpara

Itajubá, November 2018

MITIGATION OF TORQUE RIPPLE AND VIBRATION IN SWITCHED RELUCTANCE MOTOR DRIVES: A SWITCHING OPTIMIZATION

by

Marcio Luiz Magri Kimpara

A Thesis
Presented to
the Faculty of
The Federal University of Itajubá

in Partial Fulfillment
of the Requirements
for the Degree of

DOCTOR IN
ELECTRICAL ENGINEERING

Area: Automation and Industrial Electric Systems

Advisor: Prof. Dr. Luiz Eduardo B. da Silva

Co-advisor: Prof. Dr. João Onofre P. Pinto

November 2018
Itajubá - MG, Brazil

ACKNOWLEGDMENTS

First of all, I would like to thank God, the greatest supervisor of my life.

I also wish to take this opportunity to thank all my family for their support, care and love during all the challenges I've faced, including this research. They are a constant source of motivation and encouragement.

I owe my heartfelt thankful to my lovely wife. She has been a special person in my life from who I find daily inspiration. Without her constant support, motivation and love, I would not go that far. Thank you for being my partner.

I wish to express my deep sense of gratitude and indebtedness to my academic advisors, Dr. Luiz Eduardo Borges da Silva and Dr. João Onofre Pereira Pinto for provide great support in the course of this research and for belief in me. Your efforts and insightful guidance are hereby acknowledged.

Also, I would like to express my sincere gratitude and admiration to Dr. Babak Fahimi. He has been encouraging and guiding me throughout the time I stayed in the University of Texas at Dallas. His knowledge is an outstanding contribution. I also appreciate all the help from the REVT members.

I could not miss to mention my friends, professors and colleagues from BATLAB. It is always a pleasure be in the presence of such nice people like in this group. Your friendship is hereby acknowledged.

I am also thankful to the institutions Federal University of Itajubá, Federal University of Mato Grosso do Sul, University of Texas at Dallas and, in general, to the Brazilian society.

Finally, thanks to all committee members for their valuable comments and contributions.

DEDICATION

Dedicated to my parents Luiz and Aparecida,

my brother Everson, my sister Luciana,

and to my dear spouse Renata...

... *"The greater our knowledge increases the more our ignorance unfolds"*

(John F. Kennedy)

MITIGATION OF TORQUE RIPPLE AND VIBRATION IN SWITCHED RELUCTANCE MOTOR DRIVES: A SWITCHING OPTIMIZATION

Marcio Luiz Magri Kimpara

ABSTRACT

Supervising Professor: Luiz Eduardo Borges da Silva, Dr.

Switched reluctance motor (SRM) drives represents an attractive solution for industrial, transportation and domestic applications due to their rugged structure, independence from rare earth metals, modular design, wide speed range, and tolerance to harsh environments. Despite these advantages, the adequacy of SRM drives for many applications has been overshadowed by its relative high levels of torque pulsation and vibration/acoustic noise.

This research aims to investigate and propose control strategies to mitigate these adverse features. To reach this goal the current shaping and switching optimization have been proposed. Two modeling methods were used in this process: i) field reconstruction method (FRM) to model the electromagnetic behavior; and ii) mechanical impulse response to model the structural behavior. This two-modeling procedure are the key innovative tools in this dissertation, since those are techniques recently proposed in the literature. Moreover, these two methods have been combined to simultaneously mitigation of torque ripple and radial vibration.

Firstly, the structural vibration was investigated in detail for an 8/6 SRM. The modal analysis is carried out experimentally and through finite element model in ANSYS. Then, the mechanical impulse response concept was applied to develop a vibration prediction model that, after validated, was introduced in an optimization algorithm developed in MATLAB to design the precise switching instants to have active vibration cancellation. The method is focused on SRM operating under current control (low speed region). The experimental results show a significantly reduction. This technique is sensitive to timing without adverse impact on productivity and efficiency of the SRM drive. Moreover, the vibration mitigation also has contributed to acoustic noise reduction.

In a second approach, an optimization based on the SRM model using the FRM is used to find the optimal current profile that mitigates the torque ripple. The percentage reduction reached is about 44%. Furthermore, the effect of the new current profile in the structural response is also investigated and a negative impact in the vibration has been observed. To deal with this shortcoming, an adaptive hysteresis band is implemented over the optimized current profile for torque ripple mitigation. The obtained results demonstrated a good compromise between the torque ripple and vibration mitigation.

List of Figures

VI

VIII

List of Tables

Table of Contents

Chapter 1

Introduction

Electric motors have a wide array of applications and can be found practically everywhere. Moreover, there are different types of motors, which are normally classified by the power supply, type of motion, the principle of energy conversion, among other features. Therefore, there are many aspects to consider when selecting the appropriate motor for a specific application. Type of load, operational requirements, investment, mechanical, and environmental issues are some examples. Furthermore, in many situations a trade-off must be considered, and an equilibrium established between many factors in defining the suitable motor.

The applications involving adjustable speed drives demand technologies that result in a reliable and high-performance operation. In this field, permanent magnet (PM) motors are treated as a good candidate. This type of motor has high power density due to presence of permanent magnets, but its speed range is limited by the flux weakening capability. Additionally, it depends on rare earth metals and the magnets can be demagnetized under certain conditions. Induction motors (IM) are also suitable due to its robust structure and low cost. Nonetheless, power density is a shortcoming compared to PM motors.

Therefore, switched reluctance motors (SRM) are receiving renewed attention as a potential candidate for modern applications due to its attractive features, such as robustness, power density, wide speed range, fault tolerant ability, high efficiency, low cost and suitable conditions for operating in harsh environments. Indeed, commercial pumps, compressors, automotive applications and home appliances such as washing machines and vacuum cleaner are already available. However, despite the SRM advantages, the adequacy of SRM drives for many applications has been overshadowed by its relative high torque pulsation and vibration/acoustic noise levels, considered the primary disadvantages of this motor.

Reluctance machines are one of the earliest electric machines which were developed, however, in a first glance, the limitations of the power electronics devices restricted the widespread use of this motor in industry applications. Recently, with modern power electronics and microcontrollers devices, many researchers have been focused on improving the SRM adverse features to encourage the disseminate usage of this machine.

Therefore, in this research, new control strategies are proposed for SRM drives aiming to reduce the torque oscillation and the induced vibration to acceptable levels. These new control methods are based on switching approach, giving rise to an optimized excitation current profile. To reach this goal, the torque ripple production and the vibration phenomena are studied by means of two models: i) the electromagnetic model based on the field reconstruction method and; ii) the vibration prediction model, based on the mechanical impulse response. These models are the key innovative tools that establish a link between the electrical excitation and the torque ripple generation; and the electrical excitation and vibration, respectively.

The analysis and claims of this research will be verified through multi-physics finite element and experimentation. The simulations and computational analysis have been conducted in ANSYS package. The experimental tests are carried out on a 4-phase 8/6 SRM.

1.1   Research Motivation and Objectives

With growing industry interest in switched reluctance machines, extensive research is being conducted on its design and control. Many researchers have been focused on mitigate the inherent operation issues, such as vibration and torque ripple. As reported in the state of art section of Chapter 2, insightful contributions have been proposed in the design and control of SRM and, although improvements in certain performance extent have been achieved, the problem has not been solved completely. With the continuous progress of control technology, the better torque ripple or vibration suppression are to be proposed. Thus, the motivation of this work is to propose new approaches in solving the SRM drawbacks.

An electric machine can be viewed as a current to torque transducer, thus the torque ripple effects can be minimized by a properly current excitation. The investigation of torque ripple mitigation in this research follows this perspective. Also, SRMs still require further efforts in order to reduce the acoustic noise and the vibration. Previously, active vibration cancellation techniques demonstrated success in reducing the vibration and acoustic noise, however, these methods are either limited to high speed region. Hence, the hereby proposed method to suppress the stator vibration is motivated in finding a solution for low speed operation, under current chopping control.

Moreover, after going through a comprehensive review of previous work it was found that very few multi-objective improvements have been developed. Therefore, this research is also motivated to develop a combined optimization procedure to outcome with a current profile able to simultaneously reduces torque pulsation and induced vibration.

Thus, although the earliest concept on switched reluctance motors dates back to the 19th century, the majority of its development is recently. Yet, there is room for technical advances.

The main objectives of this dissertation research are:

- Propose new switching strategies to address the pulsating torque and vibration issues in SRM;
- Improve the performance of SRM and extend its applications in industry;
- Apply the field reconstruction method concepts to develop a fast and precise model for electromagnetic flux and force calculation in SRMs;
- Propose and test an optimal excitation current profile that allows the SRM to operate at reduced torque ripple;
- Investigate the vibratory behavior of the SRM;
- Explore the mechanical impulse response to develop a vibration prediction model;
- Propose a current switching pattern that incorporates the active vibration cancellation aiming to suppress the stator vibration and reduce the emitted acoustic noise at low speed region;
- Propose an excitation profile that simultaneously mitigates the torque pulsation and stator vibration, reaching a satisfactory level in these parameters;
- Contribute to create conditions for insertion of SRM in sensitive applications;

1.2   Dissertation Organization

The dissertation starts with an introduction where a brief contextualization regarding switched reluctance motors has been presented. The motivation and objectives of the current research work is also covered in this first chapter. Chapter Two presents the literature review regarding the SRM. It includes the principle of operation and governing equations, the main drive topology, operation modes and control strategies. The chapter ends with the state of art covering some optimization procedures and achievements reported in the literature.

In Chapter Three, the SRM characteristics and modeling are discussed. The flux linkage, static torque and inductance profile are obtained experimentally. Then, A 2D finite element model is developed in software ANSYS and used to perform magneto-static solutions used in the development of a more effective model based on the field reconstruction method (FRM). The 2D models is also extended to its 3D version for structural analysis purpose.

Chapters Four and Five are the bulk of this research. Chapter Four covers a comprehensive vibration analysis. It starts with the natural frequencies and mode shape investigation. Then, the impulse response method and the vibration prediction model are described. The prediction model is validated and applied to an optimization algorithm to outcome with an alternative active vibration cancellation strategy. Experimental verification is conducted to assess the effectiveness of the proposed method for different operation points. In Chapter Five the torque ripple is addressed. An optimization process is proposed to shape the excitation current that results in a smoothly torque profile. The FRM is applied in this iterative routine due to its computational time efficiency. Simulation results are demonstrated through a co-simulation model in ANSYS/Simplorer. Experimental tests also confirm the improvements in the generated torque. In the end of the chapter, the effects of the new current shape in the structural response is investigated and a method to simultaneously mitigate the torque ripple and the vibration/acoustic noise based on an adjustable hysteresis band has been proposed. Chapter Six is the final chapter presenting the conclusions, primary contributions from this research and suggestions for future research work.

Chapter 2

Literature Review

This chapter provides a basic background regarding switched reluctance machine. A brief history, description of constructive aspects, the fundamentals on the principle of operation and governing equations are presented. In addition, the basic converter drive and the operational characteristics of the switched reluctance motors are also covered. At the end of this chapter a state-of-the-art with respect to the recent findings in the SRM design and control, is also discussed.

2.1 Concerning SRM

Reluctance motors are considered as a subcategory of synchronous motors with a salient-pole rotor. They differ from other types of motors, since their rotor does not carry any windings or permanent magnet. The guiding principle behind the SRM is based on a doubly salient structure and the alignment tendency between stator and rotor poles, i.e. by exciting a stator coil, the rotor will move towards a position where reluctance is to be minimized.

The scientific knowledge of physical principles governing the operation of SR motor can be traced back to 1838, however at that time the first experiments faced serious limitations due to inadequate switches and poor electromagnetic and mechanical design [1], [2]. As a result, the reluctance machine was quickly overcome by induction and DC machines whose implementation challenges were clearly lower since these machines can be feed directly from the power supply. Hence, SRM drives were not competitive and they faded into the background. Only after the evolution in the field of power electronics, including the advent of more reliable, high-power and affordable semiconductor devices, it has been possible to develop the drive system and thus "reinvent" the SRM [3].

Early evolution of reluctance motors led to two different types: switched and synchronous reluctance motors. In a recently past, the progress in switched reluctance motor developments and applications has been fairly active. This interest has been primarily due to the potential applications in variable speed drives for industrial, domestic consumers and in the

emerging market of electric vehicles. Figure 2.1 depicts some milestones in the SRM development and evolutionary application [1], [2], [4], [5], [6].

Figure 2.1. Evolutionary timeline.
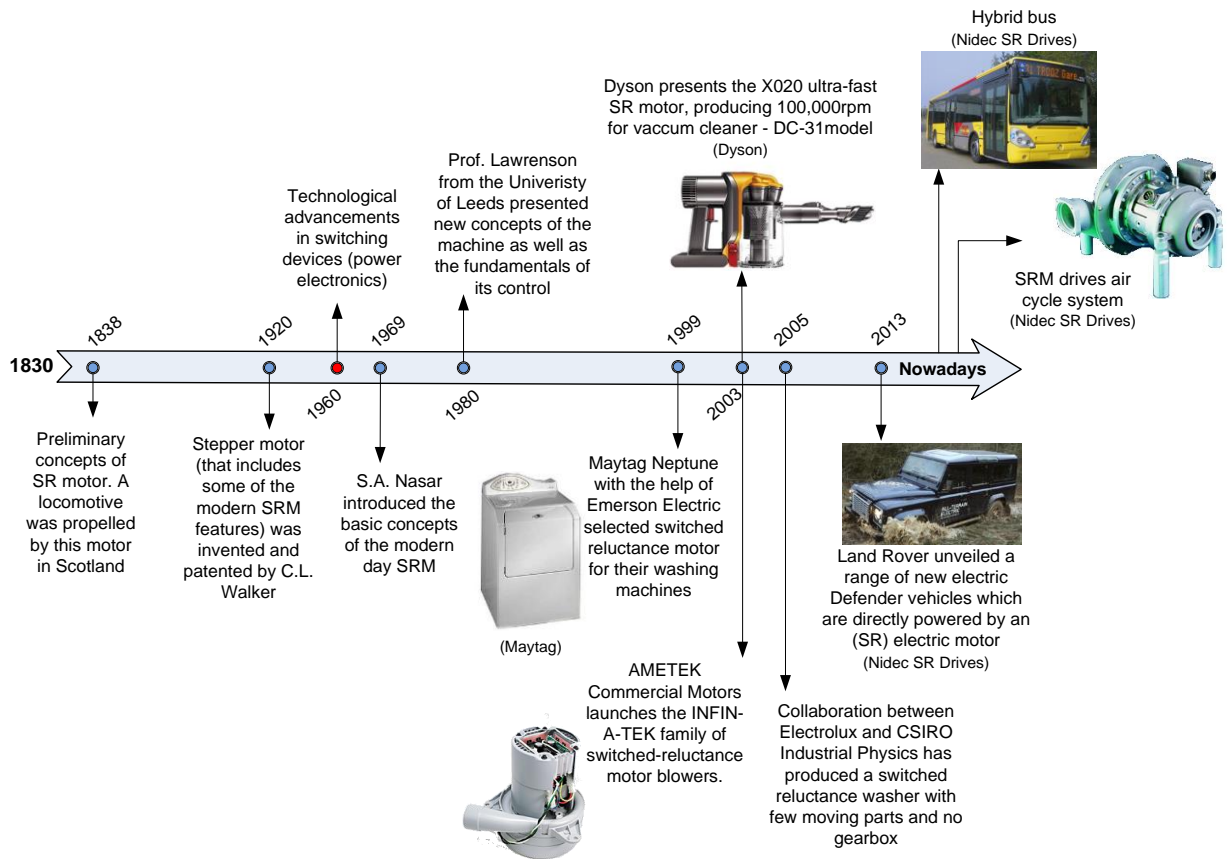
Indeed, SRM presents desired and more attractive characteristics than these of other traditional motors. High efficiency, low cost, wide speed range, robustness and suitable conditions for operating in harsh environments are some examples [7]. However, SRM also suffers from some demerits, namely, torque ripple and high levels of vibration/acoustic noise. These shortcomings are inherence features on account of the principle of operation, however, many researchers have been contributed in design and control of SRMs aiming to improve its performance.

Constructively, the switched reluctance motor has a double salient structure, i.e. both the stator and rotor magnetic circuits have salient poles. The number of saliencies on the stator and rotor can vary and different combinations are possible, however, it is essential to machine operation that the number of rotor and stator poles be different. The most common configurations are 6/4, 8/6 and 12/10, where the first digit refers to the number of saliencies in

the stator and the second digit denotes the number of saliencies in the rotor. Figure 2.2 illustrates different possible arrangements for the SRM. The stator has windings concentrated around the saliencies, while the rotor is totally passive, having no type of winding or permanent magnet. In the stator, each pair of diametrically opposed poles constitutes a phase. Thus, the SRM can be manufactured with single, two, three, four or even having more than four phases.

The rotary movement of this motor is due to the tendency of alignment between the poles of the stator and the rotor in order to obtain minimum reluctance for the magnetic flux. Further details on its elementary operation will be cover in the next section.

Figure 2.2. SRM stator and rotor pole configurations. (a) 6/4. (b) 8/6. (c) 10/8.

| (a) | (b) | (c) |
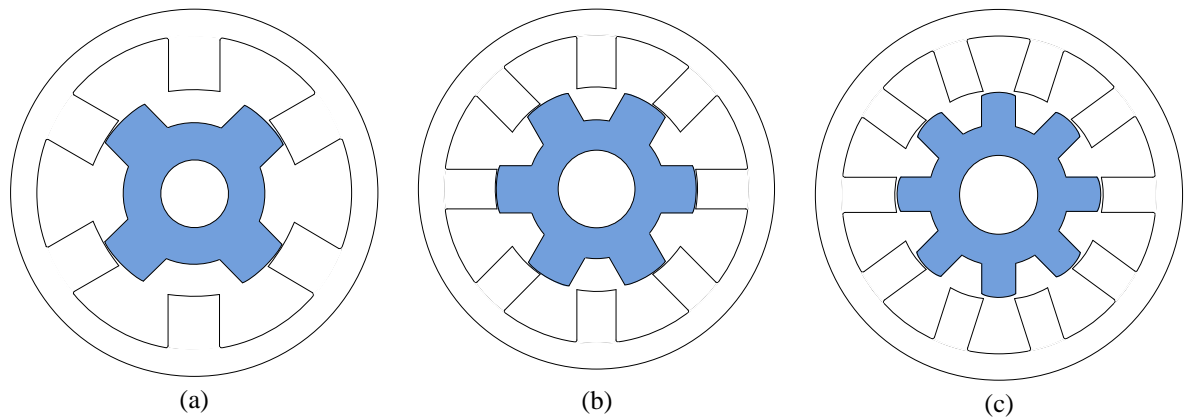
This electric machine received this nomenclature because the rotor movement is achieved by switching the excitation between stator phases and due to the variable reluctance as the rotor moves. The SRMs can also be classified into rotational or linear categories [3]. Among the rotational type it is still possible to classify them between axial field or radial field as shown in Figure 2.3. In this work the study is carried out based on a rotational radial flux 8/6 SRM.

Figure 2.3. SRM classification.
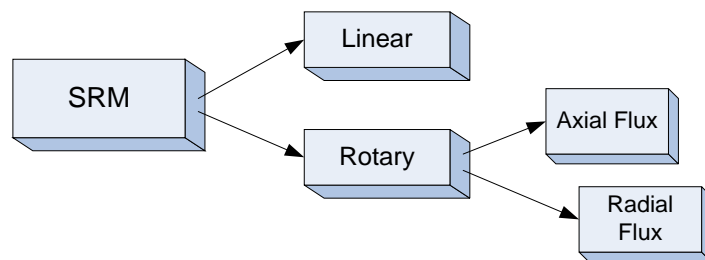
Adapted from [3].

2.2 Fundamentals of SRM operation

The operation of the switched reluctance motor is relatively simple. Consider at a first glance that the position of the rotor is such that the poles *r1* and *r*1' are aligned with the stator poles *c* and *c'* as shown in Figure 2.4(a). Applying current in phase A of the stator, the flux shown in Figure 2.4(b) is established through the poles *a* and *a'* of the stator and by *r2* and *r2'* in the rotor, which tends to move the rotor to the position of alignment with phase A, as illustrated in Figure 2.4(c). When it reaches this new position, the current applied to phase A must be extinguished and the excitation applied to phase B causing the poles *r1* and *r1'* to align with *b* and *b'* [3]. Similarly, the subsequent excitation of phase C will lead to the alignment of *r2* and *r2'* with *c* and *c'*. Thus, by applying excitation sequentially to the stator windings, the continuous rotational motion is obtained.

Figure 2.4. Elementary operation. (a) Rotor poles aligned with phase C of stator. (b) Flux lines when phase A is excited. (c) Rotor poles aligned with phase A of stator.

(a)   (b)   (c)
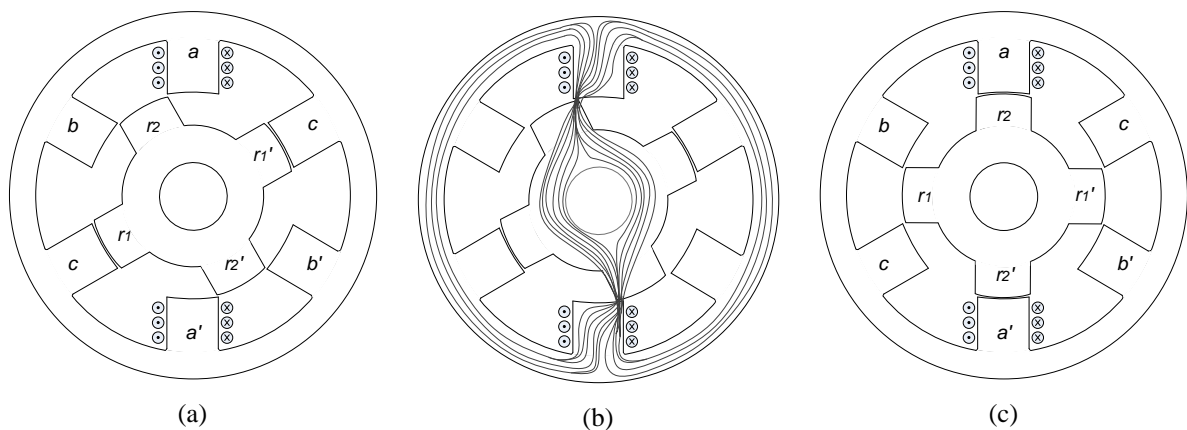
Adapted from [3].

The above explanation is given based on a 6/4 SRM, however other configurations have the same principle. The definition of the number of poles affects the number of converter legs, the drive cost and control complexity, and torque oscillation. Incrementing the number of stator poles, the cost of the drive increases due to the increase in the number of semiconductor devices. Likewise, increasing the number of rotor poles, the losses in the core increases due to a higher switching frequency between stator phases excitation [8].

For a complete revolution, the excitation current must be switched between phases as many times as the number of saliencies in the rotor. For instance, on the 8/6 motor, for a complete mechanical turn, 6 switching sequences between the phases (6 poles in the rotor) are

required. It means that after 1 sequence, the rotor moves 60° (360°/6). As the motor has 4 phases, each phase remains energized for 15° (60°/4). This is known as stroke angle and measures the maximum dwell angle without overlap (single-phase excitation):

$$\theta_{ST} = \frac{360}{q \cdot N_r} \tag{2.1}$$

where q is number of phases and N_r stands for number of protuberances in the rotor.

Based on that, one can note that the switching sequence between the SRM phases depends on the rotor position, thus it is essential to have this information in the drive control. The presence of a position sensor adds complexity and costs to the system, therefore same sensorless control methods have been proposed in the literature.

The torque production in the SRM can be explained by its magnetization characteristic. Due to the constructive aspect of this motor, there is a nonlinear relationship between flux/torque, rotor position and excitation current. As the rotor moves, the inductance in each phase of the stator follows a cyclic variation. The variation of the self-inductance in one of the stator phases as a function of rotor position is shown in Figure 2.5. As illustrated, the inductance profile can be divided into four well defined regions. In the first region, between 0 and θ_1, the stator and rotor poles are misaligned and not overlapping. In this range, the flux path is predominant the air, giving rise to a minimum inductance value (L_u). Furthermore, the inductance is practically constant in this region.

The second region starts from position θ_1 in which the rotor pole starts to overlap the stator pole providing a path for the flux through the magnetic material. Hence, the inductance increases with the rotor position, ranging from the minimum value L_u to a maximum value (L_a), obtained when the rotor reaches the position θ_2 at which the overlap between the poles is complete. The small interval between the positions θ_2 and θ_3 defines the third region. In this region, the rotor motion does not change the alignment condition between the rotor pole and the stator pole, which maintains the flux predominantly by the magnetic material and therefore the inductance remains constant at the maximum value (L_a).

Finally, in the fourth region the rotor is moving towards the direction of misalignment with respect to the excited phase, i.e., leaving the overlapping between the poles. As a result, there is a decrease in the inductance due to the flux variation. The inductance decreases from its maximum value L_a to the minimum value L_u.

The inductance profile shown in Figure 2.5 is only theoretical. In practice it is not possible to achieve this ideal shape due to saturation. The saturation effect causes a curve near

the top of the inductance profile, which decreases the torque constant [3]. Moreover, some SRMs do not have third zone. That happens when the stator pole and rotor pole are designed with the same arc.

Figure 2.5. Inductance profile for one stator phase in relation to rotor position.
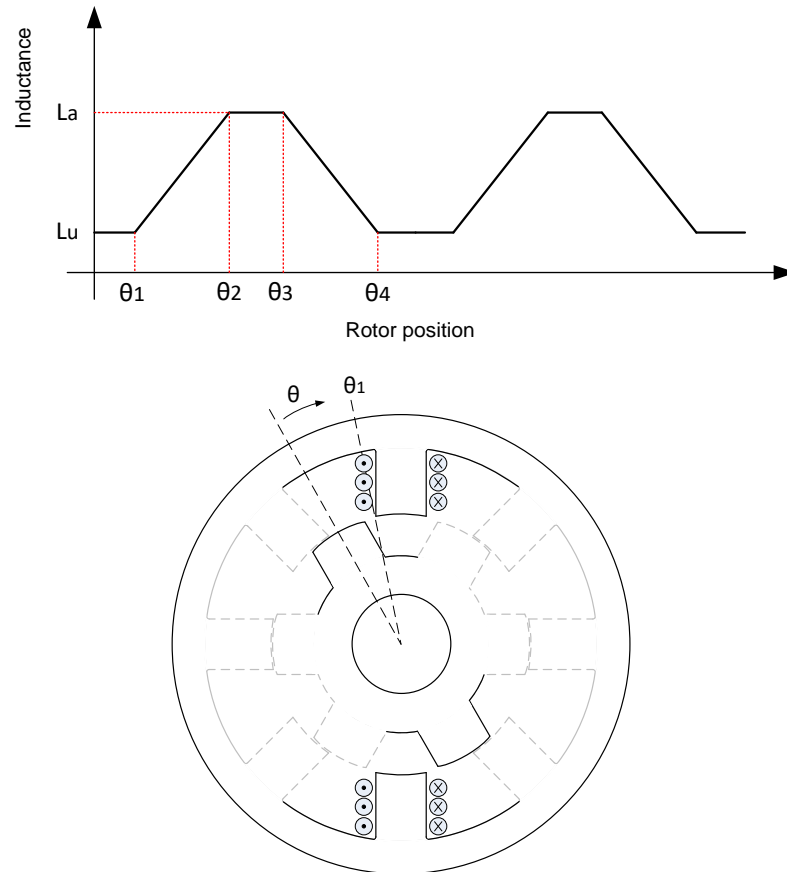
2.3 Mathematical equations governing SRM

The formulation that follows is based on the description presented in [3]. As the SRM phases are excited individually, we can neglect the mutual inductance between the phases. Thus, we have that the voltage applied to the phase is equal to the sum of the drop in the winding resistance and the variation in the linkage flux, as described by equation (2.2):

$$V = R.i + \frac{d\lambda}{dt} \tag{2.2}$$

where R denotes the phase resistance and λ is the flux linkage, calculated as (2.3):

$$\lambda = L.\,i \quad \Rightarrow \quad \lambda = L(\theta, i).\,i \tag{2.3}$$

where L is the inductance, which depends on the rotor position θ and phase current i.

Replacing (2.3) in (2.2), yields:

$$V = R.\,i + \frac{d(L(\theta, i).\,i)}{dt} \tag{2.4}$$

Appling the derivative rule:

$$V = R.\,i + \frac{d(L(\theta, i))}{dt}.\,i + L(\theta, i).\frac{di}{dt} \tag{2.5}$$

Multiplying all the terms of equation (2.5) by the current, results in the expression for the input power:

$$P_{input} = V.\,i = R.\,i^2 + \frac{d(L(\theta, i))}{dt}.\,i^2 + L(\theta, i).\,i.\frac{di}{dt} \tag{2.6}$$

The last term on the right-hand side of equation (2.6) is physically non-interpretable; so, we can rewrite it in terms of known variables as in (2.7) in order to extract a meaningful inference [3]:

$$\frac{d}{dt}\left(\frac{1}{2}.\,L(\theta, i).\,i^2\right) = L(\theta, i).\,i.\frac{di}{dt} + \frac{1}{2}.\,i^2.\frac{d(L(\theta, i))}{dt} \tag{2.7}$$

Substituting (2.7) into the power equation, we have:

$$P_{input} = R.\,i^2 + \frac{d}{dt}\left(\frac{1}{2}L(\theta, i).\,i^2\right) + \frac{1}{2}.\,i^2.\frac{d(L(\theta, i))}{dt} \tag{2.8}$$

Analyzing equation (2.8), one can identify already known terms in electromechanical systems, that is, the input power is equal to the sum of the resistive loss in the winding, the rate of change of energy and the power in the air gap.

The variable transformation $t = {\theta}/{\omega_m}$, gives:

$$P_{airgap} = \frac{1}{2}i^2\frac{d(L(\theta, i))}{dt} = \frac{1}{2}i^2\frac{d(L(\theta, i))}{d\theta}.\frac{d\theta}{dt} = \frac{1}{2}i^2\frac{d(L(\theta, i))}{dt}.\,\omega_m \tag{2.9}$$

As the power in the air gap is the product of the electromagnetic torque by the mechanical speed, we have:

$$P_{airgap} = T_e \cdot \omega_m$$

(2.10)

Combining (2.9) and (2.10), the equation for torque is defined as:

$$T_e = \frac{1}{2} i^2 \frac{d\big(L(\theta, i)\big)}{d\theta}$$

(2.11)

Considering the torque equation represented in (2.11) one can refer back to the inductance profile to conclude that:

- In region one, the L_u inductance is constant, therefore there is not torque generation.
- In the second region, the inductance is rising, hence the excitation current applied to the stator phase produces positive torque.
- In the third region the inductance is constant in its maximum value L_a. Since there is no inductance variation, the torque generated in this region is zero. This is known as dead zone.
- In region four, inductance is decreasing. This negative slope produces negative torque if phase excitation is applied.

In summary, the complete alignment represents the stable position for the set while the misalignment region represents a position of instability. Both regions do not produce torque since there is no inductance variation. The positive inductance slope is the region in which the phase must be excited to produce positive torque - motor mode. The inductance decreasing region produces negative torque and is used for braking or generator mode. At this point it is also opportune to observe that: when operating in motor mode, the region 3 in which there is no torque production is the appropriate time to extinguish the current from the stator phase, preventing the generation of negative torque in part of the time if the current is still decaying (current tail) in the region where the inductance decreases.

2.4 Operational Characteristics

The definition of the best electric machine is far from a unified agreement and has motivated a wide and hot discussion. Several factors should be considered. Based on the

constructive characteristics and operating principle described in the previous sections, it is possible to highlight some particular characteristics of SRM:

1) The torque is proportional to the square of the current, which allows to operate with unidirectional currents. This characteristic allows to adopt converters with only 1 semiconductor per leg, helping to reduce the costs of the drive [3];

2) The torque constant is given by the inductance slope versus rotor position. The inductance of the stator windings is a function of both, rotor position and the applied current, which outcomes with a strong non-linear relationship [3];

3) The torque produced by the SRM is proportional to the square of the current. This provides high starting torque, without the problem of excessive inrush currents, as for example the large starting current of induction motors. It is an important requirement for traction applications [3];

4) Alternating the rotation direction can be easily accomplished by simply changing the excitation sequence of the stator phases;

5) The torque has the signal controlled by the inductance variation (dL/dt). Operation as a generator is possible as long as the motor is operated on the inductance descent ramp. Indeed, due to this and other characteristics, the motor can operate easily in the 4 quadrants [3];

6) This motor requires a controlled converter and cannot be operated directly from an alternating or continuous power supply. The dependence of the converter makes it suitable to variable speed applications. For applications involving constant speed, SRM is more expensive compared to the induction motor [3];

7) Regarding variable speed drive, the switched reluctance motor has the same components used for other motors, namely, input source, rectifier, converter and controller. Figure 2.6 shows a typical diagram for SRM drive system. From the converter it is required the ability to apply current to the windings of the motor in well-defined intervals of time. The extrapolation of these intervals leads to an increase in the oscillations of the torque and consequently loss of efficiency [9], besides the possibility of entering the generator region;

8) The magnetic circuit of the machine is symmetrical and the mutual inductance between stator phases is very small and can be ignored for practical purposes. Without this mutual coupling, it can be said that the phases are electrically independent, and a possible short-circuit in one phase

will not affect the others. This feature provides higher fault-tolerant ability, compared to other motors [8].

9) This motor operates at a wide speed range. Disregarding the mechanical limitations, the speed of this motor is not limited by the geometry of the machine, but by the frequency switching of the drive converter [8].

10) By increasing the number of poles in the rotor it is possible to decrease the torque oscillation. On the other hand, it produces a lower ratio between the maximum and minimum values of the phase inductance, decreasing the output specifications [9]. By increasing the number of phases, it is possible to reduce the torque pulsation without decreasing the inductance ratio, but the number of switching devices employed in the drive circuit and consequently the cost will be increased. At least two phases are required to guarantee the self-starting. At least three phases are required in order to ensure the starting direction. Motors with only 2-pole (single-phase) exist, however these have no ability to start depending on the position of the rotor. Thus, permanent magnets must be positioned inside the machine in order to allow them to start.

11) The simplicity combined with the reduction in the volume of copper due to the short pitch of the coils (concentrated winging) in the stator and absence of winding in the rotor contributes to the reduction of the manufacturing cost of this one machine [10]. It also helps in the power density.

12) It has a robust structure. Rotor is especially simple and requires few manufacturing steps.

13) SRM can be found in the range of a few Watts to MWatts. The lifetime is higher due to the lower temperature since the rotor circuit does not present Joule losses. It is, therefore, a highly efficient motor [11].

14) The lower internal temperature and absence of commutation sparks extend the applications for this motor to harsh environments. Moreover, because there are no magnets the maximum permissible rotor temperature may be higher than in PM motors;

15) The rotor is simple and requires relatively few manufacturing steps; it also tends to have a low inertia [1];

Figure 2.6. SRM drive components.
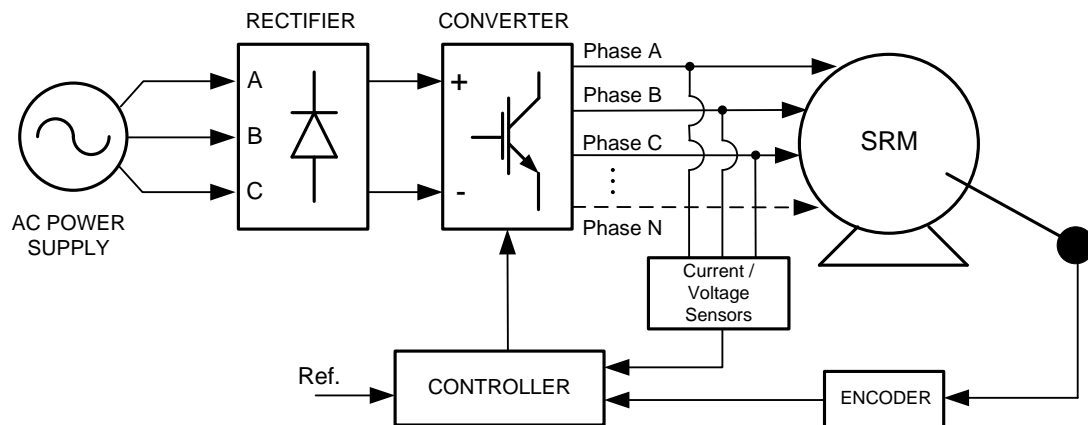
2.5   Converter Topology

In order to obtain a continuous rotational movement, SR machines utilize a power converter to commutate the phase excitation. Moreover, the torque is produced regardless the direction of the current flowing through the phase windings, which permits the use of only one switching device per phase. However, since the mutual coupling between phases is almost negligible, stored magnetic field energy can create problem during commutation of a phase. Therefore, the stored magnetic field energy must flow through a path during commutation, otherwise excessive voltage can be developed across the winding and may result in the failure of the semiconductor switch connected in series with the winding [8].

Many different power circuit configurations have been designed for SRM drives. Split-capacitor converter, variable DC link Buck converter, R-dump and C-dump are some examples [1], [3]. Nonetheless, the most flexible and popular SRM converter is the asymmetric bridge converter shown in Figure 2.7, which requires two switches and two diodes per phase. This converter provides independent control for each phase and consequently, overlapping operation can be easily implemented.

Figure 2.7. Asymmetric bridge converter.
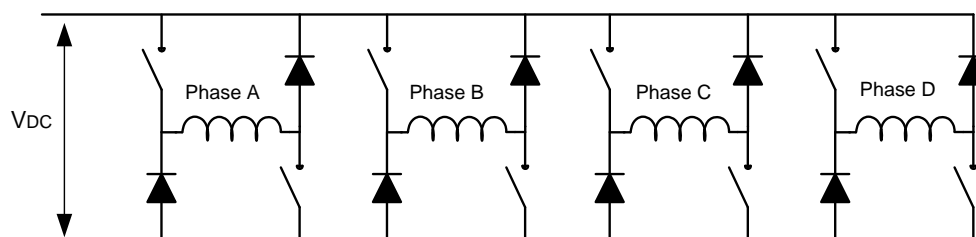
The asymmetric bridge converter is adopted in this research as the driven circuit, therefore, further details on its operation are provided below. There are three modes of operation in each phase: magnetization, freewheeling and demagnetization [12].

a) For motoring operation, magnetization period is when both the switches are turned ON and the energy is transferred from the source to the motor phase winding as shown in Figure 2.8 (a).

b) Freewheeling stage in motoring operation at low speeds is accomplished by keeping one of the switches ON and switching the other switch as shown in Figure 2.8 (b). With only one semiconductor ON, the motor phase gets slowly demagnetized through the respective freewheeling diode.

c) Demagnetization is achieved by applying negative DC-link voltage to the phase winding when the two switches are turned OFF as shown in Figure 2.8 (c). This helps in fast decay of current flowing through both the diodes.

Figure 2.8. Operation modes in one phase. (a) Magnetization. (b) Freewheeling. (c) Demagnetization.

(a)

(b)

(c)
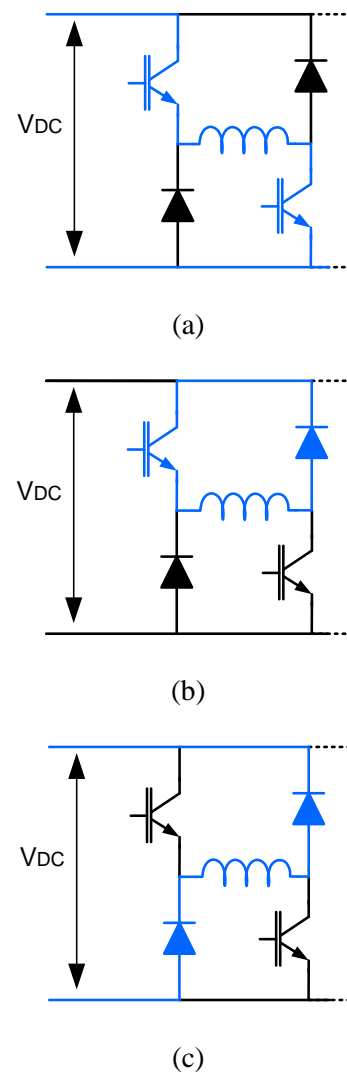
2.6 Control strategies

The purpose of the power converter circuit is, to provide some means to supply the current to the phase winding. The control circuit monitors the current and rotor position information to produce the correct switching signals for the power converter to match the desired requirements placed on the drive by the user. Appropriate positioning of the phase excitation pulses relative to the rotor position is the key to obtaining effective performance from a SRM drive system

[13]. The timing, conduction period and the magnitude of the phase current determine torque and efficiency. The type of control to be employed depends on the operating speed of the SRM.

The control parameters for an SRM drive are: the fire angle (θ_{on}), turn-off angle (θ_{off}), and the phase current. The definition of these variables will affect the drive performance and the complexity of its determination depends on the chosen control method for a particular application. For wide speed range operation, the important concepts that must be considered are discussed as follow.

At low speeds, the rate of increase of the current after turn-on is high because of the negligible back-emf, and the peak current must be limited by either controlling the average voltage (voltage PWM) or regulating the current level (chopping control) [7]. Hysteresis current control is commonly adopted in SRM drives due to its simplicity and fast response. It is also used to force maximum current into the motor to maintain the desired torque level. As the speed increases, the back-emf increases and opposes the applied bus voltage. Thus, phase advancing is necessary in order to have a certain current amplitude already established at the onset of rotor and stator pole overlap region. Due to the high back-emf the current is not allowed to reach high values and control is achieved only defining the advancing turn-on angle and adjusting the dwell angle. In this case, the switches are continuously ON during the conduction period of a particular phase and for this reason, it is known as single-pulse mode of operation.

In both conditions, low and higher speeds, the phase excitation is turned off early enough so that the phase current decays completely to zero before the negative inductance slope region is reached. Figure 2.9 shows the inductance profile along with the current waveform representing each mode of operation: low and high speeds.

In the current control mode (low speeds), there are two possibilities to regulate the current: soft-chopping and hard-chopping. In soft chopping control one of the switches in the phase leg always remain ON while a PWM signal is applied to the other switching changing its state to ON and OFF. Only after the turn-off angle both switches are commanded to OFF. In hard chopping controller the switches of the leg are turned ON and OFF simultaneously. This method is preferred for low speed operation and the controller operates at magnetization and demagnetization modes [1].

Figure 2.9. Inductance profile and current waveforms at low and high speeds.
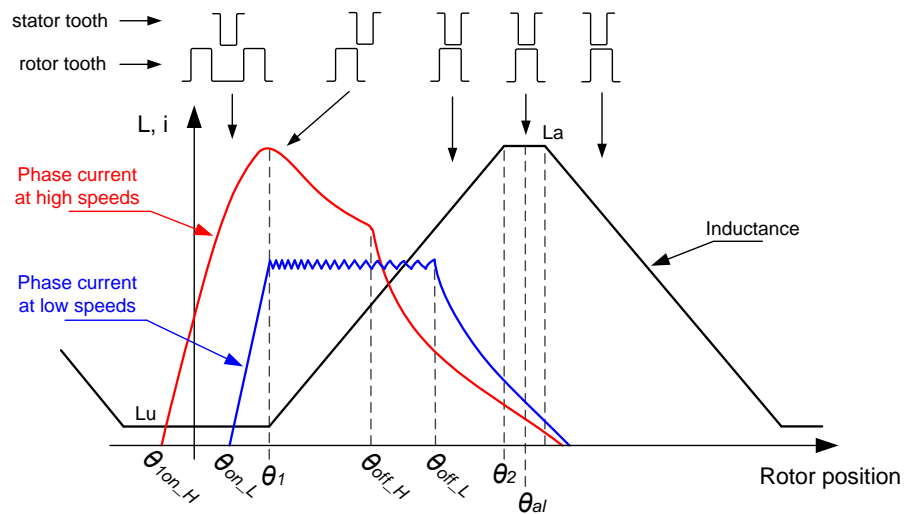
Adapted from [12].

2.7 SRM demerits

Despite to the attractive advantages, SRM also suffers from some demerits. The primarily drawbacks of this motor relies on the torque ripple and vibration/acoustic noise levels. These features are inherent characteristic due to the principle of operation.

The double saliency construction and the discrete nature of torque production by the independent phases lead to higher torque ripple compared with other machines [14]. The torque dip occurs in the vicinity of the alignment due to the non-linear relationship with rotor position and the sequential stator phases excitation yields a pulsated torque profile. This can create problems with increased audible noise, shaft degradation and possibly speed oscillation. The higher torque oscillation also causes the ripple current in the DC supply to be quite large, demanding a large filter capacitor.

Although torque ripple can contribute to acoustic noise, the majority of vibration, and consequently audible noise in SRM is a byproduct of the electromagnetic force. The surface forces can be decomposed into components in tangential and radial directions. It is clear that only the tangential forces acting on the rotor contribute to the motion and the remaining forces tend to originate vibration in the stator and rotor. The doubly salient structure is especially favorable to a strong radial force arising from the attraction between the rotor and stator poles. Therefore, radial forces will cause stator deformations due to the induced resonant vibration with the circumferential mode shapes and hence, acoustic noise is emitted from the frame.

The torque ripple and vibration phenomena will be covered in detail in the following chapters.

Requirements for motors are getting stricter. Vibration and noise become important metrics for many applications, specially home/office appliances. Also, in order to improve the performance of SRM and extend its applications in industry, it is essential to reduce the torque ripple. So far, many mitigation methods on these issues have been proposed. The next section presents the state-of-the-art regarding these achievements.

2.8   State of the art

Over the past decade, efforts have been dedicated to minimizing the SRM issues. In general, the SRM drive operation can be optimized by means of two approaches: structure design or control strategies. Good insights have been provided by the structural design to improve both, torque ripple and vibration issues. However, some of the proposed methods has physical limits, can increase the manufacturing costs or are not practical for machines already in the market, i.e. they are more suitable for motors in the design stage. On the other hand, control approach is based on current/voltage profiling which, in general, consists in adapt the control algorithm. Thus, it is more effective in attending conventional/commercial machines.

To reach this goal, computational resources have been largely employed in analysis of finite element models and run artificial intelligence algorithms. Table 2.1 summarizes some of the proposed methods found in the literature in attempt to mitigate the SRM primary disadvantages.

A review of the literature indicates that radial vibration of the stator frame in SRM drives has been the focus of many researchers. Cameron and Lang [15], through a series of carefully designed experiments, demonstrated the significance of the radial attraction and the consequent radial vibration of the stator frame as the main origin of vibration and acoustic noise in SRM drives. Many researchers have since provided insight on the impact of current profile and natural frequencies/normal modes on radial vibration and acoustic response of the SRM drives. Among the methods of analysis and control, the work of Pollock and Wu [16], stands out. While most of the analysis aim at comprehensive FEA analysis to enhance the geometry or control, the method proposed in [16] uses a two-step switching during the turn-off process to mitigate the radial acceleration of the stator frame. The method is based on active vibration cancellation which is very sensitive to the timing yet shows promise in enhancing the acoustic response without adverse impact on productivity and efficiency of the SRM drive.

Table 2.1. Classification of Related Researches

Approach	Goal	Proposed Method	Reference
Structural design	Vibration reduction	Addition of notches and holes in the magnetic circuit of stator and rotor to reduce the magnitude of the radial force	[17]
		skew the rotor and stator laminations to reduce the maximum value of radial electromagnetic forces	[18]
		Improvement in the stator pole shape to increase the mechanical strength of the stator; and change the shape of the rotor poles to reduce the radial force	[19], [20]
	Torque ripple reduction	modified rotor pole geometry	[21], [22]
		non-uniform air gap (asymmetry of poles) with asymmetric inductance profile	[23]
		new SRM configuration for stator and rotor through a new saliency	[24]
Control strategy	Vibration reduction	active vibration cancellation (AVC) by introducing a zero-voltage stage (voltage shaping)	[16]
		current profiling based on artificial neural network	[25]
		avoid abrupt changes in the excitation level applying a hybrid excitation: two-phase excitation with long dwell angle and conventional one-phase excitation.	[26]
		eliminate the third harmonic component in the sum of the radial electromagnetic forces by current shaping	[27]
		Semi-active control base on piezoelectric (PZT)	[28]
	Torque ripple reduction	Optimization of the turn-on and turn-off angles	[29], [30]
		PWM control technique to improve the current in which the current traces a contour to develop a constant torque	[31], [32]
		artificial intelligence algorithms to find out the optimal excitation profile	[33], [34], [35]

In general, vibration optimization has been faced controlling the radial forces and torque improvement is observed by current shaping methods. However, despite to a broad literature solution, still there is room for technical advances. For instance, some methods might have limitations or compromise other performances such as torque per ampere, efficiency, maximum torque output, etc., hence more considerations need to be included if these methods need to be adopted. Very few proposed solutions handle with multi-objective optimization. It is known that a radial force is the main source of vibration and this point inspired the development of control methods aiming to obtain an overall smooth radial force. However, the tangential force component might be affected by the proposed solution and some penalty in torque generation should be considered. In other words, depending on the method, some improvement in vibration signature is achieved meanwhile a worse torque profile is observed, and vice versa.

Moreover, the active cancellation proposed by [16], [36], is more suitable at single pulse mode, i.e. high speeds, and has some limitations such as requirement of power converters to

offer a zero-voltage freewheeling path and accommodating the delay corresponding to half resonant cycle.

In this dissertation, a new vibration cancelation method is proposed by designing the switching instants for the operation under current control (low speeds).

Chapter 3

Characteristics and modeling of the studied SRM

Switched reluctance machine has a highly non-linear magnetization characteristic due to the doubly salient structure. This chapter aims to determine the static characteristics of the SRM used in this research. Experimental flux linkage curves, incremental inductance and static torque profile have been obtained.

Moreover, the target machine is modeled in ANSYS package for 2D and 3D finite element analysis. The 2D model is used to perform magneto-static solutions required to develop the field reconstruction model of this machine, which is also covered in this chapter. The 3D model will be later used in the study of vibration modes, which will be described in the next chapter. An overview of converter board used to drive the SRM in the experimental tests is also presented.

3.1   Characteristics of the studied SRM

The results presented in this dissertation are based on a rotary radial flux 8/6 SRM, however, the proposed strategies can be extended to other SRMs with some adjustments. The main specifications of the target machine are shown in Figure 3.1 and Table 3.1. Figure 3.2 shows a picture of the real machine.

3.2   Static profiles

An important characteristic of the SRM is its inherent nonlinearity, hence accurate calculation of the static characteristics of the torque, flux linkage, inductances and back-emf is not straightforward.

Flux linkage and static torque data can be measured experimentally or can be numerically calculated using finite element (FE) analysis. However, the accuracy of FE analysis is variable

Figure 3.1. Main dimensions.
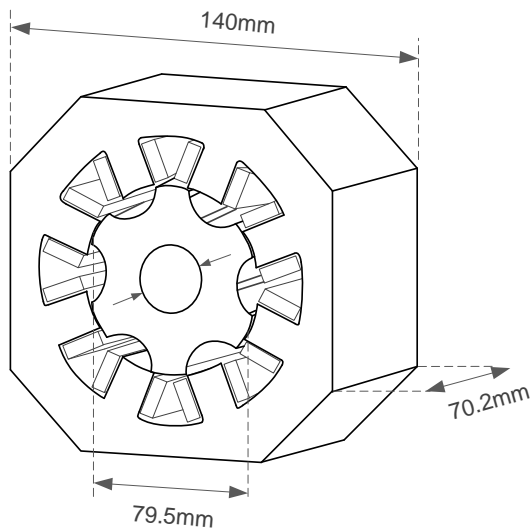
Table 3.1. SRM Parameters

Phases	4
Pole Configuration	8/6
Rated Voltage	48V
Power	2 kW
Rated speed	6000 rpm
Stator OD	140 mm
Rotor OD	79.5 mm
Stack length	70.2 mm
Shaft Diameter	24 mm
Phase resistance	11 mΩ
Number of turns	8
Airgap	0.3 mm
Magnetic material	M-19

Figure 3.2. Switched reluctance machine under study.
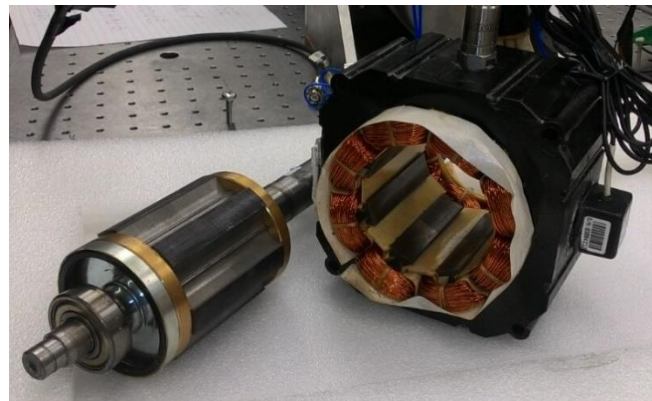
due to some complex second order effects, such as iron hysteresis [37]. Therefore, in this dissertation, the flux linkage curves are measured experimentally and compared with the finite element model output to validate the model accuracy. An accurate FE model guarantees a qualifies post-processing.

3.2.1 Flux linkage

The flux linkage characteristics of SRM depends on the rotor position and the stator phase current excitation. The measurement of flux linkage curves may be carried out through different methods [38]. A practical method of obtaining the SRM flux-linkage characteristic is indirect

measurement based on the voltage equation (2.2). Assuming the SRM phases are decoupled from each other, the flux linkage can be indirectly measured by equation (3.1):

$$\lambda(t) = \int_0^t \left(v(t) - R.i(t)\right)dt + \lambda(0) \tag{3.1}$$

where: $\lambda(t)$ is the phase flux linkage, Wb
$v(t)$ is the applied phase voltage, V
$i(t)$ is the phase current, A
R is the phase winding resistance, Ω
$\lambda(0)$ stands for the flux linkage at time $t = 0s$
t is time, s

Since there are no magnets on the rotor or stator, the initial flux linkage $\lambda(0)$ is negligible and in this research, it will be treated as zero when there is no phase current.

Figure 3.3 (a) shows the experimental setup for flux linkage measurements. It consists of the SRM with a rotor locking device. First, the rotor is mechanically fixed at any desired position and the stator winding is energized by DC a pulse of voltage [38]. The instantaneous winding voltage and current signals are recorded simultaneously as shown in Figure 3.3(b). Figure 3.3(b) depicts the oscilloscope screenshot for the aligned position and also shows the mathematical numerical integration result of equation (3.1).

Figure 3.3. Experimental flux linkage measurement. (a) Setup. (b) Measured waveforms.

(a)   (b)
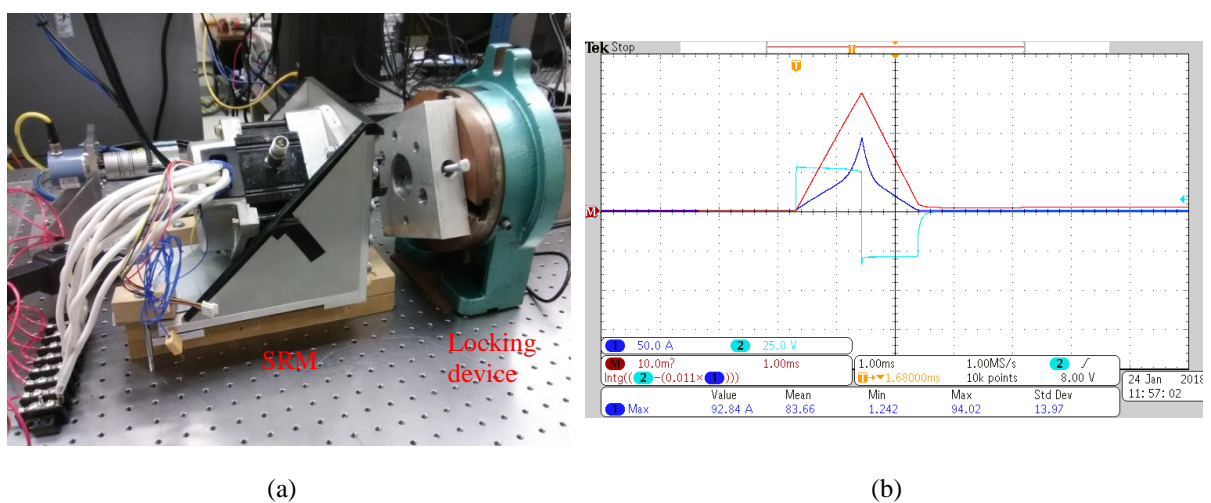
The aforementioned procedure is repeated spanning from aligned to unaligned position. A resolution of 1 mechanical degree has been adopted, resulting in 30 curves (8/6 SRM). For

visualization purpose, Figure 3.4 illustrates the curves for every 3 mechanical degrees rotor position. It is important to highlight that in the flux linkage measurements using this method the effects of magnetic hysteresis of the silicon iron laminations will result in not a single valued function of rotor position and phase current. Thus, the curves in Figure 3.4 are the average value, as proposed in [39].

Using the MATLAB spline interpolation function, the phase flux linkage can be evaluated at any rotor position and current. Figure 3.5 depicts the interpolated 3D profile from which is possible to note the non-linear relationship between flux linkage, excitation current and the rotor position.

Figure 3.4. Experimental flux linkage curves.
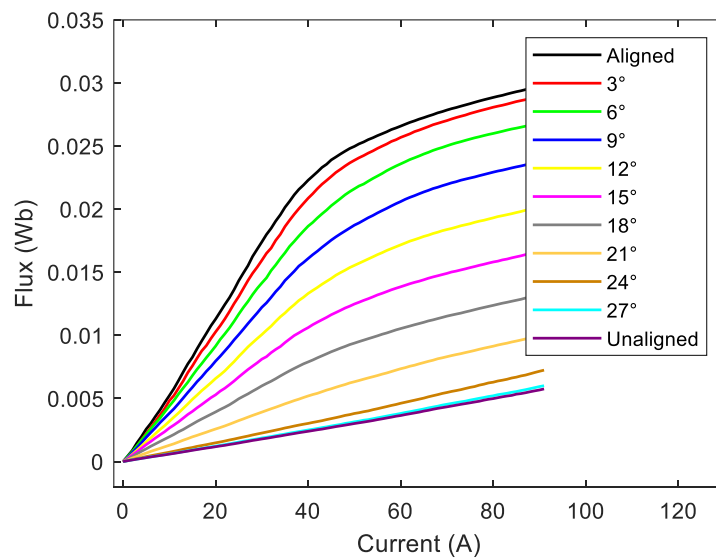
Figure 3.5. Experimentally measured and interpolated 3D flux linkage profile.
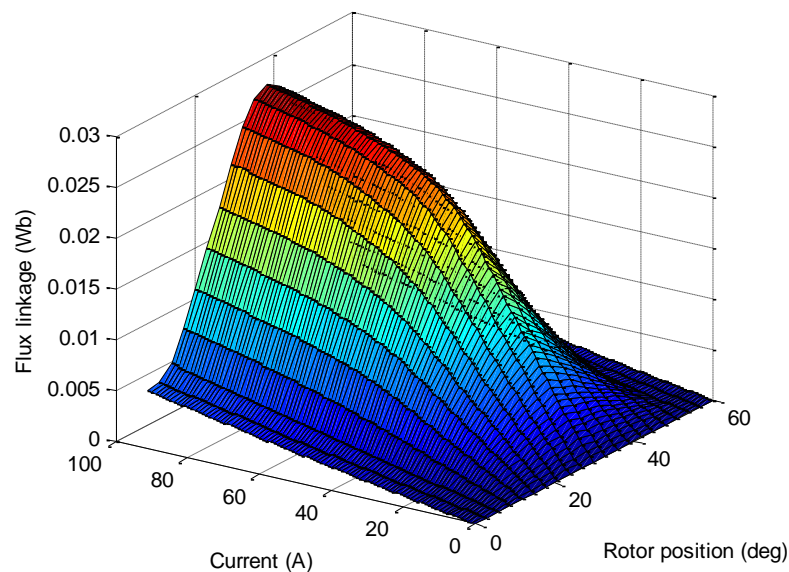
From the knowledge of the phase flux linkage data, other quantities, including the incremental inductance, back emf, and electromagnetic torque can be determined indirectly from it.

3.2.2 Inductance profile

The inductance of the magnetic circuit is a non-linear function of both phase current and rotor position. According to [38], the incremental inductance can be obtained as follow:

$$L_{ph} = \frac{\partial \lambda_{ph}}{\partial i_{ph}}$$
(3.2)

Using the expression (3.2) the phase inductance was computed for different current values and rotor position as shown in Figure 3.6. In this case, 30° represents the aligned position.

Figure 3.6. Experimental inductance profile.
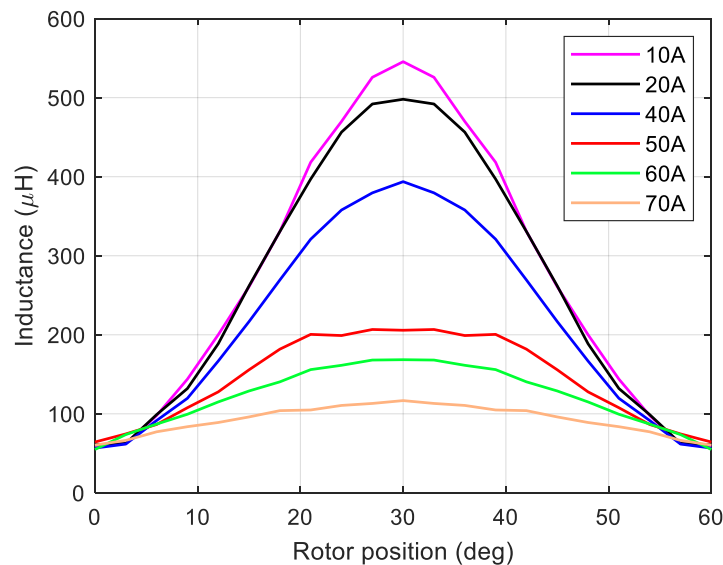
3.2.3 Static torque profile

The torque profile can also be obtained from flux linkage data if there is no torquemeter at hand. However, in this work an experimental verification was conducted in order to outcome with direct and accurate curves. To measure the static torque, a shaft-to-shaft torquemeter shown in Figure 3.7 (a) was installed between the SRM and the locking device. With the rotor mechanically fixed at a desired position a constant DC current is applied in phase winding. The torque developed was measured for various stator currents values. Figure 3.7 (b) illustrates the

measured torque values as a function of current and mechanical position. Analyzing the torque profile one can note that as the rotor approaches the aligned position, the generated torque reduces.

Figure 3.7. Experimental static torque measurement. (a) Torquemeter. (b) Measured torque profiles.

(a)   (b)
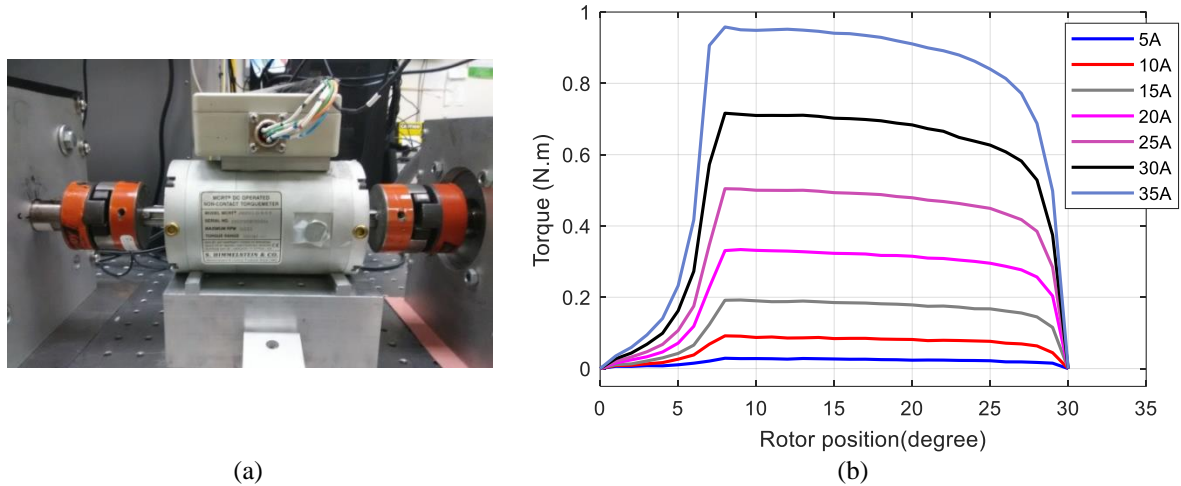
3.3   Machine model

Because of the doubly salient structure of the SRM, and local saturated magnetic field the determination of the electromagnetic characteristics is not straightforward. The SRM characteristics is very known to present a strong nonlinear function of phase current and rotor position, which virtually eliminates the possibility of representing it in a simple analytical expression. Therefore, numerical methods such as the well-known Finite Element (FE), has been widely applied to deal with the non-linear characteristics of the SRM.

First, the magnetic characteristics of the SRM were presented to gain insight into the non-linear relationship between the machine parameters and to map the characteristics of the particular machine under study. Specifically, the static torque profile is important to have a good grasp of the relationships between excitation current, rotor position and the individual phase torque generated, once one of the objectives of this research is to improve its profile based on current shaping.

However, to analyze the torque behavior during motion, a two-dimensional finite element model has been developed. Figure 3.8 shows the 2D section of the SRM modeled in software Maxwell/Ansys using the geometric parameters. Specifically, this model is used in a co-simulation in Simplorer, as detailed in Chapter 5. Moreover, the SRM model was also extended

to its 3D version (please see Figure 3.9) as a tool for investigation of the structural behavior. The SRM vibration response is covered in Chapter 4.

Although the finite element model has been built, such technique involves steps such as geometry domain discretization, calculations on each node and interpolation of these values to the regions between the nodes. This process demands high computational cost, even for the modern processing platforms. Therefore, in the optimization routine the Field Reconstruction Method (FRM) has been used to compute the electromagnetic forces and torque due to its fast modeling process for electric machines.

Figure 3.8. 2D section of the 8/6 SRM in Maxwell/ANSYS.
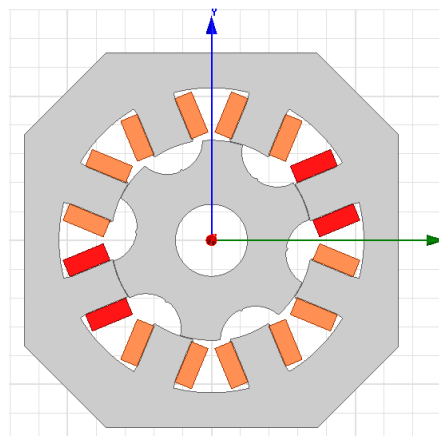
Figure 3.9. Exploded view of the SR machine.
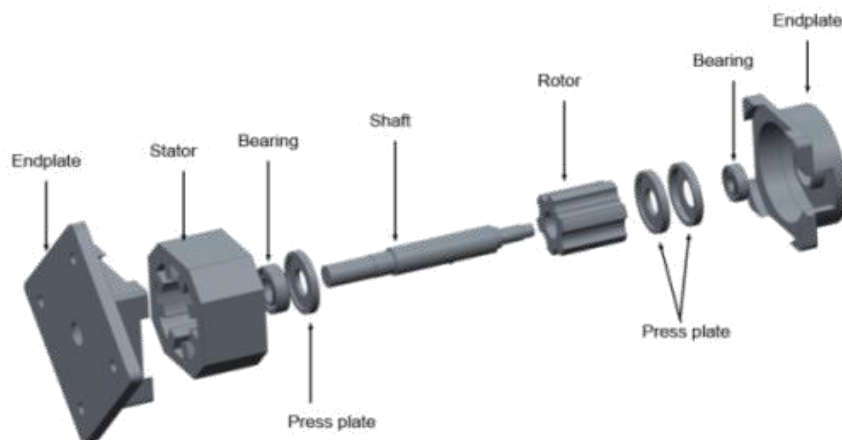
Adapted from [49].

3.4 Field Reconstruction Method (FRM) for SRM

An accurate model is crucial to perform a confident analysis of the electric machine. Moreover, an efficient model will be beneficial, manly if the model will be use in optimization routines. Torque optimization through FE model is possible, however, an iterative optimization algorithm can cause unreasonably long computational time and requires sophisticated computational facilities. Alternatively, FRM is a faster modeling process in which a minimal set of magneto-static field solutions are used as basis functions to determine the electromagnetic flux densities distribution.

The basis functions are FE solutions under a specific condition (base condition) and once these functions are established, the performance of the machine can be predicted for another arbitrary condition with minimal computation effort. FRM presents an accuracy similar to the FE however with a computation time much lower.

Indeed, the FRM advantages have been explored for modeling different types of electric machines. The work presented in [40] for permanent magnet synchronous machine, in [41] for induction machine and [42], [43] for wound-rotor synchronous machine, are some examples.

The FRM applied for SRM was first addressed in [44]. The first step to represent the SRM using the FRM is to use the finite element model of the target machine to compute magneto-static solution for $\overrightarrow{B_n}$ (normal flux density) and $\overrightarrow{B_t}$ (tangential flux density). These flux density components are sampled in a contour in the middle of air gap and stored in a look-up table as basis functions, please see Figure 3.10. The applied current during this process is chosen as a base value (i_b) and the magneto-static simulation is performed at the same current amplitude for different rotor positions, spanning from unaligned to aligned. Using the basis functions the flux distribution can be "reconstructed" for other excitation conditions as described in the following formulation:

$$\overrightarrow{B_n}(i_a, \theta_d) = \frac{i_a}{i_b} . h_n(i_b, \theta_d) \tag{3.3}$$

$$\overrightarrow{B_t}(i_a, \theta_d) = \frac{i_a}{i_b} . h_t(i_b, \theta_d) \tag{3.4}$$

Where:

B_n, B_t - Normal and tangential components of flux density B

i_b - Base current (current value applied to generate the basis functions

θ_d - Desired rotor position

i_a - The new arbitrary current excitation

$h_n(i_b, \theta_r)$
$h_t(i_b, \theta_r)$ - Basis functions for each rotor position θ_r

Figure 3.10. Basis function at 14°. (a) Flux distribution. (b) Flux density components due to 5A excitation.

(a)   (b)
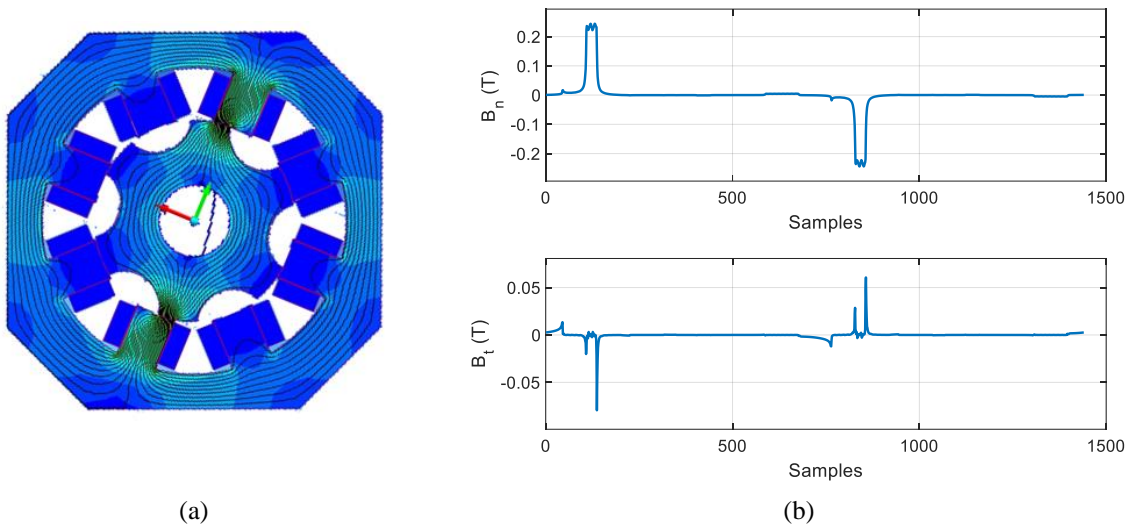
Due to the lack of permanent magnet or coil windings in the rotor of SRM, the FRM for this machine is only represented by these two equations. Basically, the basis functions provide the information on the flux distribution signature and the ratio between the currents adjusts the magnitude. To account for saturation, [44] presents a saturation multiplier using Fourier coefficients. Particularly, the machine under study presents a wide linear region in flux linkage curve, thus the saturation effects will not be considered in light loads. Moreover, herein it is assumed a perfectly symmetric machine and the same basis functions are applied to all 4-phases.

If the flux density $\vec{B}$ is known, further analysis, such as forces and torque, can be evaluated using Maxwell stress method [7]:

$$\vec{f_t} = \frac{(B_n . B_t)}{\mu_0} \tag{3.5}$$

$$\vec{f_n} = \frac{(B_n^2 - B_t^2)}{2\mu_0} \tag{3.6}$$

where, $\overrightarrow{B_n}$ and $\overrightarrow{B_t}$ are the normal and tangential flux density components, respectively, and μ_0 is the permeability of air. Integrating the tangential force density $\overrightarrow{f_t}$ along the contour in the air-gap, the torque is estimated by:

$$T = \int_\Gamma f_t . R . L_Z \qquad (3.7)$$

where R is the Γ contour radius and L_Z is the machine stack length.

In summary, the SR machine analysis using FRM concepts is represented in Figure 3.11. Figure 3.12 depicts the estimated flux density components in comparison with those given by the finite element software for arbitrary conditions. In this work the basis functions were obtained using $i_b = 5A$ and the results depicted in Figure 3.12 are for 23A excitation and rotor position equal to 10° (Unaligned = 0°), and the scenario with 31A excitation and rotor position at 22°. In both comparisons, a very good agreement has been observed.

Finally, to validate the model, the torque measured experimentally (continuous line) and the torque calculated using (3.7) (dashed line) are compared in Figure 3.13 for different current values. The discrepancy between the measured and estimated curves is due to the losses (not considered in the estimation).

Figure 3.11. Field reconstruction method concept.
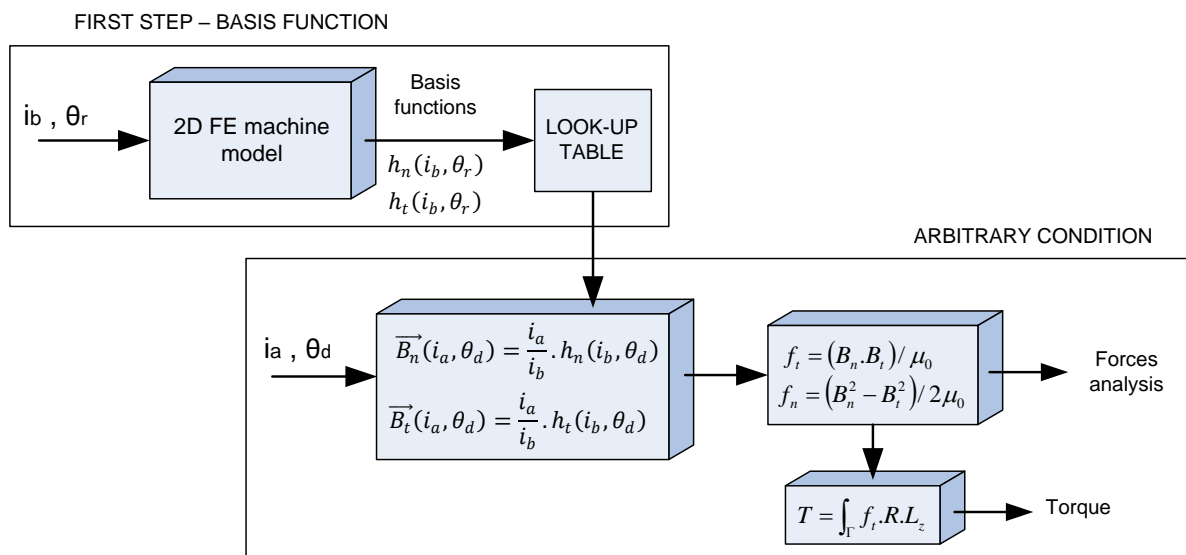
It is important to highlight that the advantage of the FRM is the simulation time. For instance, in the comparison showed for arbitrary condition in Figure 3.12, the finite element

software took approximately 2 minutes to calculate the flux components meanwhile the FRM took less than 1 second. Therefore, this model is suitable to be employed in an iterative routine and, moreover, it has proven to be accurate enough to guarantee a good post-processing output. The optimization routine using this model is detailed in chapter 5.

Figure 3.12. Comparison of the flux density components in the airgap obtained through FRM and FE for arbitrary conditions. (a) $\theta_r = 10°$ and 23A excitation. (b) $\theta_r = 22°$ and 31A excitation.

(a)   (b)
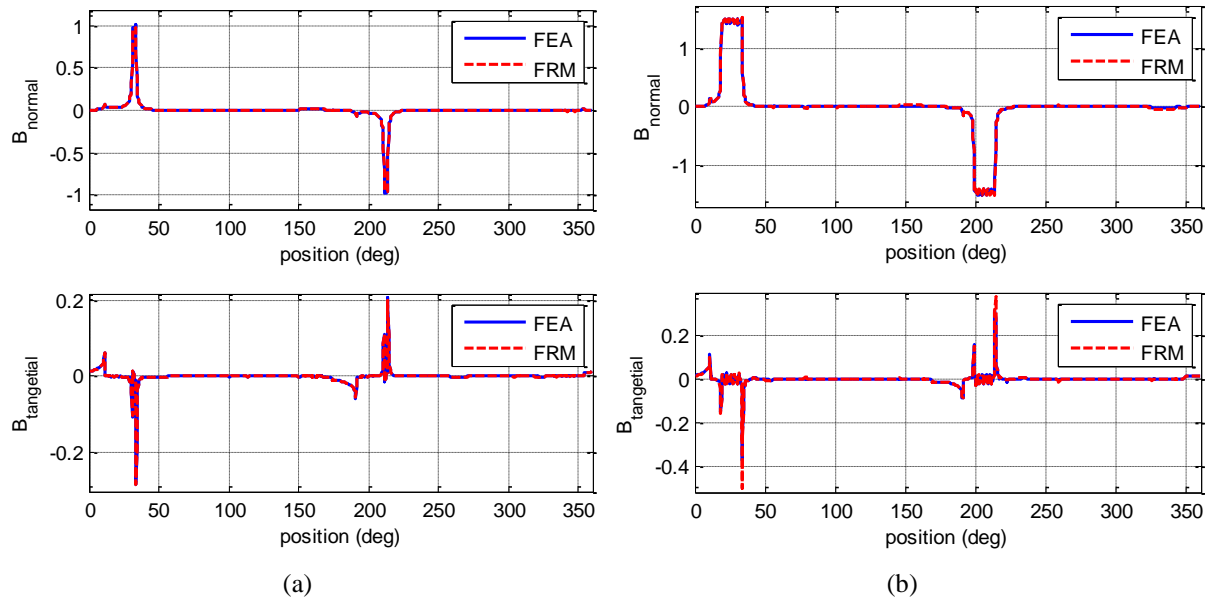
Figure 3.13. Comparison between the torque obtained experimentally (continuous line) and through the model (dashed line)
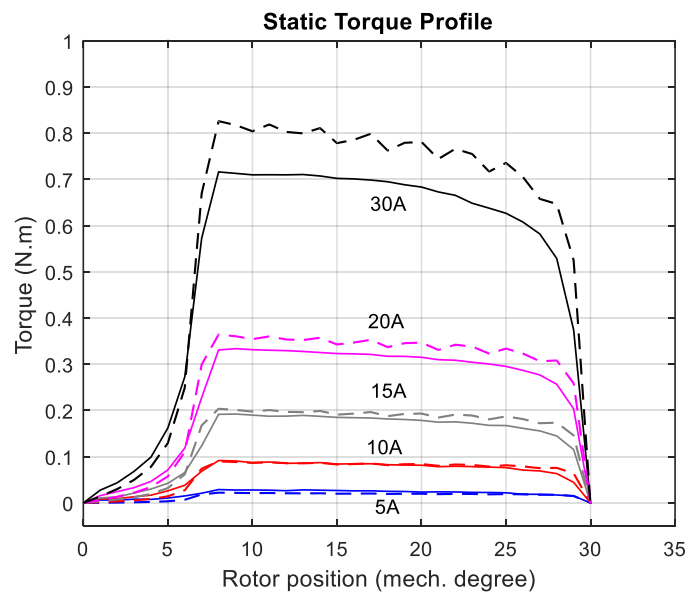
3.5 Motor drive

In the previous sections, the electric machine characteristics and model have been discussed. Herein, the converter board used to drive the SRM in the experimental tests is presented. The board consisting of the asymmetric bridge converter circuit, the DSP controller, signal conditioner and the gate drives for the power switches is shown in Figure 3.14.

A 4096-pulse incremental encoder (Celesco CH-25) is connected to QEP of DSP to read the rotor position and DC bus voltage is provided by a 2.5 kVA DC power supply. The main components used in the power circuit and the control circuit are listed in Table 3.2.

The DSP programming was developed in the Code Composer Studio (CCS) and part of the code is available in Appendix I.

Figure 3.14. Power and control board used to drive the SRM.

(1) Gate-drive board
(2) Encoder signal conditioner
(3) Phase leg – SiC components
(4) DSP board
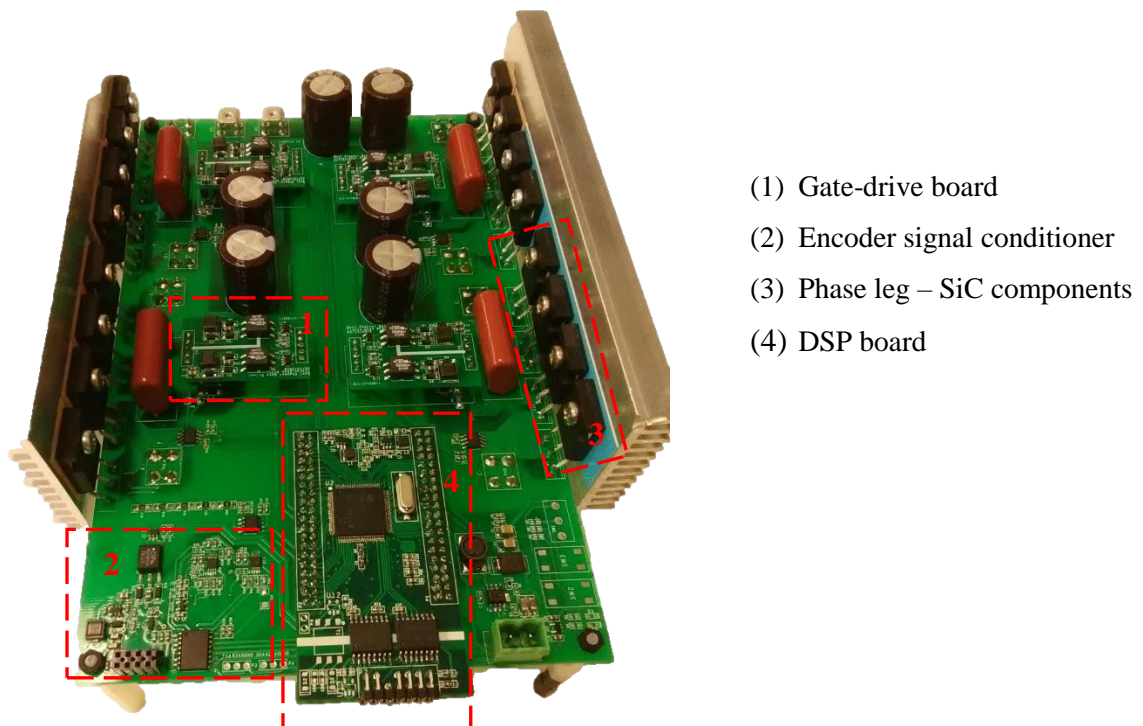
Table 3.2. Main Electronic Components

DSP	F28379s
Current sensors	ACS 712
Power MOSFET	IRFP4410z
Diode	STPS40H100CW

Chapter 4

Analysis, Prediction and Optimization in Vibration of Switched Reluctance Motor

The torque ripple, along with the vibration are considered crucial issues of switched reluctance motors in comparison with other traditional motors. Specifically, the high vibration level gives rise to acoustic noise, which, prohibit the use of SRM in sensitive applications. This chapter presents the vibratory study of the target SRM. First, a comprehensive analysis on the natural frequencies and vibration modes are conducted through the impact hammer test and modal finite element analysis. A prediction model of stator vibration based on the mechanical impulse response (MIR) is also described and, finally, an active vibration cancellation strategy is presented aiming to optimize the operation of SRM at low speeds. Experimental results confirmed the effectiveness of the proposed strategy.

4.1 Origins of vibration in SRM

Electromechanical energy conversion can be viewed as the interaction between electromagnetic forces and the mechanical systems. Although the motional forces are the desirable outcome in this process, byproducts produced by other undesirable force components are also present, i.e. vibration and acoustic noise.

Vibration and acoustic noise in electric machines have multiples sources. Vibrations may be caused from electrical, mechanical, aerodynamic or magnetic origins. Despite to that, it is widely accepted that the main source of vibration in SRM is due to the stator deformations caused by the radial electromagnetic forces [15], [45]. During the operation the stator pole is pulled inward due to the strong radial attraction between the stator and rotor poles, and as such, the stator assumes an oval shape during the rise of radial force. The deformation of the stator structure peaks at the turn off position. At this instant, a sudden change of radial force produces a large vibration, which in turn will produce acoustic noise emitting from the frame.

Figure 4.1 shows the principle of vibration and acoustic noise generation in SRM. Electromechanical energy conversion in SRM results in distribution of magnetic forces which act on the stator and rotor poles surface in radial and tangential directions. Although the primary goal of the energy conversion is to create forces acting on the rotor in tangential direction (hence contributing to the motion), significant non-contributing radial force components will act on the stator and rotor structures. These byproducts will initiate displacements in not intended directions. Due to the specific shape of the stator and the rotor in SRM, severity of the radial forces acting on the stator pole surfaces, and abrupt commutation in the vicinity of the aligned position where these radial forces exhibit their maximum, the radial vibration of the stator is known to be major contributor to the vibration and acoustic noise in this family of motor. Basically, the deformations in the diameter of the stator, displaces surrounding air creating differences of pressure. This pressure variation is perceptible to human ears as noise.

Figure 4.1. Vibration mechanism in SRM.
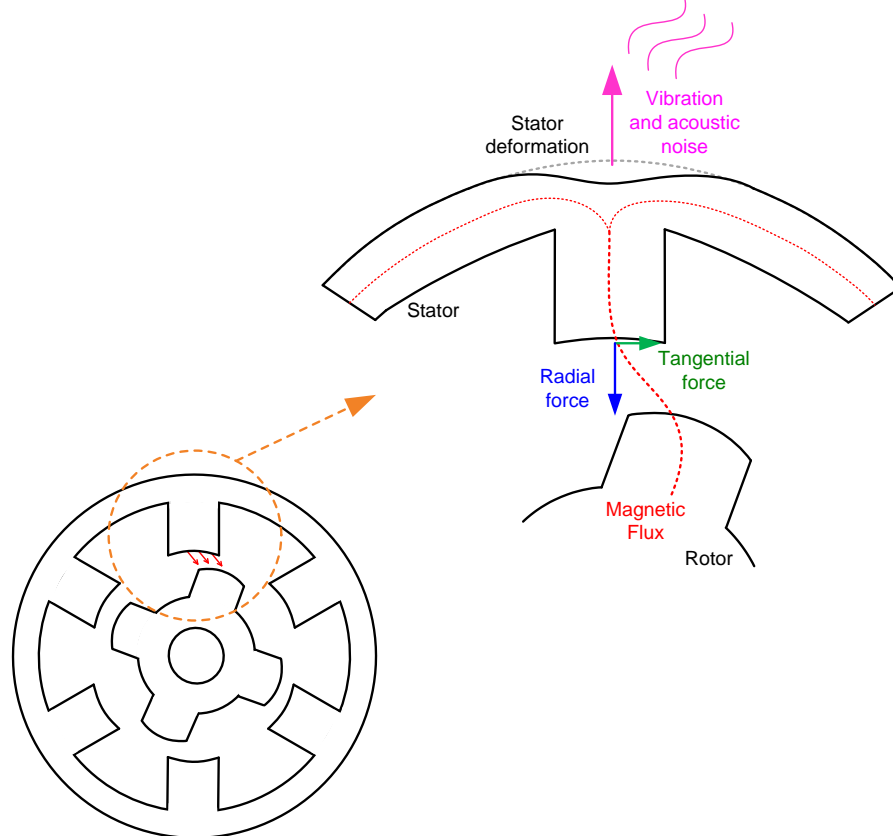
Stator deformation, i.e. the shape that the stator assumes is related to the natural frequencies of its structure. Moreover, the motor geometry is a multiple degree of freedom (MDOF) system and despite to some degree of nonlinearity, the resulting dynamic response

can generally be represented as a superposition of the contributions of each single degree of freedom (SDOF) [46].

4.2 Natural frequencies and vibration modes

The resulting vibration and acoustic noise from SRM can be particularly severe if mechanical resonances are triggered. Therefore, the natural frequencies and the respective mode shape of each one of these frequencies must be investigated. The dynamic behavior of any structure with multiple degrees of freedom can be characterized by three fundamental properties: natural frequencies, natural modes of vibration and damping factors. The natural frequencies indicate the rate at which the structure oscillates, after having ceased the excitation force that caused its movement, also said free movement. The modes of vibration are the way the structure vibrates and are related to each of its natural frequencies, i.e. for each natural frequency there is a specific mode of vibration. The damping factor in turn provides a measure of how much the body's oscillation (vibration) movement is extinguished when there are no external forces acting. The determination of these parameters can be obtained by the so-called modal analysis, which is the process consisting of theoretical and experimental techniques that enable the construction of a mathematical model representative of the dynamic behavior of the system being studied.

The natural frequencies of the motor depend on the geometry and the properties of the material. This concept can be easily understand analyzing a simple SDOF system consisting of a mass (m), spring (k), damper (c) and excitation (f). The energy enters the systems through excitation force, is stored in the in the mass and the spring in the form of kinetic and potential energy, respectively, meanwhile is gradually dissipated in the damper. Thus, with the force ceased, the mass displacement ($x(t)$) is described by a damped oscillating motion. Mathematically, the equation of motion in this case is [46]:

$$m\ddot{x}(t) + c\dot{x}(t) + kx(t) = f(t) \tag{4.1}$$

Using eq. (4.1) once can compute the natural frequency in rad/s as a direct function of the stiffness (k), and inverse of the structure mass (m):

$$\omega_n = \sqrt{\frac{k}{m}} \tag{4.2}$$

The extension of SDOF concepts to a more general MDOF system, with n degrees of freedom, leads to matrix representation of equations of motion:

$$[m]\{\ddot{x}(t)\} + [c]\{\dot{x}(t)\} + [k]\{x(t)\} = \{f(t)\} \qquad (4.3)$$

As for the SDOF system, the solution of the equation of motion with no excitation, gives the modal parameters (roots of the equation) of the system. For the MDOF case, however, a unique displacement vector called the mode shape exists for each distinct frequency and damping. In other words, the mode shape is an eigenvector of the systems and represents the displacement in each degree of freedom for a specific frequency and therefore defines the shape assumed by a structure.

As discussed, both, natural frequencies and modes of vibration can be obtained theoretically. Nevertheless, it is also possible and practical to obtain this information experimentally.

4.3   Experimental modal analysis

Modal analysis testing is widely used for investigation of dynamic properties of structures, such as natural frequency, damping factor, mode shape and modal mass [47]. It is commonly performed experimentally using impact testing or shaker testing. The impact test is conducted using an instrumented hammer that has a load cell to measure the magnitude of the applied force and it is typically operated manually (please, see Figure 4.2(a)). The shaker system is an electronic device used to excite the structure. In both tests accelerometers are placed on the body of the structure under test to capture the acceleration (vibration) response as illustrated in Figure 4.2(b).

In this research the experimental modal analysis carried out in the 8/6 SRM under study was performed by impact testing. The motor parts were excited using the impact hammer (086C03, PCB Piezotronics, USA) and 2 mini ICP uniaxial accelerometers (352A56, PCB Piezotronics, USA) showed in Figure 4.3(a) were placed on the stator and rotor to capture the vibration. Two signal conditioners (one for the hammer and the other for the accelerometers) were used before signals were recorded in a digital oscilloscope. Please, see Figure 4.3(b).

Figure 4.2. Modal analysis. (a) Instrumented hammer used for impact testing. (b) Electromagnetic shaker used to test a car's door with attached accelerometers.

(a)

(b)

Figure 4.3. Equipment used in the impact modal test. (a) Mini accelerometer (b) Signal conditioners.

(a)

(b)

[Courtesy of PCB Piezotronics]

According to the literature review, the procedure used to perform the experimental modal test is to suspend the object on analysis by elastic or elastic strings in order to create a condition similar to the so-called free-free body. Generally, structures have several natural frequencies because it can vibrate freely (after being excited by a force) in several directions. This condition refers to the possibility of free movement in all directions by the structure, after the external force is applied.

In theory, the structure under test should be excited with a perfect force impulse. This would have an infinitely short duration, which would result in a constant amplitude in the frequency domain. As in real applications, this impulse is impossible to produce, we must apply an impact using the instrumented hammer with a short contact time to generate the impulse. The duration of this time is directly linked to the frequency content of the applied force. Thus, in practical, it is not possible to excite all frequencies with the same magnitude. However, the most important natural frequency is the first, the lowest of all, called the fundamental frequency.

It is important to note that, in conventional structures, the first frequency is always the most preponderant to the oscillatory movement, and the other modes of vibration are insignificant compared to this one [47].

Additionally, an important consideration in this type of test is the selection of the appropriate tip type. This is because the commercial hammers have different tips that can be changed according to the type of material from which the object to be tested is made. Figure 4.4 shows the frequency range that each tip can excite.

Figure 4.4. Family of impulse hammer response curves.
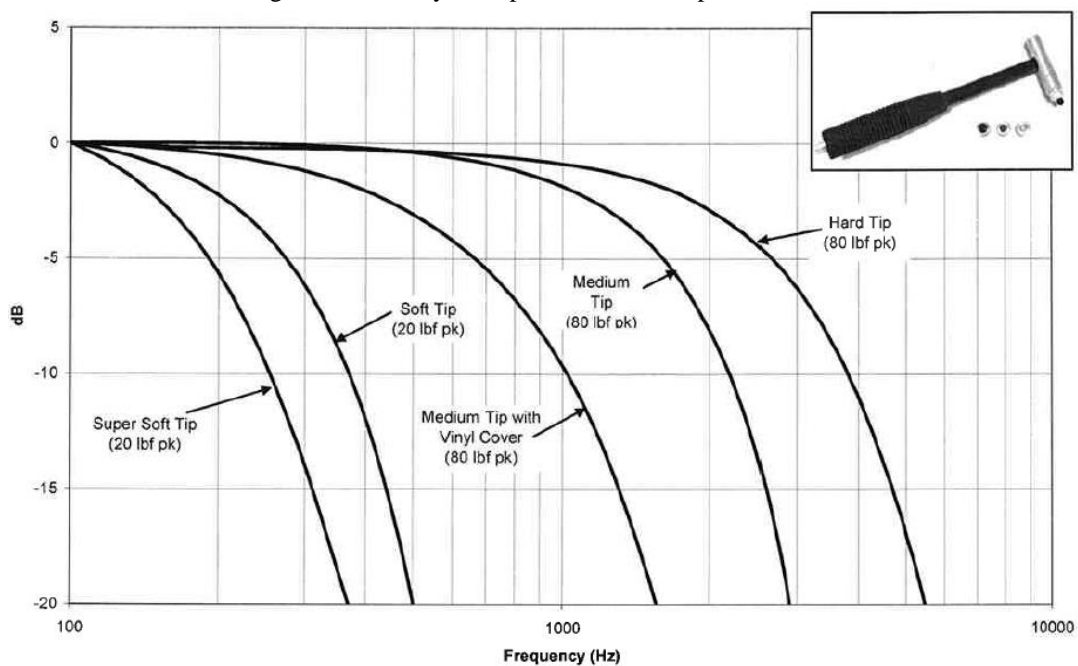
The test should be done at various points in the structure, and usually one of following methods is adopted [48]:

1) Several accelerometers are placed in different positions in the structure and an impact is produced. In this way, a single impact is required, and the data is all captured at the same time as a SIMO system. Although fast and efficient, this test requires a large number of transducers and an equally large investment in a measuring system with enough channels to simultaneously record all of our responses.

2) A single accelerometer is installed in one position and the structure is impacted in several places. This methodology is known as roving hammer test. This involves less resources but takes longer as several measurements are needed.

3) The third method is basically the inverse of the previous one. A single point of the structure is adopted to receive the impacts while a single accelerometer is relocated at each test, covering several measurements. This is known as roving accelerometer test. Although this method is still efficient in terms of transducers and measuring system, it is less time efficient, since moving an accelerometer requires greater care. Usually this method is used in situations where considerations of physical space make it possible to position accelerometers, but there is not enough room to use a hammer.

4.3.1   Results for the studied SRM

First, the stator and rotor were hung separately by straps to create a free-free condition as shown in Figure 4.5. The procedure adopted was roving the hammer while both accelerometers were kept fixed in the chosen pick up point. Figure 4.6 depicts one of the impact forces applied to the stator and the correspondent recorded acceleration.

Figure 4.5. Suspended parts for modal test. (a) Rotor. (b) Stator.
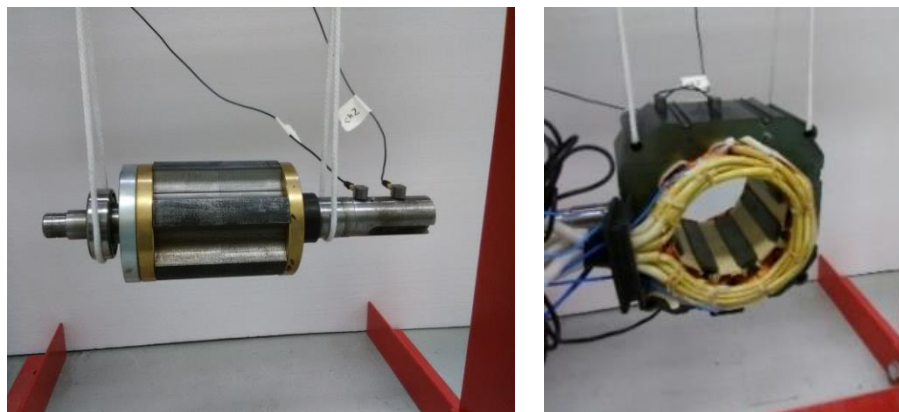
(a)   (b)

More than one impact has been applied on the stator body to validate the measurements and have a representative behavior. In addition, two accelerometers have been employed in these tests just to compare the responses and guarantee a confident acquisition.

The analysis of the acceleration signals typically relies on Fourier analysis. The fast Fourier transform (FFT) of 8 different tests were then performed using the MATLAB. Figure 4.7 illustrates the water fall plot of the acceleration in the frequency domain. As one can note, as the impact point around the stator surface changes, it might be favorable to excite some frequencies meanwhile not others. Moreover, once the test is performed manually the applied force is different for every impact. These factors contribute to have different magnitudes in the frequency components, however, it is possible to identify the dominant natural frequencies as 1875 Hz, 2400 Hz, 3750 Hz, 4400 Hz and 5100 Hz.

Figure 4.6. Stator hammer testing. (a) Impact force. (b) Acceleration measured on the stator housing.
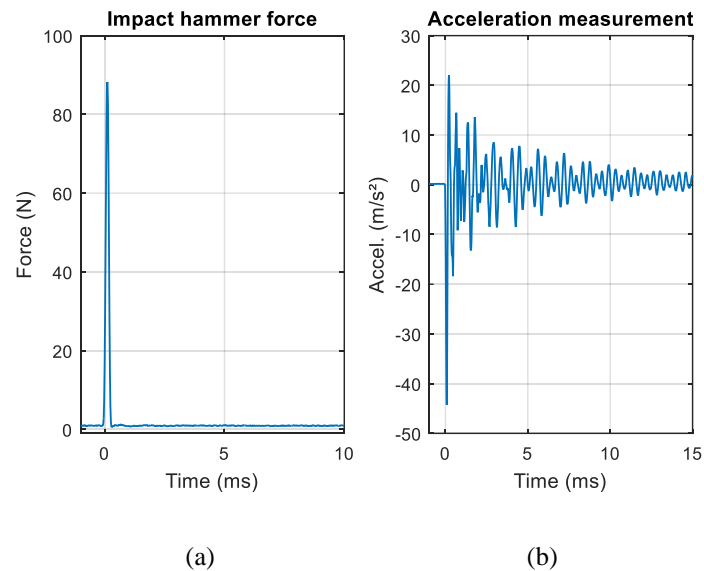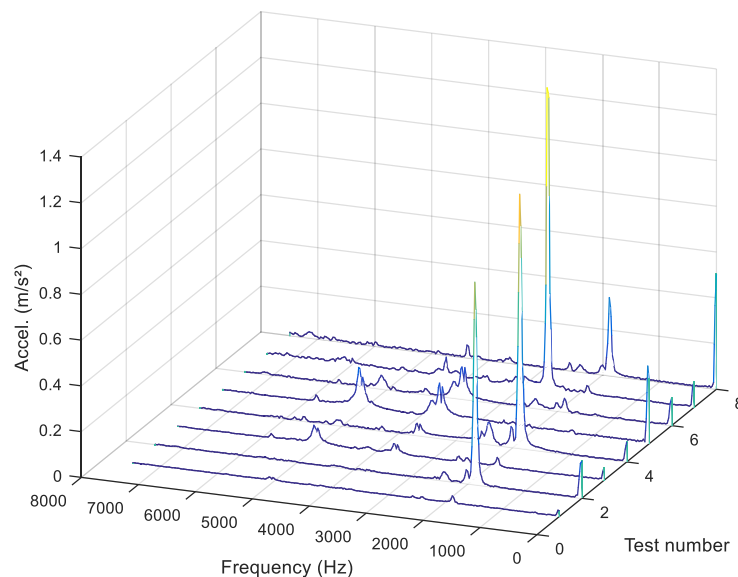

(a)   (b)

Figure 4.7. Frequency domain of the accelerations measured on the stator surface for 8 impact tests.

Although it is possible to notice the presence of a natural frequency around 6 kHz, in this work only frequencies below 5.5 kHz will be considered valid due to the hammer limitations (even with the hard metal tip – please see Figure 4.4). The coherence function plot for one of the measurements is depicted in Figure 4.8. This graph displays the portion of the output frequency range which is tightly correlated with the excitation. In this case a high coherence value indicates a reliable range of frequency for which the measurements are trustworthy. Therefore, the measurement presents good quality (coherence close to 1) only up to 5.5 kHz. The low frequency observed in the beginning of curves in Figure 4.7 is due the

Figure 4.8. Coherence function between output (accel.) and input (hammer) signals.
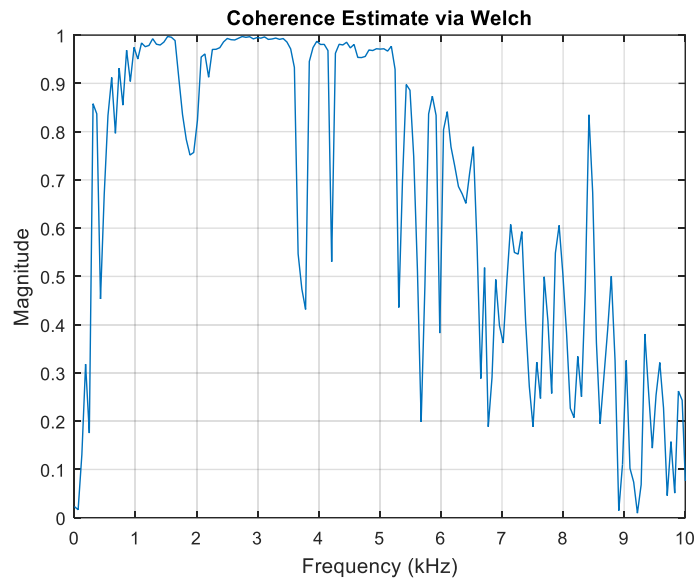
setup test (elastic supports) and might be neglected.

To better describe the motion-per-force input-output relationship between two points on the stator, the frequency response functions (FRF) can be computed. The FRF describes the ratio of one signal with respect to another signal over frequency range interested. In this case it is the acceleration over the force (A/f), also known as *inertance*. Others commonly forms of frequency response are the mobility (V/f) and compliance (X/f) [46]. It is also important to mention that a FRF is a complex signal which can be analyzed through different plot methods: magnitude/phase, real/imaginary (Nyquist plot) or using the Bode diagram. Figure 4.9 illustrates the FRF of stator tests.

A similar analysis has been conducted in rotor structure. Figure 4.10 shows the time domain acceleration measured on the shaft, while Figure 4.11 illustrates the corresponding

response in frequency domain along with other recorded accelerations due to different impact points.

Figure 4.11 reveals that the natural frequencies for rotor structure are 2150 Hz and 4750 Hz. It is important to notice that the rotor has less mass than the stator, therefore, according to eq. (4.2) it is expected to have natural oscillation in higher frequencies, however, as previously discussed, the setup is not suitable for frequencies above 5.5 kHz. Despite, the presence of a natural frequency around 7 kHz is notable. This frequency is later confirmed by the FE modal analysis.

Figure 4.9. Stator FRFs and natural frequencies.
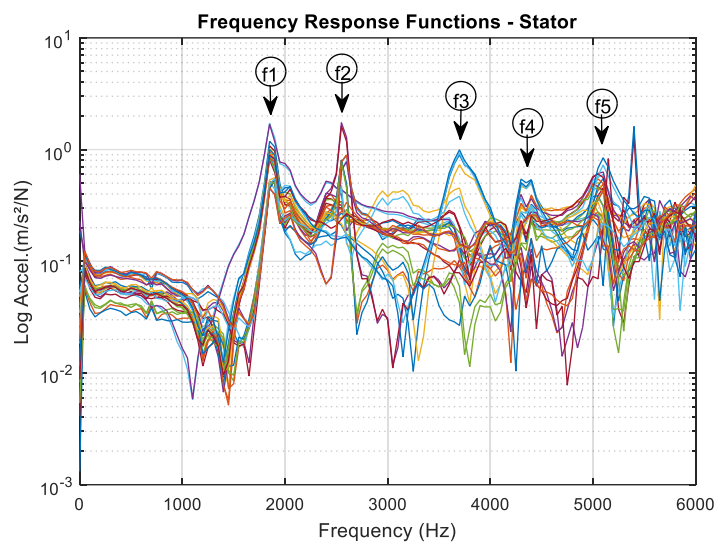
Figure 4.10. Rotor impact testing. (a) Excitation Force. (b) Measured acceleration in time domain.
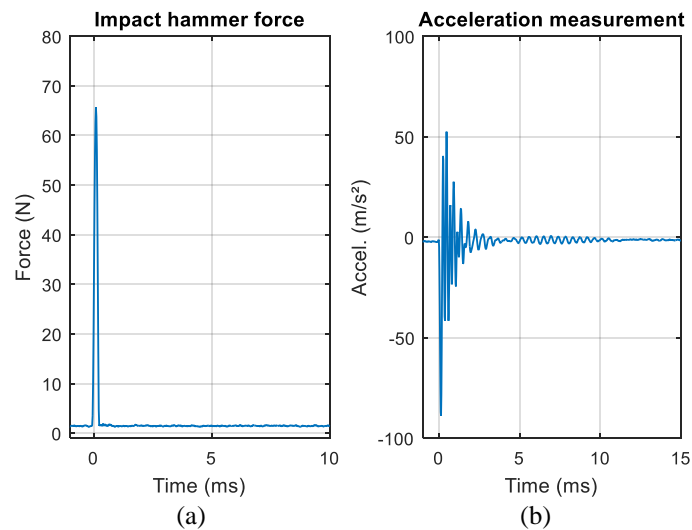
The amplitude of FRFs for the rotor tests expressed as inertance are shown in Figure 4.12. For demonstration purpose, rectangular coordinates plot (the real part and the imaginary part versus frequency) and the Nyquist plot of one rotor FRF are shown in Figure 4.13. Rectangular coordinates display that the imaginary part is maximum at resonance and the real part is zero [46]. Nyquist data representation emphasizes the area of frequency response at resonance and traces out a circle for each degree of freedom (DOF).

Figure 4.11. Rotor accelerations in frequency domain for each 25-impact test.
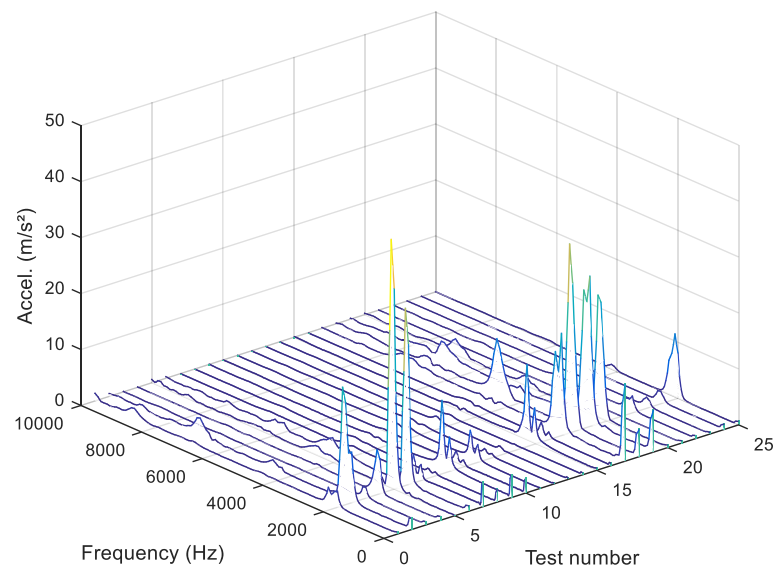
Figure 4.12. Rotor frequency response functions.
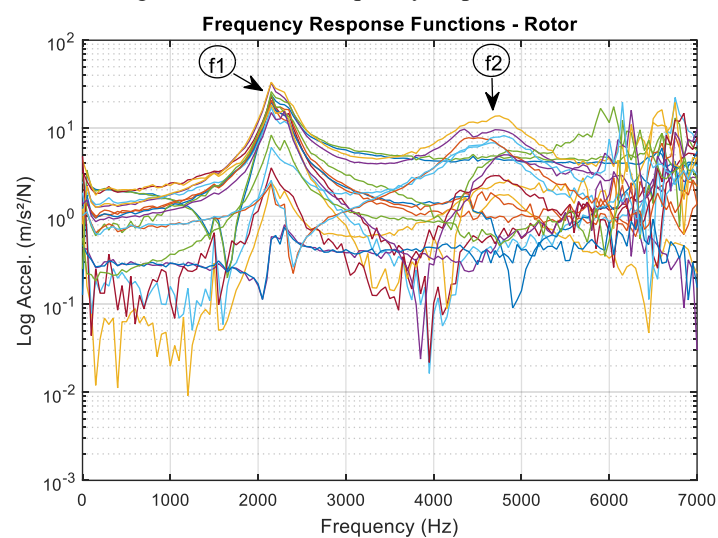
Moreover, using the imaginary part of the rotor FRFs obtained in a measurement mesh

along axial direction, it is possible to predict the mode shape of vibration by inserting a line that connects the peaks (for the same frequency) using the same point of measurement and relocating the hammer to impact the other points in the mesh. Figure 4.14 shows the estimated first and second mode shapes obtained through this method.

Figure 4.13. 3D plot of real and imaginary parts as a function of frequency and the Nyquist plot of a rotor FRF.
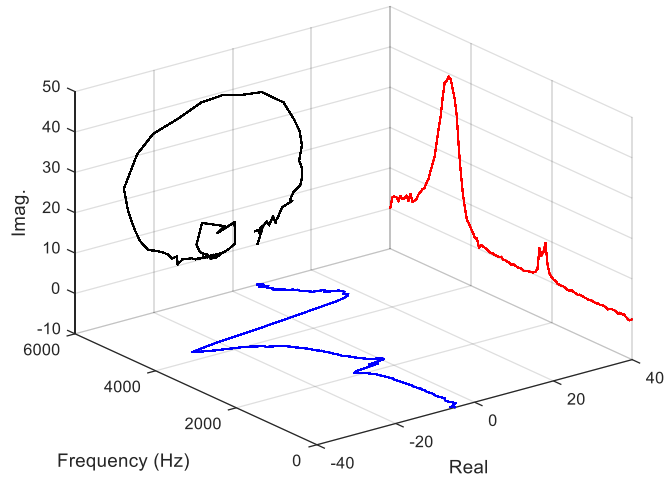
Figure 4.14. Rotor mode shape estimation. (a) Mode 1 at 2.1 kHz. (b) Mode 2 at 4.7 kHz.
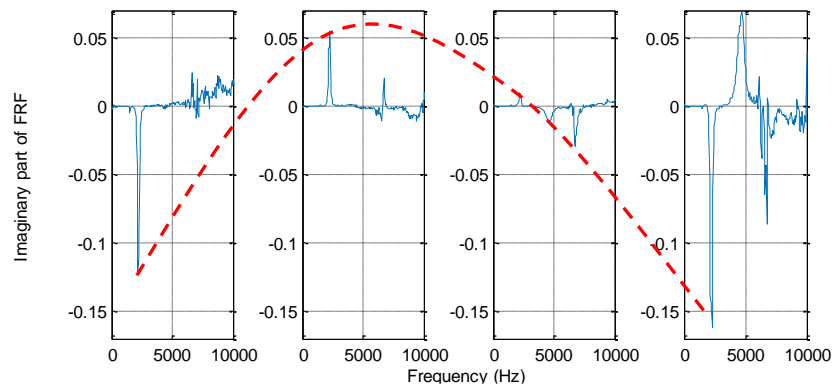
(a)
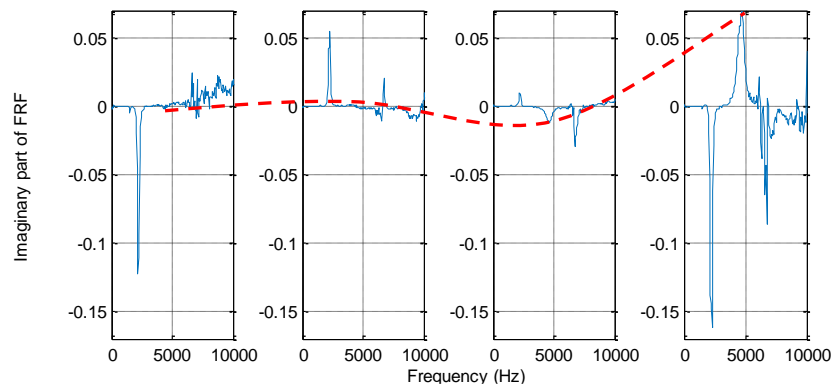
(b)

The experimental modal test presented helped to identify some of the natural frequencies of stator and rotor. However, natural frequencies beyond 5.5 kHz could not be confirmed using the hammer at hand. Furthermore, the mode shape analysis would require many data and would be an exhaustive process without the help of a software. Only two rotor mode shapes have been estimated due to the rotor structural format.

Therefore, others natural frequencies and the vibration modes will be find out using the finite element modal analysis. First, parameters such as damping are extracted from the experimental data and used to tune the finite element model.

The damping factor can be estimated by the half-power method based on the frequency response function, also known as vibration transfer function [46], [49]. In the half-power method, the damping is estimated by determining the sharpness of the resonant peak. It can be calculated as equation (4.4) using the transfer function plot. For structures with multiple peaks, the frequency response can be divided into frequency bands corresponding to each resonant peak as shown in Figure 4.15. Thus, every resonant peak can be treated as a single-degree-of-freedom system and the damping can be related to the width of the peak between the half-power points, i.e. points below and above the resonant peak at which the response magnitude is 0.7071 times the resonant magnitude.

$$\xi = \frac{\omega_2 - \omega_1}{2.\,\omega_n} \tag{4.4}$$

where ω_1 and ω_2 are frequency of half power points and ω_n is a natural frequency.

Therefore, using the half-power method in the average FRF [46] of Figure 4.9 the calculated damping ratios for each stator natural frequency are listed in Table 4.1. Similarly, the calculated damping for the rotor's frequencies are summarized in Table 4.2.

Table 4.1 - Damping ratios for stator obtained by Half-power method.

Frequency	f1 (1875Hz)	f2 (2400Hz)	f3 (3750Hz)	f4 (4400Hz)	f5 (5100Hz)
Damping ratio (ζ)	0.0098	0.0567	0.0605	0.0743	0.0321

Table 4.2 - Damping ratios for the rotor obtained by Half-power method.

Frequency	f1 (2150Hz)	f2 (4750Hz)
Damping ratio (ζ)	0.0345	0.0255

Figure 4.15. The half-power method for determining the damping.
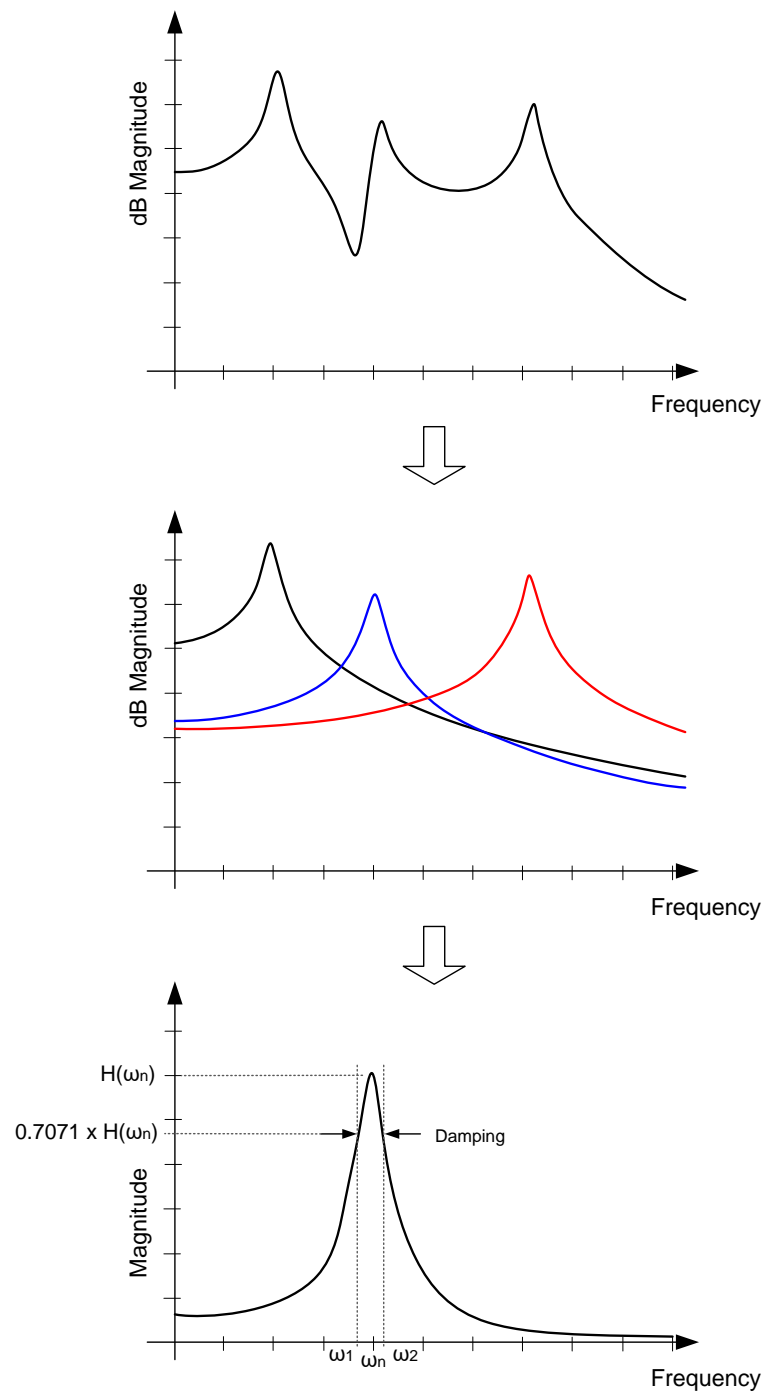
As mentioned before, although a finite element analysis is a useful tool for solving structural mechanics problems and specifically, it can be used for determining the modal properties of a structure, it is often necessary to validate the results from this theoretical prediction with measured data from a modal test [46], [48]. In general, this correlation method involves two major steps: i) the modal parameters, both frequencies and mode shapes, are compared and the differences quantified; ii) adjustments and modifications are made, usually to the finite element model, to achieve more comparable results. Figure 4.16 illustrates this iterative process.

Figure 4.16. Adjustments in the FE model through the modal parameters.
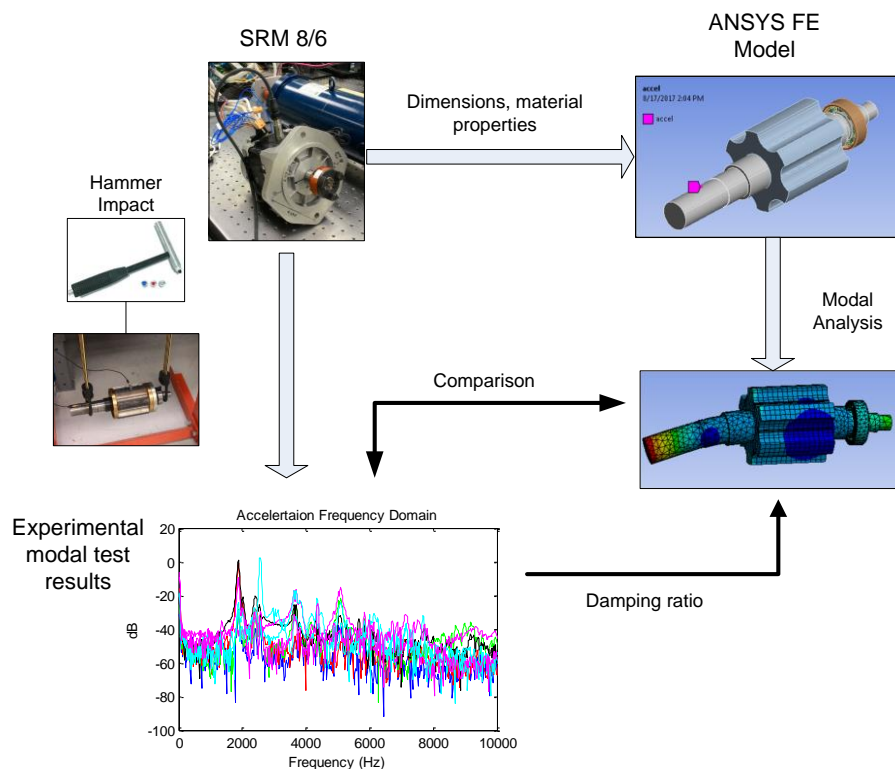
4.4 Finite element modal analysis

According to the literature review, modeling of the modal characteristics of electric machines is difficult because material properties and complexity of the boundary conditions for the machine components. With regards to the material properties, special attention has to be given to the laminated electrical steel sheets. The Young's modulus value of steel (normally 2×10^{11} Pa) has been widely used by researchers in electric machine field, however, experiments conducted in [50] showed a smaller value for the Young's *moduli* when laminated

material is used. Moreover, in [51], [52] it was found that lamination has an orthotropic characteristic, which will also be adopted in this dissertation. This seems to be more consistent with stator stacked structure.

Another concern in modeling of vibration in electric machines is the impact of the windings. In [50], to account for the winding properties, an equivalent mass for stator tooth and windings was calculated, so the poles were treated as a third material with a new density. However, the Young's modulus and Poisson's ratio were kept the same as a pure magnetic material. Although, it is an acceptable approximation, the authors in [53], [54] concluded that the stator windings have a significant effect on modal frequencies and cannot be simply treated as an additional mass, i.e. stiffness effects of the stator winding should be considered. Therefore, it was decided to keep the windings in the 3D structural model and the contact with the stator tooth was modeled as bonded (no penetration, separation or sliding between faces or edges).

The SRM prototype dimensions were used to construct the 3D model in ANSYS workbench as shown in Figure 4.17. The materials and their properties for the main components in the model are shown in Table 4.3. In addition, the contact between the machine parts were set according to Table 4.4.

Figure 4.17. 3D finite element model for mechanical analysis.
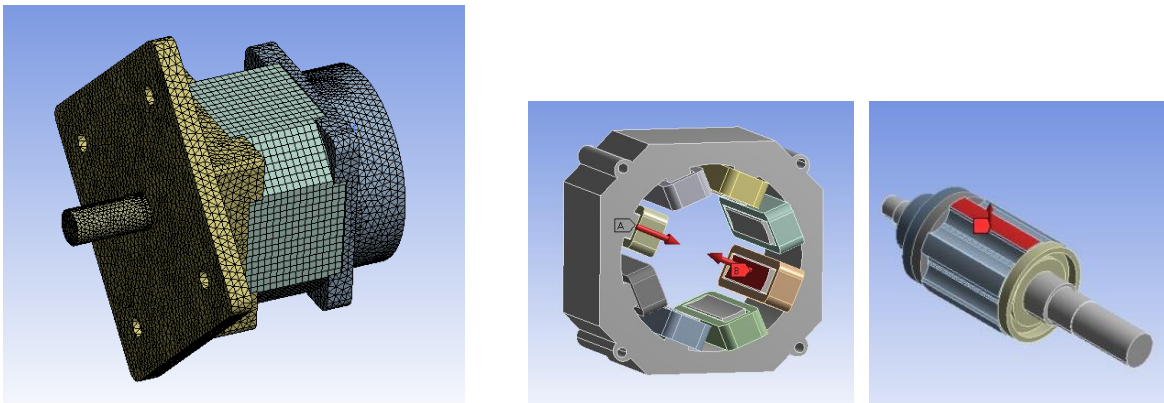
Using the FE model, the modal analysis was evaluated and compared with the experimental modal test. Figure 4.18 and Figure 4.19, respectively, show the stator and rotor natural frequencies and their associated mode shapes obtained from simulation. As can be noticed, the natural frequencies from simulation results and the impact test results are very close. Moreover, the mode shapes ilustrated in Figure 4.19(a) and Figure 4.19(b) are compatible

with the experimental extraction shown in Figure 4.14. The finite element analysis has also confirmed the rotor natural frequency around 7 kHz.

Table 4.3. Materials for different parts in the SRM

Component		Stator and Rotor Lamination	Shaft	Bearing	End plate and press plate
Material		M19	Steel	Stainless steel	Aluminum
Young's modulus (GPa)	E_x	188.7	110	193	71
	E_y	99.39			
	E_z	206.8			
Density (kg/m³)		7850	7850	7750	2770
Poisson ratio	υ_{xy}	0.3700	0.28	0.31	0.33
	υ_{yz}	0.3988			
	υ_{xz}	0.3316			
Shear modulus (GPa)	G_{xy}	11.40	35.156	73.664	26.692
	G_{yz}	14.02			
	G_{xz}	84.42			

Table 4.4. Contacts between components
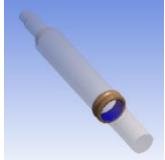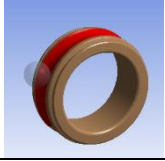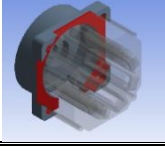
Contact pair		Contact Type
Shaft and inner ring of bearing		Bonded *(No penetration, separation, or sliding between faces or edges)*
Ball and inner/outer race		No separation *(No penetration or separation, frictionless sliding can occur along contacting faces)*
End plate and outer ring of bearing		Bonded *(No penetration, separation, or sliding between faces or edges)*
End plate and stator lamination stack		Bonded *(No penetration, separation, or sliding between faces or edges)*

Figure 4.18. Stator vibration modes.

(a) 1836.5 Hz

(b) 2330.4 Hz

(c) 3841.7 Hz

(d) 5069.1 Hz
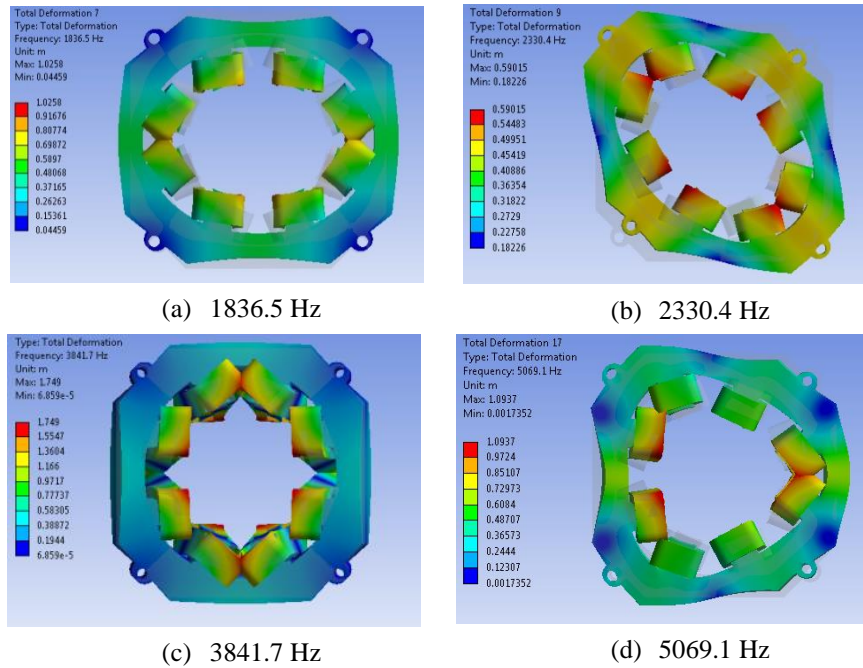
Figure 4.19. Rotor vibration modes.

(a) 2130.2 Hz

(b) 4829.7Hz

(c) 7108.6 Hz

(d) 8804.8 Hz

4.5   Vibration prediction model based on the mechanical impulse response

In the previous section the modal test results provided information on the natural frequencies and vibration modes. Thus, when the motor in operating, if the radial forces contain components which coincide with the natural frequencies of the motor, the structure will vibrate

according to its mode. Additionally, if more than one natural frequency is excited, the total resulting vibration of the motor will be the summation of individual modes. Therefore, the vibration measured in the stator during motor operation is a combination of several modes. In addition, with the motor assembled some cross-coupling vibration also takes place [49].

Hence, many vibration estimation methods reported in the literature consists in obtaining the contribution of each mode and then superimpose them [55]. Basically, natural modes of the stator frame are calculated using structural modal analysis first. Next, modal superposition is implemented by adding the natural modes for configuration of the vibration. Subsequently, the radial electromagnetic force is calculated from the excitation current, and the frequency components of the radial force computed. Finally, the resonance between the force harmonics and the natural frequency response of the vibration modes is analyzed to estimate the overall vibration.
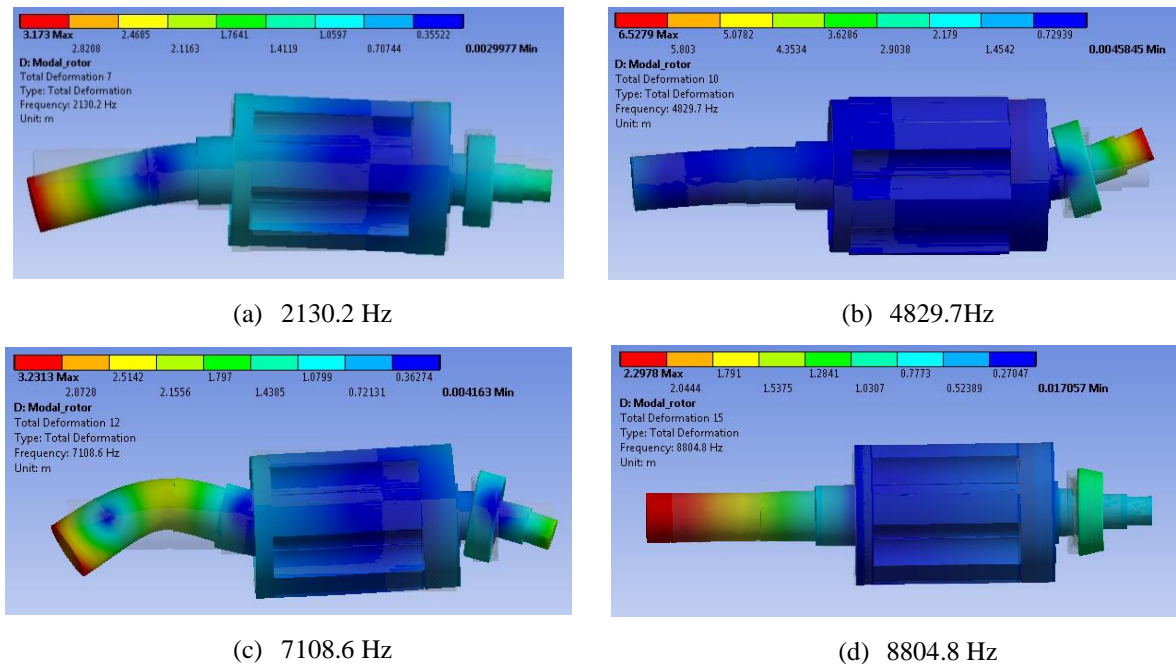
Alternatively, a direct and effective method based on the mechanical impulse response has been presented in [56]. The mechanical impulse response (MIR) provides a link between the time rate of change in the input electric power to a stator phase and acceleration of the stator frame at a targeted point. MIR can be computed using FE magneto-structural analysis of the SRM or can be measured experimentally. Once computed/measure it can be used for predicting the vibration and for optimizations processes: finding optimal excitation or optimal design of the SRM.

Before considering the MIR, let's analyze the change in the airgap length due to deformation of the stator, analytically [56]. This will provide a complete understanding of the origin and mechanism through which vibration in SRM is generated. Although the change in the airgap length is small (microscopic deformation), the phase voltage equation, in the absence of magnetic saturation, can be expressed as follows:

$$v = R.i + \frac{d\lambda}{dt} = Ri + L(x,\theta)\frac{di}{dt} + i\frac{dL}{dx}\frac{dx}{dt} + i\frac{dL}{d\theta}\frac{d\theta}{dt} \tag{4.5}$$

where: $\lambda = L.i \; \rightarrow$ flux linkage
$\theta \; \rightarrow$ rotor position
$x \; \rightarrow$ airgap length
$v \; \rightarrow$ phase voltage
$i \; \rightarrow$ phase current
$L \; \rightarrow$ phase inductance

In eq. (4.5) the input voltage is manly compensated by the back-EMF (i.e. $d\lambda/dt$) which is due to (i) velocity of geometry variation (i. e. dx/dt) that intends to move the poles radially along the airgap, and (ii) the current gradient (i. e. di/dt) which reacts faster because the electrical system has smaller time constant than the mechanical system. Given the fact that the switching times of semiconductor switches are very short, when the converter switches are turned on, $d\lambda/dt$ is dominated by $L\,di/dt$ term (there is no current in the coil) and as such the stator poles almost do not move (acceleration is almost zero).

However, as the switches are turned off, a sudden change in the voltage takes place (from positive to negative). During this sudden transition, a sudden change in back-EMF has to happen to balance the two sides of eq. (4.5). As a result, not only current is changing due to a non-zero flux, stator frame will be subject to sudden motion (i.e. radial vibration) as well. Analytically, this process can be described using the following equation at the switching instant, where the acceleration term comes in sight. Equation (4.6) is derived by differentiating both sides of (4.5) with respect to time:

$$\frac{dv}{dt} = R\frac{di}{dt} + 2\frac{dL}{dx}\frac{dx}{dt}\frac{di}{dt} + L\frac{d^2i}{dt^2} + i\frac{dL}{dx}\frac{d^2x}{dt^2} \tag{4.6}$$

Equation (4.6) implies that the acceleration is also dependent upon the magnitude of current i (relevant to flux level or radial force). Furthermore, a negative time rate of change in the voltage will result in a negative acceleration of the airgap (expansion of the airgap) which is agreeable as the attraction forces acting between rotor and stator are quick fading as the input current decays to zero.

4.5.1 Mechanical impulse response (MIR)

According to (4.6), a step change in the input voltage acts as an impulse to the right-hand side of the equation and in the presence of a phase current (i.e. magnetic flux) the acceleration of the stator ($a = d^2x/dt^2$) will carry the majority of the discontinuity.

Using (4.5), one can compute the instantaneous power as:

$$vi = Ri^2 + i\frac{d\lambda}{dt} = Ri^2 + iL(x,\theta)\frac{di}{dt} + i^2\frac{dL}{dx}\frac{dx}{dt} + i^2\frac{dL}{d\theta}\frac{d\theta}{dt} \tag{4.7}$$

In order to understand the physical meaning of this equation a simple experiment can be performed: with the rotor of the SRM locked at a fixed position, a pulse of voltage is applied to one of the stator phases and the corresponding phase current and radial acceleration of the stator frame at a fixed position is recorded. Figure 4.20 illustrates the experimentally recorded waveforms and the location of the accelerometer. One can note that amid fast turn-on time there no notable acceleration at the turn-on instant while there is a significant acceleration at the turn-off instant. Given the fact that tangential forces in SRM are approximately an order of magnitude smaller than the radial forces, the tangential vibration has not been included in this analysis.

Figure 4.20. Experimental vibration measurement due to a pulse of voltage. (a) Experimentally recorded voltage, current and acceleration. (b) The accelerometer (model 623C01 and its location on the stator lamination.

(a)   (b)
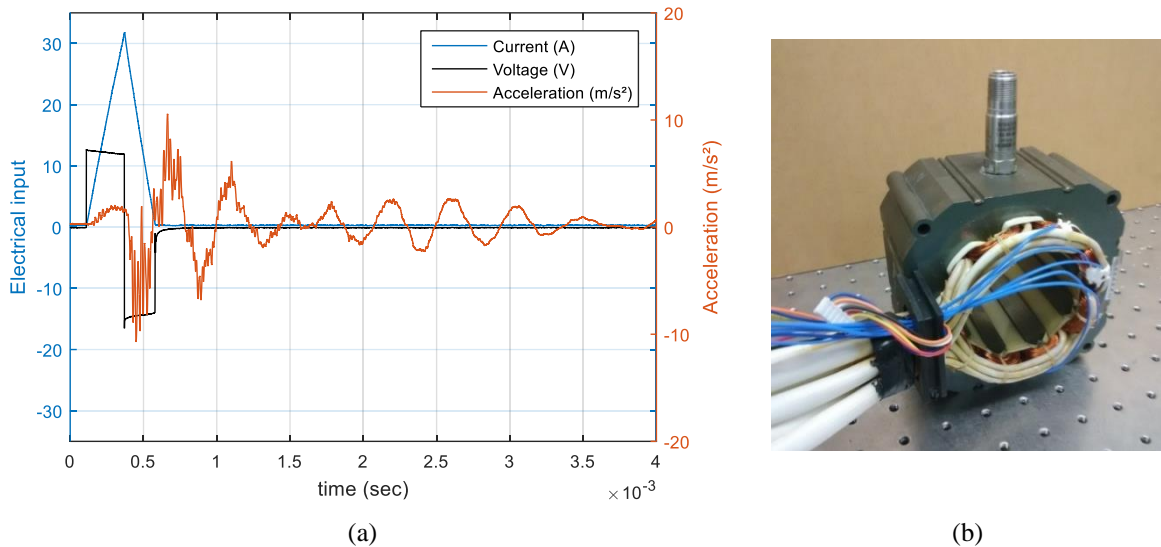
An inspection of the time rate of change in input electric power under the test condition explained above reveals that discontinuities in input power are created by fast switching of the input voltage during commutation of the voltage. The derivative of power is:

$$\frac{dP}{dt} = v\frac{di}{dt} + i\frac{dv}{dt} \cong i\frac{dv}{dt} = Ri\frac{di}{dt} + 2i\frac{dL}{dx}\frac{dx}{dt}\frac{di}{dt} + Li\frac{d^2i}{dt^2} + i^2\frac{dL}{dx}\frac{d^2x}{dt^2} \qquad (4.8)$$

It is important to highlight that equation (4.8) reveals that magnitude of the current and switching levels of the voltage will determine the magnitude of the input impulse into the electromechanical system. In equation (4.8), the term $\left(v\frac{di}{dt}\right)$ is very small compared with $\left(i\frac{dv}{dt}\right)$ and can be neglected in the computations [56]. Given the fact that the switching times of

semiconductor devices are very short, a step changes in the input voltage at turn-on and turn-off instants takes place ($\frac{dv}{dt}$ is to large, mainly if hard chopping in asymmetric bridge is assumed).

Given the SRM characteristics, the relationship between the time rate of change in input power and the acceleration of the stator is different at each rotor position. Therefore, the MIR should be defined at discrete rotor positions spanning from unaligned to aligned position. Figure 4.21 shows the impulse response at different rotor positions. Furthermore, as the inductance changes according to rotor position, the current magnitude will be different for each rotor position if the same duration of the pulse of voltage is applied, hence the measured acceleration in Figure 4.21 must be normalized (divided by the input) before stored in a lookup table for future vibration computations [56]. A resolution of 1degree has been used in collecting all MIR data.

Figure 4.21. MIR at different rotor positions.
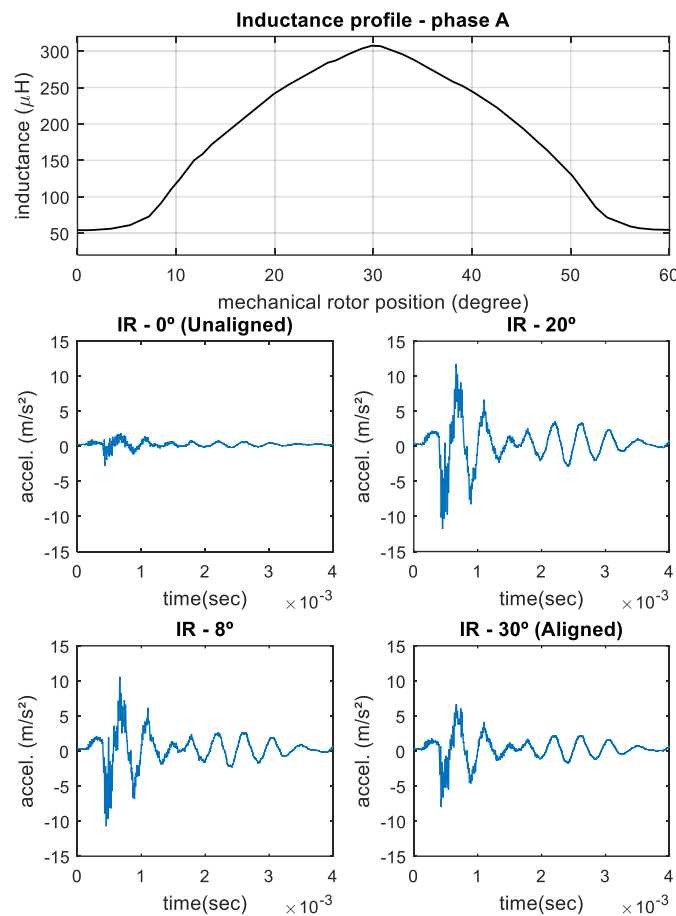
The impulse function for a given current magnitude and at a given rotor position can then be used to obtain the acceleration (vibration) at the targeted point using the convolution theory:

$$a(t)\Big|_{\theta, i} = \frac{dP}{dt} * h_a(i, \theta) \tag{4.9}$$

where $a(t)$ and $h_a(i, \theta)$ denote the acceleration and the impulse response corresponding to a specific rotor position θ and stator current i, respectively.

The MIR creates a direct link between the power electronic converter and the structural response of the machine through which the effects of the fast switching and the structural response of the machine can be studied. More important, since acceleration is experimentally captured through impulse responses, the mechanical modal parameters defined by the body geometry and material are automatically included.

4.6 Prediction of vibration

The time derivative of the input electric power and acceleration at the target point on the stator were treated as input and output of a system, respectively, i.e. the measured acceleration induced by the change of power is considered as the impulse response. Moreover, since the consecutive switching instants are viewed as a series of impulses with opposite signs representing turning on and off instants, the output acceleration can be modeled as a series of impulse responses with opposite signs representing contractions and expansions [56]. Figure 4.22 illustrates this process graphically.

Please, note that a new switching occurs (and therefore a new vibration is introduced) before the vibration caused by the past switching dies out. Therefore, the effects of all switchings will be superimposed.

Considering the location of the accelerometer attached to the stator body, Figure 4.23 shows the microscopic stator deformation (contracting and relaxing) that is captured by the sensor due turn-on and turn-off instants.

To assess the mechanism described, the radial stator acceleration during motor operation at 600 rpm has been predicted. Figure 4.24 shows the electrical input (voltage and current) and the acceleration measured on the stator. Using the current and voltage information along with the MIR, vibration can be estimated. Figure 4.25 illustrates the predicted acceleration in comparison with the measured one. The results demonstrate that the stator vibration signature can be successfully estimated using the mechanical impulse response.

Figure 4.22. Vibration prediction mechanism.

V

i

t1 t2 t3

Change of
power
(impluses)

Induced vibration
(equation 4.9
calculated for V, i
and rotor position at
instant t1)

(+) Superposition

(+)

.
.
.

Accel.

Resulting
vibration due to
all switchings
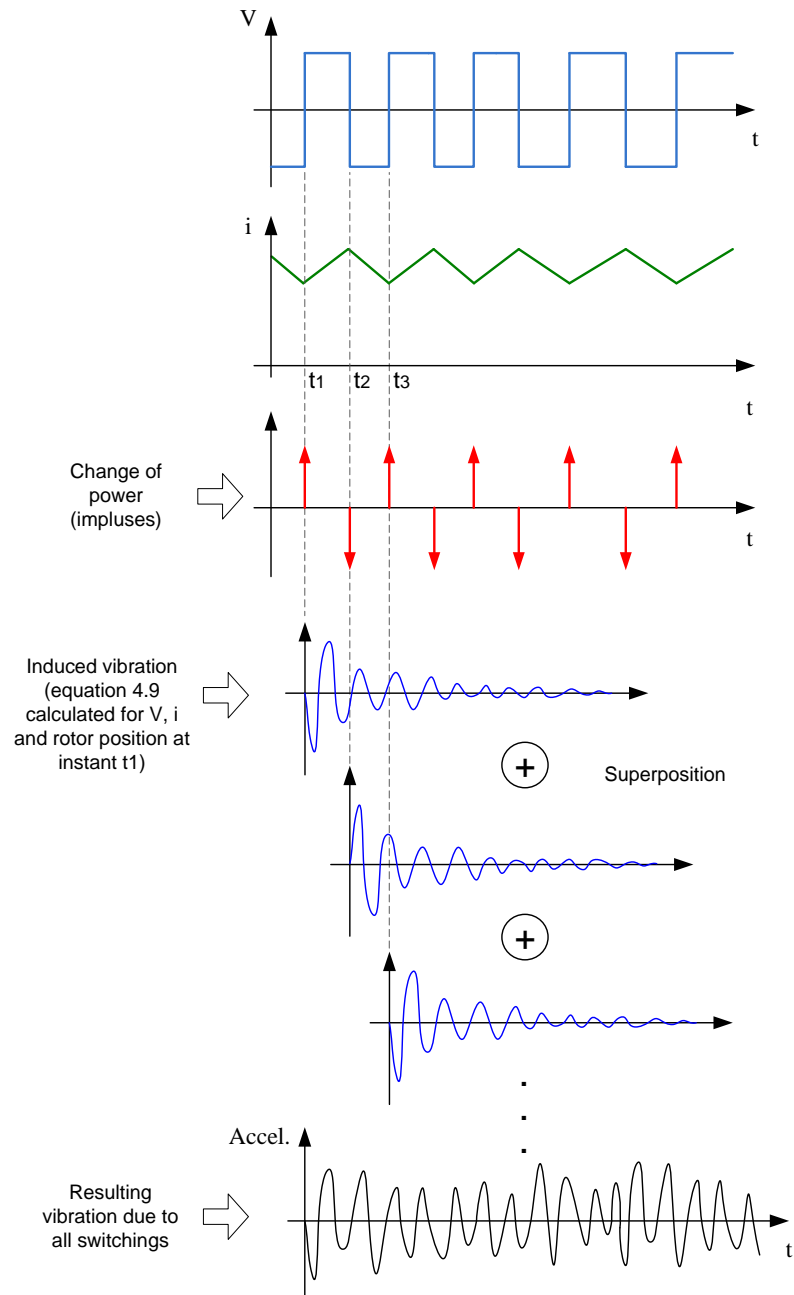
Figure 4.23. Stator deformation due to turn-on and turn-off.

Turn-on

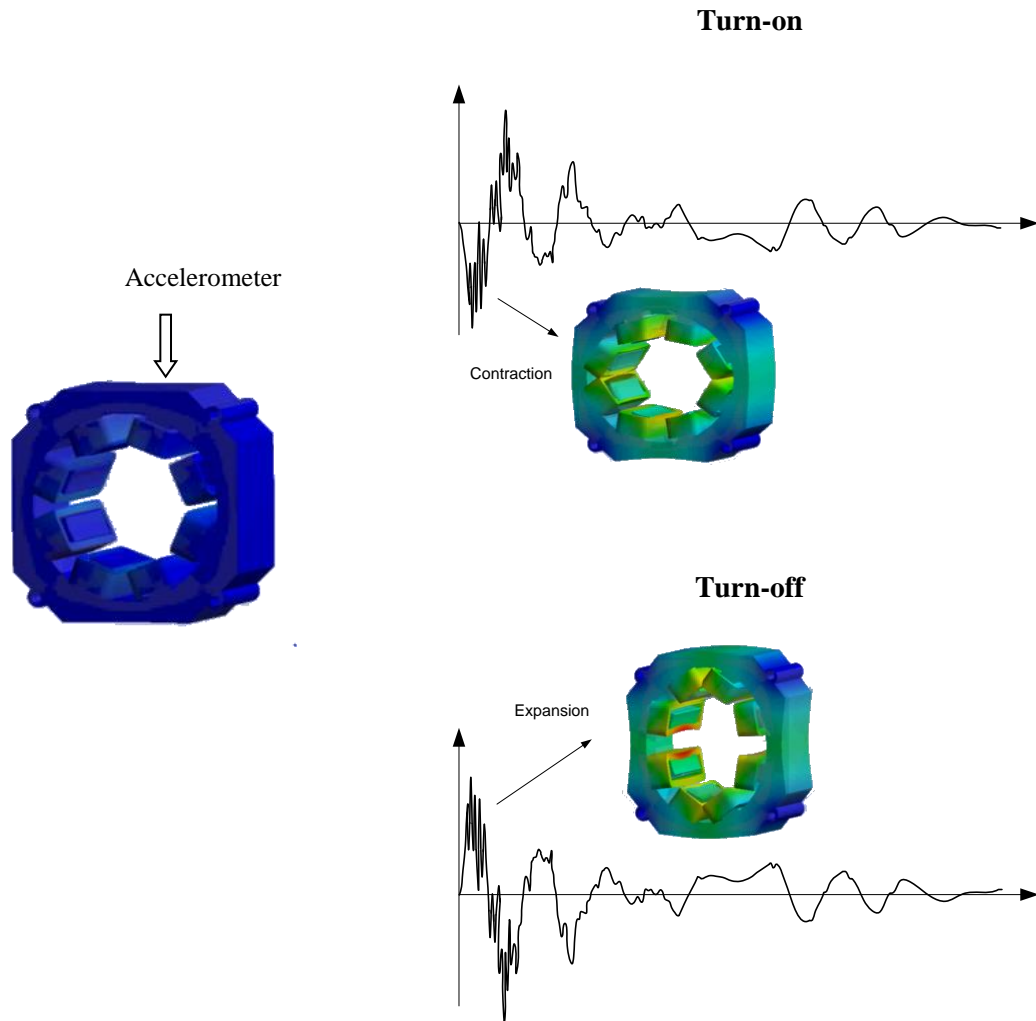
Accelerometer

Contraction

Turn-off

Expansion

Figure 4.24. Phase A voltage and current waveforms and the corresponding stator acceleration at 600rpm.
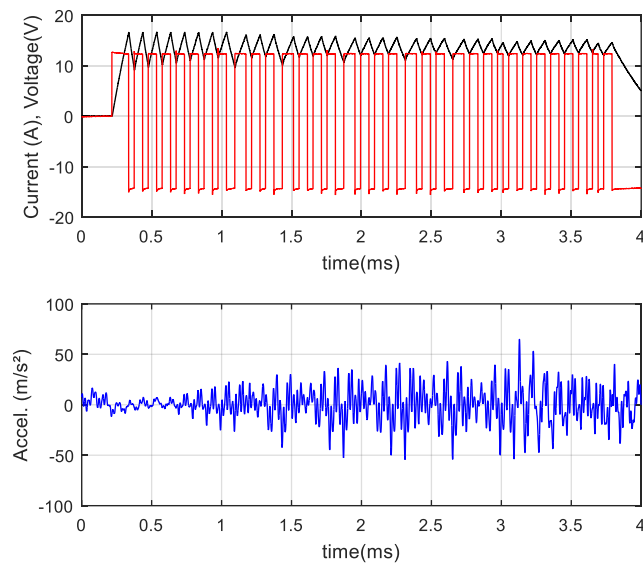
Figure 4.25. Comparison between the measured and estimated vibration due to phase A excitation. Time and frequency domain.
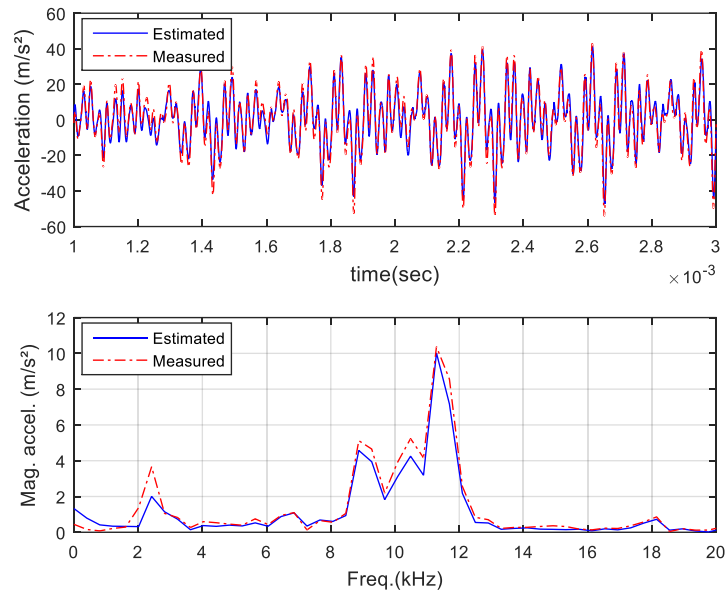
The accelerometer is placed on the stator housing as shown in Figure 4.20(b). Thus, even though the machine is symmetric, the vibration captured by the sensor has different signatures depending on whether the excited phase is closer or farther from the accelerometer location. Therefore, in order to accurately represent the vibration signal as it is measured during motion, the impulse responses should be captured for the four phases and the resulting MIRs stored in look-up tables. Indeed, Figure 4.26 shows the impulse response for the four phases at aligned position and it is possible to note that the signatures are different from each other, even when the rotor is relatively at the same position (for each phase point of view).

Figure 4.26. Impulse responses at aligned position relative to each phase.

Figure 4.27 shows the comparison between the measured vibration and the estimated signal for 3 phases when the motor is running at 1000 rpm. Please, note that in Figure 4.27 the vibration due the fourth phase excitation is not displayed in the estimated signal (approximately after 0.0075s) because during this test, a 4-channel oscilloscope was used to acquire the currents in phase A (ch1), phase B (ch2) and phase C (ch3) while the fourth channel was used to capture the vibration signal from the accelerometer. Therefore, there was no available information about phase D current, and the vibration generated could not be estimated. Despite, the results for the other phases validate the prediction model.

Traditionally, cascaded numerical finite element analysis has been wide applied for estimation of vibratory behavior [57]. However, in this approach, a three-dimensional structural model of the machine is employed to compute the vibration. This process can cause unreasonably long computational time even for the modern computational resources. Access to MIR will allow for optimization of the stator excitation in the existing SRM drive (with substantially less computational effort) to achieve the desirable structural and acoustic response.

4.7   Active vibration cancellation (AVC) in SRM

Among the methods of vibration analysis and control of SRM drives, the work of Pollock and Wu [16] stands out. In early 1990s, they have proved that vibration is greatly reduced by means of active cancellation (AVC), reached by stepping the voltage during the turn-off process
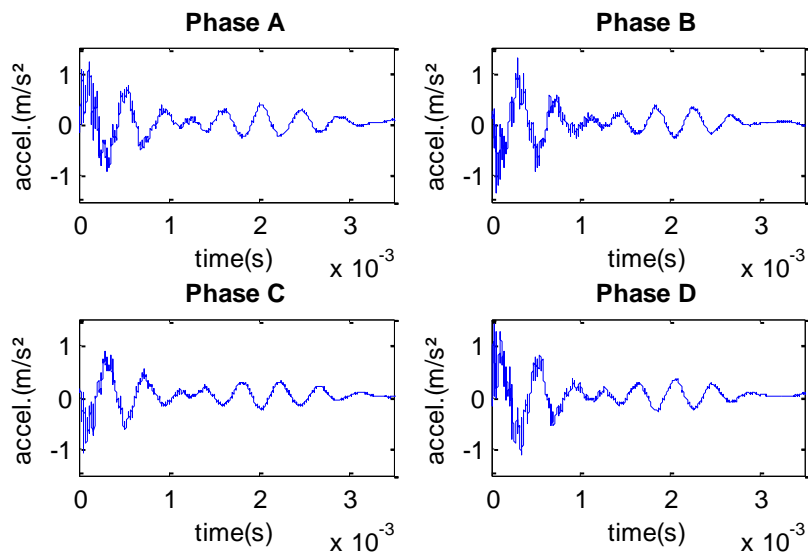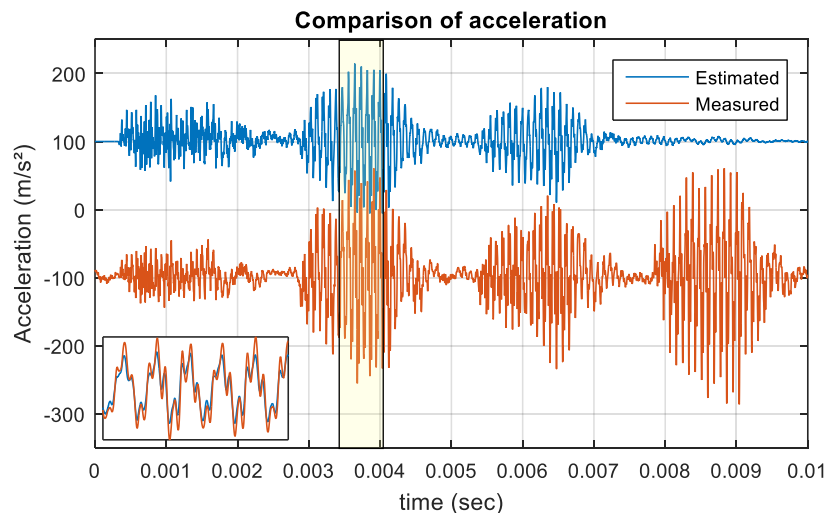
Figure 4.27. Comparison between the measured and estimated vibration acceleration for different phases at 1000 rpm. The highlighted region is zoomed to illustrate the details.

According to this method, a zero-voltage stage is introduced just prior to the turn-off instant leading to a two-step commutation. The winding voltage is first reduced from positive dc bus value to zero, then after a period equal to half-cycle of the dominant natural frequency the voltage across the winding is changed from zero to negative dc input, thereby producing an anti-phase (180 degrees phase shift) vibration with respect to that caused by the first step change in voltage. Please see the Figure 4.28. Accordingly, majority of the resulting vibrations cancel each other, and net vibration is reduced.

Indeed, vibration is an inherent characteristic of SRM, therefore AVC method is a suitable and effective technique to reduce it, instead of trying to avoid it. However, the method presented in [16] is mainly implemented at high speeds at which vibration is induced by only a few numbers of chopping or just once during single pulse mode. Moreover, depending on the speed and frequency of the dominant mode the amount of time required at zero voltage can represent too much of the time delay and it will adversely affect the torque generation. In other words, the delay time between pulses might not be an afforded for current chopping mode at low speeds, especially for SRMs that have small electrical time constant and low mechanical natural frequencies.

Therefore, this research aims to propose a new control strategy that incorporates the AVC at low speed operation. Before going through the proposed method, it is important to understand the vibration production under hysteresis current control. At low speed, the rate of rise in current is high due to the small back-emf and thus peak current must be limited by chopping. In this case, hysteresis control is commonly used in switched reluctance motor (SRM) drives due to its simplicity and fast response.

As stated before, the sudden change in the input electric power plays an important role in the amplitude of the vibration and the hysteresis control naturally consists of a sequence of switchings in order to keep the current within an upper and lower band. To better investigate the vibration response under hysteresis current control, a simple experiment has been performed in the SRM drive at 500 rpm. The test consists in applying different hysteresis current bands. Figure 4.29 shows the phase A current waveform with two different hysteresis bands along with the corresponding accelerations. Analyzing these results and considering the concepts explored in the previous sections, one can conclude that: as the band is changed, the switching instants are shifted, and this introduces a noticeable impact on the recorded acceleration. Specifically, as the current turns on and off, a reinforced vibration may be produced in some instants, whereas at other instants there may be some active cancellation taking place. Therefore, this

investigation provides a valuable observation that there might exist an ideal switching instant for each turn-on and off resulting in an optimally mitigated vibration.

Figure 4.28. Principle of active vibration cancellation.

$$t_z = \frac{1}{2 . f_n}$$
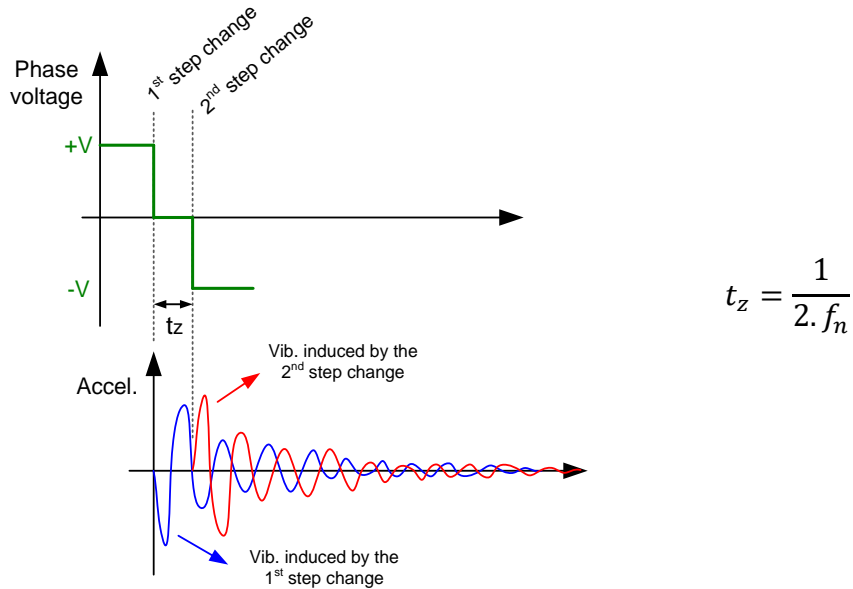
4.7.1 Proposed strategy

The mechanism introduced by Pollock and Wu is suitable for single pulse mode control in which there is more room to accommodate the timing corresponding to the half-period of the dominant natural frequency. In addition, the contribution presented by [56] has proven that vibration can be successfully predicted using the mechanical impulse response.

Figure 4.29. Stator acceleration for different hysteresis current band at same condition (torque and speed).
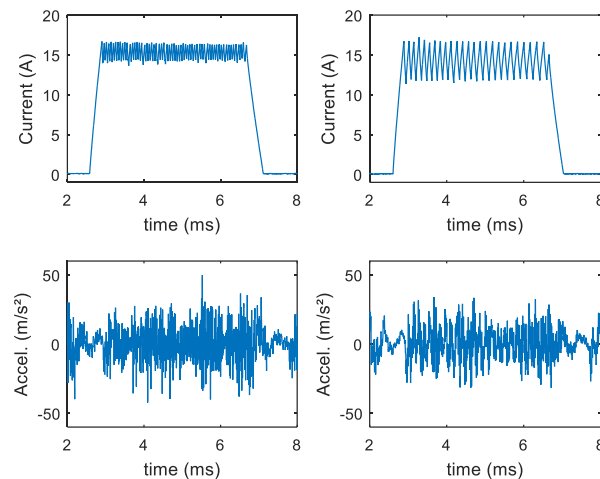
Hence, in this research a new AVC strategy has been developed to cover the low speed region based on the understanding of the vibration from the impulse response point of view. As previously discussed, every time a sudden change of the radial forces occurs, a severe stator vibration takes place, therefore the method consists of finding the optimal instant for each switching in such a way that the vibration created by the upcoming switching would partially cancel the vibration produced by the previous switchings. In conventional hysteresis current control, the switching instants are defined by the timing at which the current reaches upper and lower limits, however, in some cases it would be benefit for vibration to have the switching just few milliseconds later (or earlier).

Thus, in this new method the switching instants are well-defined, with the pattern designed to evidentiates the cancellation effect. It should be clear that by changing the switching instants, the vibration induced due to each step change is shifted given a reduced overall vibration (after superposition). For the current point of view, this mechanism will result in a dynamic current band instead of having a fixed upper and lower limit, leading to a current profile that will not necessarily present a uniform and flat-top shape.

It also must be noted that the present study only focuses on the influence of magnetic forces. Forces of mechanical nature such as centrifugal and aerodynamic forces are not considered as their impact is significant at ultra-high speeds.

The vibration optimization routine was developed in MATLAB (Appendix II) and has two main calculations: the first one is the current estimation through an analytical expression and the second one is the prediction of the acceleration. The vibration amplitude depends on the input power variation, then if the switching instant is modified the current value must be estimated for the desired instant. Therefore, for each instant of time (switching time) tested within the search domain, the current is calculated and used with MIR to estimate the acceleration according to eq. (4.9). The voltage and speed are considered constant.

The current estimation in each instant is given by eq. (4.10), derived from phase voltage equation [3]:

$$i(t) = i_0 . e^{-\frac{t}{\tau}} + \frac{V_{DC}}{R_{eq}} . \left(1 - e^{-\frac{t}{\tau}}\right) \tag{4.10}$$

where $R_{eq} = R_s + \omega \frac{dL}{dt}$ and $\tau = \frac{L(i,\theta)}{R_{eq}}$

In the instants design process, a comprehensive search will be used because the search domain is limited, i.e. the algorithm has constraints to avoid a large current variation, and consequently torque ripple. The relevant limitations are: i) after a switching occurs, the new switching cannot be too close because of the switching frequency limit; ii) after a switching occurs, the next one should not take too long (if the previous is a turn-on and the control takes too much time to turn off, the current will achieve a high amplitude, likewise, if the previous switching is a turn-off and the next turn on takes too long, the current and consequently the torque can decrease to zero). The described fact is especially noticeable if the electrical time constant of machine is very small, so the slope of the current rise and decay would become very large. Figure 4.30 shows the search region during turn off and a similar idea is used for turning on. It is important to highlight that the search domain is adaptive along the conduction period. Nearby the turn on phase commutation the inductance is smaller and the current rise (or decay) is faster. In this case the t_{max} also has a small value. On the other hand, close to the turn off phase angle, the inductance is bigger and therefore, a higher t_{max} limit is tolerable. Depending on the operating speed, the back-emf also limits the rate of current variation and this parameter needs to be properly tuned.

Considering the current and switching frequency boundaries the algorithm to find the best instants to switch is represented in the flowchart shown in the Figure 4.31. The search domain (between t_{max} and t_{min}) is discretized in small time steps. Knowing the last switching instant (suppose it is a turn-on) and the overall vibration caused by the previous switchings, the effects of applying a switching off at t_{min} is tested. Basically, the current amplitude is calculated, hence the induced vibration is computed through (4.9) and added to the vibrations signal caused by the previous commutations so far. The effect of introducing the new vibration at t_{min} is assessed calculating the variance of the whole vibration. Later, the vibration response is tested again, but now considering having the switching at $t_{min} + \Delta t$, vibration is re-calculated as well as the variance. This process is repeated until t_{max}. The time instant that gives the lower variance is chosen as the optimal instant.

Using methodology described, every new commutation (on or off) will induce a vibration aiming to have a maximum cancellation. Figure 4.32 shows one of the optimization iterations where the new acceleration (red signal) is introduced at the instant that provides the active cancellation (anti-phase signal) with the remaining acceleration (blue signal), resulting in a lower net vibration (magenta). Both signals (red and blue) are separated by the ideal time period between one switching and the next.

Figure 4.30. Search region for optimal turn off switching considering the boundaries.
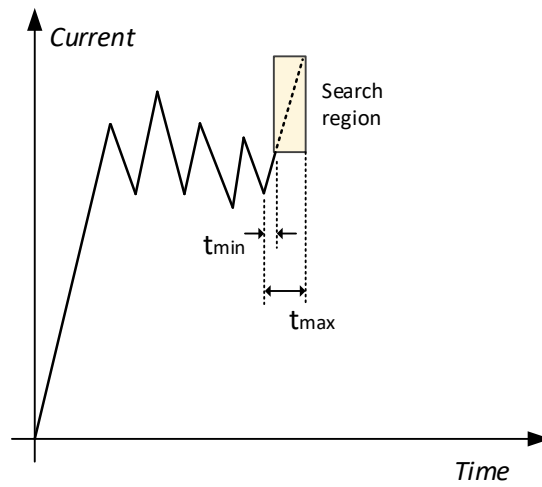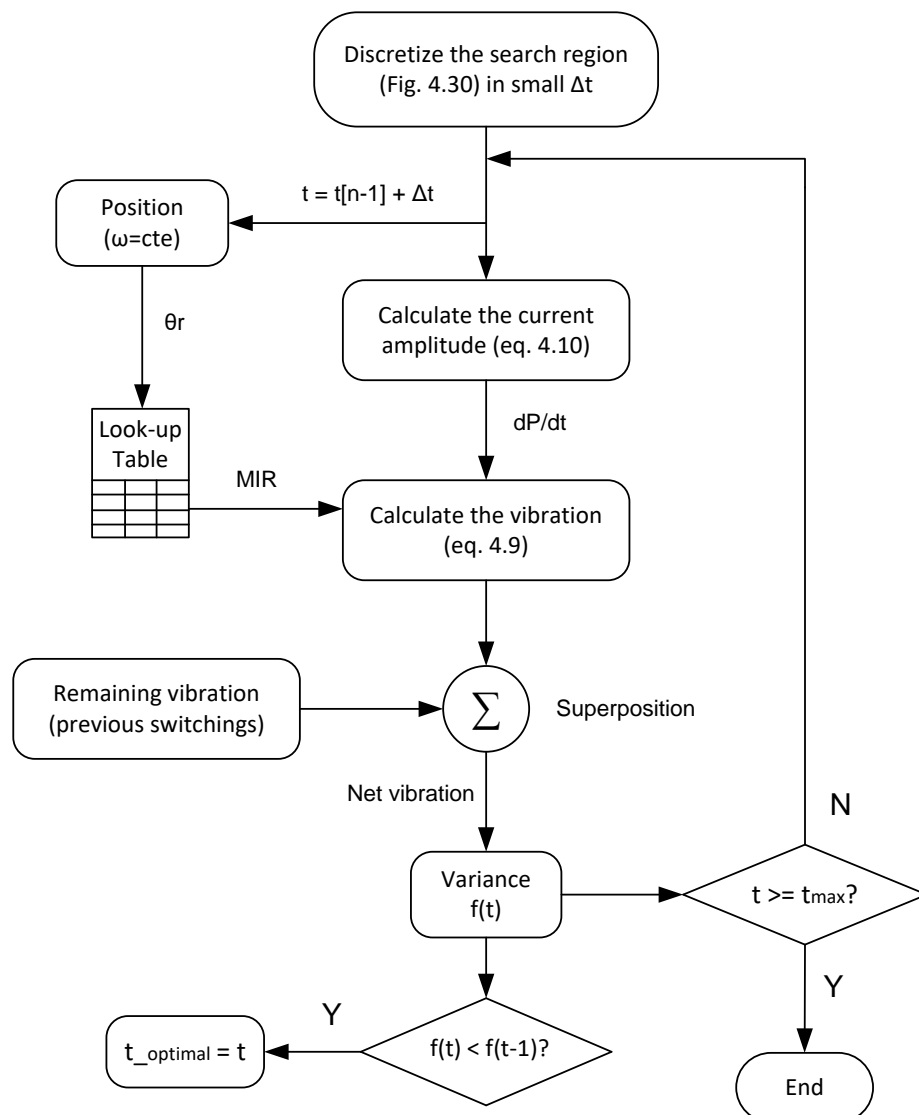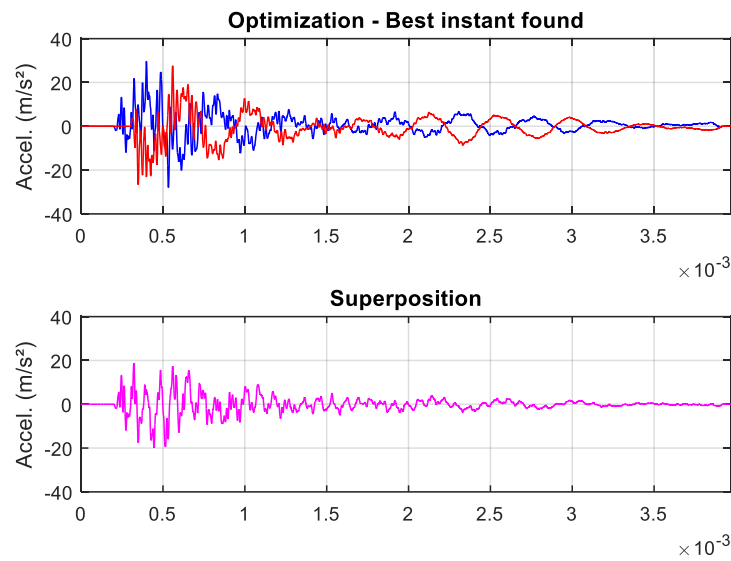

Figure 4.31. Optimization process.

Figure 4.32. Optimization iteration.

4.7.2 Experimental verification

The AVC is obtained by tuning the turn-on and off instants. By switching the phase voltage according to the new instants (rotor position) the current will assume a non-uniform shape. Also, since each phase causes a different acceleration and the upcoming phase attempts to cancel some remaining vibration from the previous phase, the phase current profile is different from each other. In other words, the best switching instant for one phase is not necessarily a good instant for another phase.

The estimated current waveforms for all the four phases given by the optimized switching pattern for operation at 900 rpm, 0.132Nm and considering 12 degrees conduction, are shown in Figure 4.33.

The experimental verification was conducted using the test bench shown in Figure 4.34.

Figure 4.33. Current profile obtained by switching the phase voltage according with the optimal instants for radial vibration mitigation.
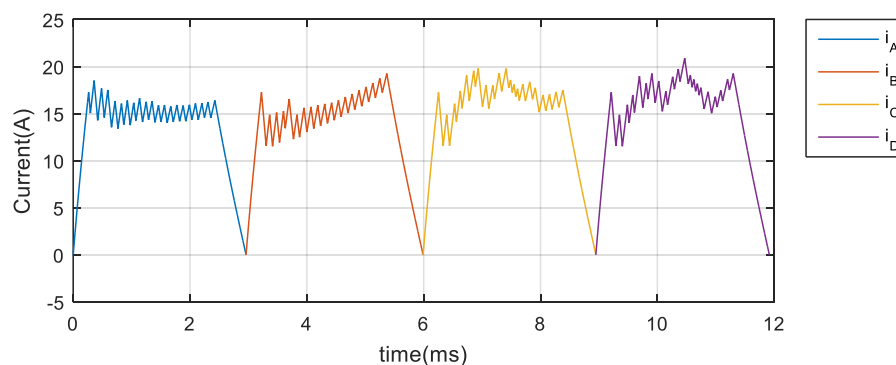
The optimal switching instants were stored in a look-up table and imported in the DSP F28379s memory. The SRM is driven using an asymmetric bridge converter and a PMDC motor has been used as load.

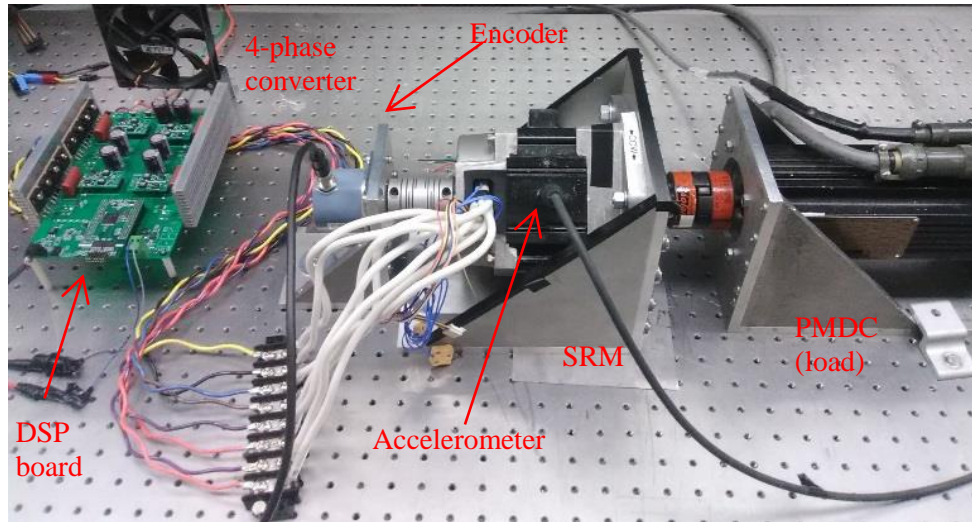Figure 4.34. Overview of the experimental setup.

Figure 4.35 shows the experimental 4-phase current waveforms using the optimized switchings pattern. To verify the effectiveness of active cancellation the SRM drive was first operated under conventional current regulation. Figure 4.36 shows the oscilloscope screenshot for the phase currents and the acceleration measured on the stator frame when the conventional hysteresis current control is applied. Exciting the stator windings with the currents showed in Figure 4.35, the results depicted in Figure 4.37 are obtained for the same operating point. As noticeable the radial vibration amplitude is largely reduced by using the proposed method in comparison with the flat-top current excitation.

A comparison in time domain between the estimated acceleration (simulated) using the modified switching instants and the measured vibration before and after optimization is shown in Figure 4.38. This comparison also illustrates that the acceleration measured after optimization is very close to the expected signature obtained from the model. Figure 4.39 shows the same comparison in frequency domain and reveals that although some components around 8-9 kHz have been amplified, the most dominant frequency components were largely attenuated. The vibration components are related to the natural frequencies; hence the new proposed switching pattern excites the mode at 8-9 kHz while attenuates others.

Figure 4.35. Experimental phase currents waveforms – Optimized switching for 900rpm and 0.132Nm.
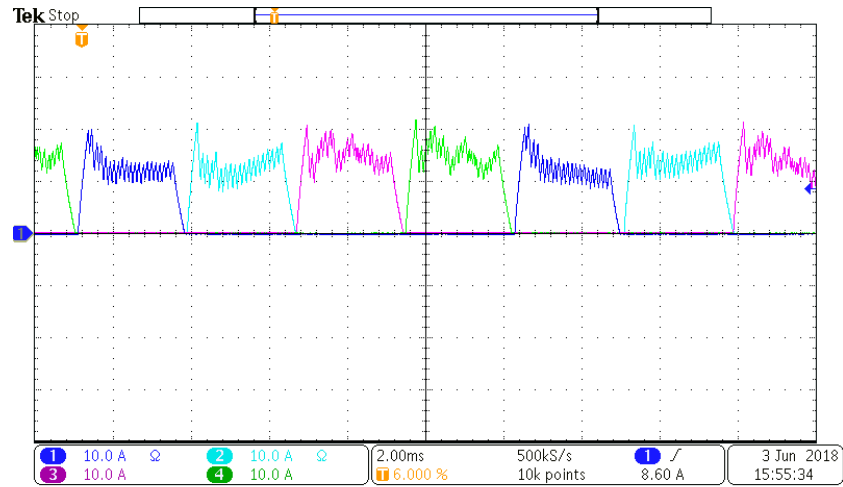

Figure 4.36. Experimental phase current waveforms (ch1, ch2 and ch4) and stator acceleration (ch3) using the conventional hysteresis current control at 900 rpm and 0.131Nm.
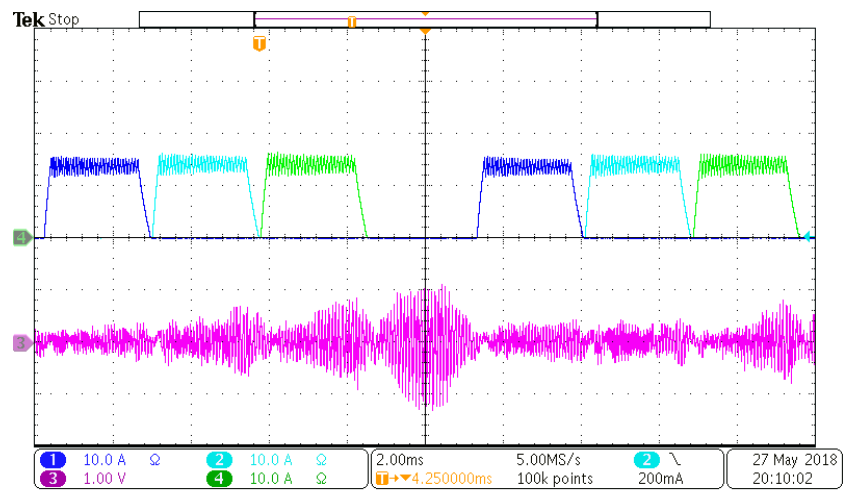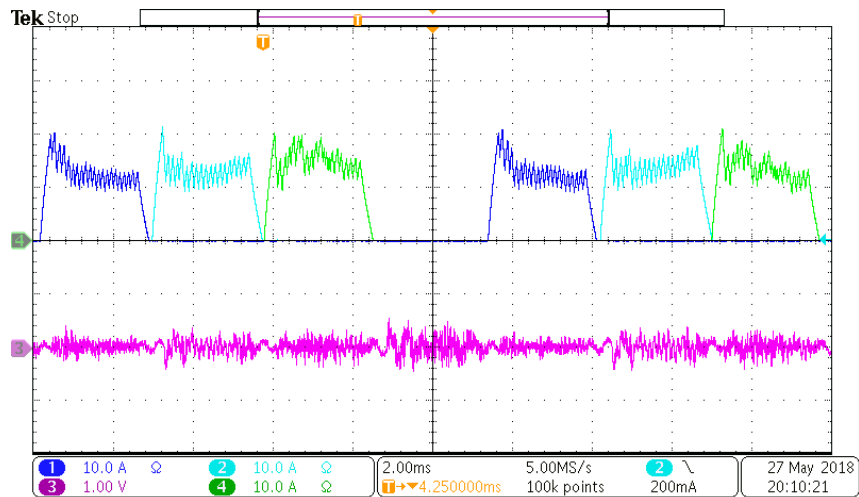

Figure 4.37. Experimental phase current waveforms (ch1, ch2 and ch4) and stator acceleration (ch3) with the proposed current profile at 900 rpm and 0.131Nm.

To assess the vibratory behavior in all the audible frequency range, the total energy (W) is computed through the expression [58]:

$$W = \int_0^{f_{max}} a(f).a^*(f)df \tag{4.11}$$

where, $a(f)$ is the magnitude of the acceleration (FFT) at the frequency f and $a^*(f)$ is the complex conjugate of $a(f)$. Thus, using (4.11) the vibration energy is found to be reduced by 72%.

Figure 4.38. Comparison of acceleration in time domain.
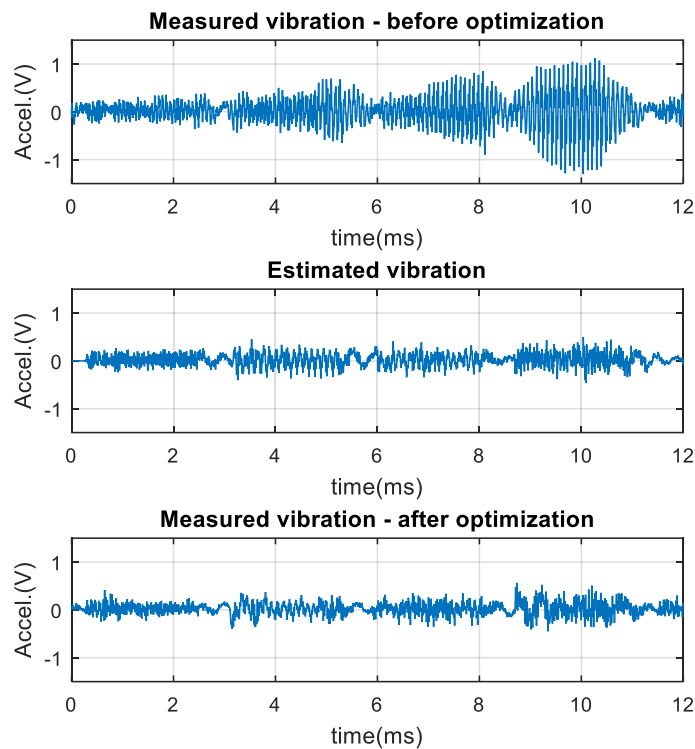
In order to investigate the impact of the new current profile on the torque generation, an in-line torquemeter was installed between the SRM and the load as shown in Figure 4.40. The torquemeter has a linear output with the maximum torque of 11.3 N-m corresponding to 5V. Figure 4.41(a) shows the phase current waveforms and the average torque measured under conventional operation. Figure 4.41(b) depicts the same measurements when the optimized vibration control is applied. Analyzing the RMS value of phase currents and the output torque one can conclude that the torque per Ampere ratio is barely affected by using the new excitation.

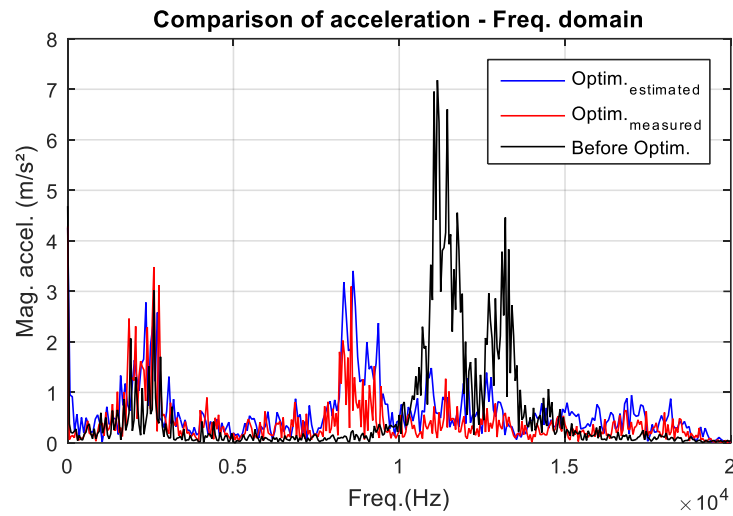Figure 4.39. Comparison of acceleration in frequency domain.

Figure 4.40. Torquemeter installed between the SRM and load.
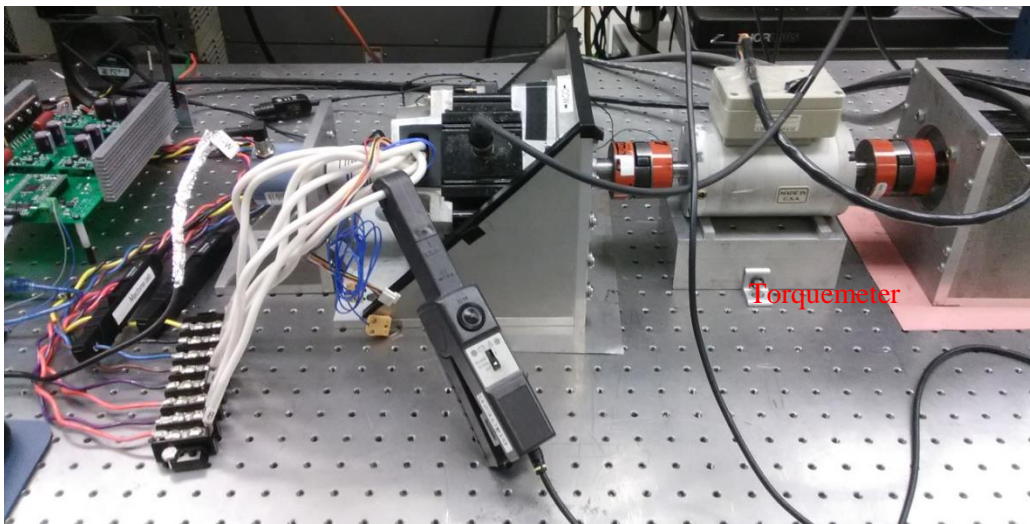
Additionally, the vibration mitigation was also investigated for other operating points. Figure 4.42 shows the optimal phase currents profile obtained for 1200 rpm and 0.308 Nm. The whole optimization process took less than 2 minutes to complete the four phases switching pattern. Figure 4.43 shows the measurements due to the conventional excitation and Figure 4.44 depicts the optimized scenario. Once more, the vibration has been suppressed. The percentage reduction computed through (4.11) is approximately 69%.

To cover the overlap condition, the method is also tested at 1500 rpm and considering the multi-phase excitation. Furthermore, to confirm the overall vibration reduction, in this new test the radial acceleration was also recorded at a second point on the stator frame.

Figure 4.41. Torque measurement at 900 rpm. (a) Conventional hysteresis control ($T_{ave} = 0.1317Nm$)
(b) Proposed method ($T_{ave} = 0.1319Nm$).
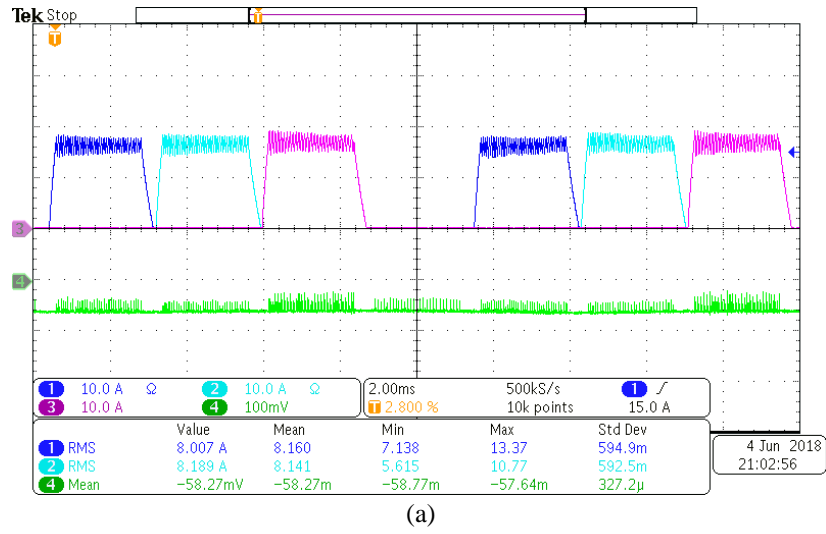
(a)
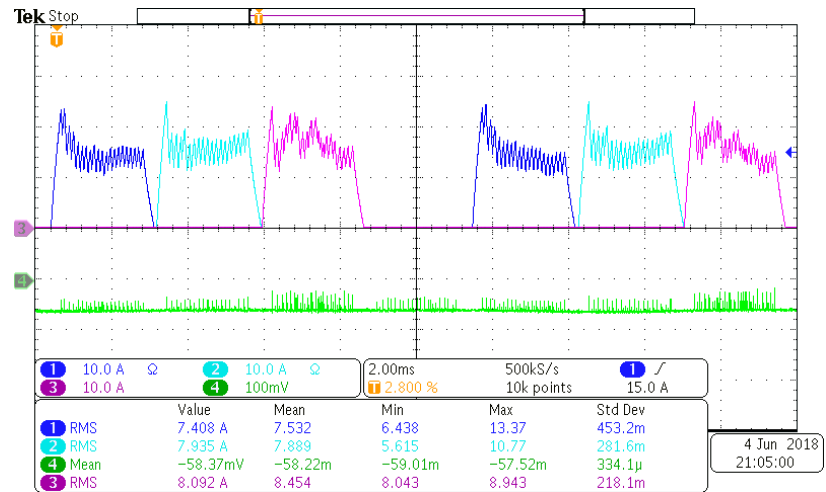
(b)

Figure 4.42. Current profile obtained for 1200 rpm and 0.308 Nm.
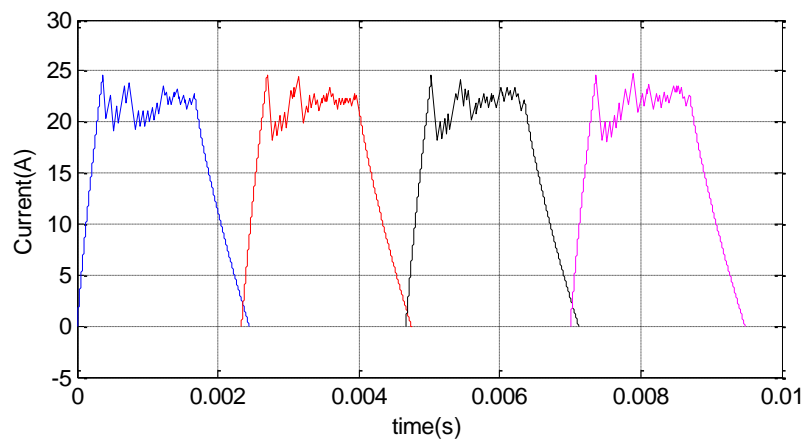
Figure 4.43. Experimental phase current waveforms and stator acceleration using conventional excitation at 1200 rpm and 0.308 Nm.
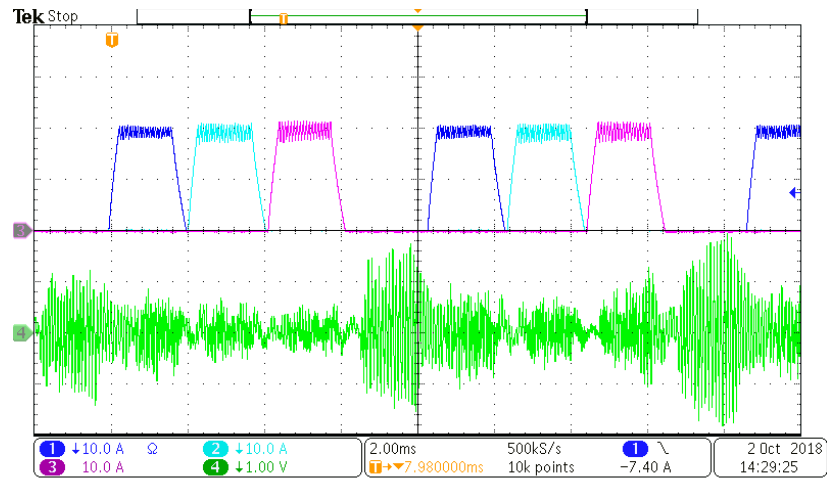
Figure 4.44. Experimental phase current waveforms and stator acceleration using the optimized excitation at 1200 rpm and 0.308 Nm.
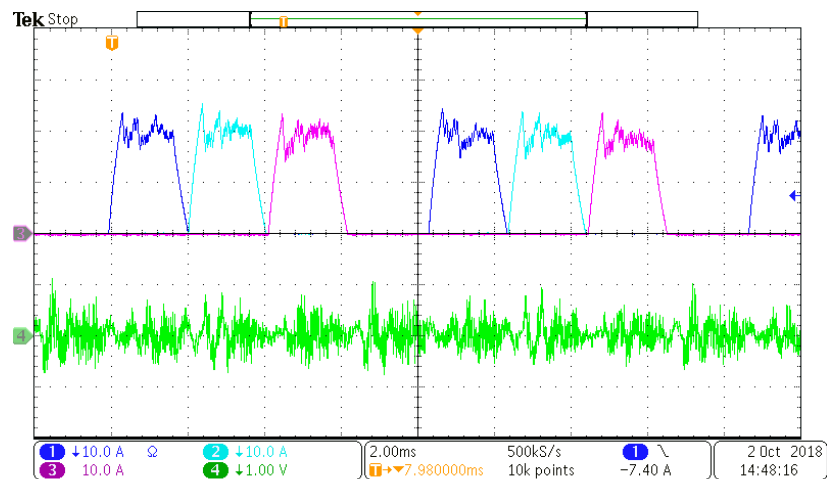
Figure 4.45 shows the theoretically computed current waveforms for the new operationing condition. Figure 4.46 and Figure 4.47 shows the experimental waveforms captured in the oscilloscope before and after optimization, respectively. The green signal is the acceleration measured in a second point on the stator. As one can observe, the method was capable to attenuate the radial vibration through active cancellation for different conditions and at different points located on the stator as observed in both acceleration measurements.

The results have shown that the AVC is possible for low speeds operation. Vibration amplitude has been significantly reduced, which in turn helps to attenuate the acoustic noise. The difference between the proposed method and the method of Pollock and Wu is that in their control, the phase is commuted off only one time (single pulse mode). In this research, the

current regulation is considered, hence many turn-ons and off happens requiring having all the commutation instants tuned.

Figure 4.45. Phase current profiles for excitation overlap at 1500 rpm.

Figure 4.46. Experimental waveforms at 1500 rpm for normal operation. Ch1 and ch2 are the phase currents and ch3 and ch4 are the acceleration measured on the stator.
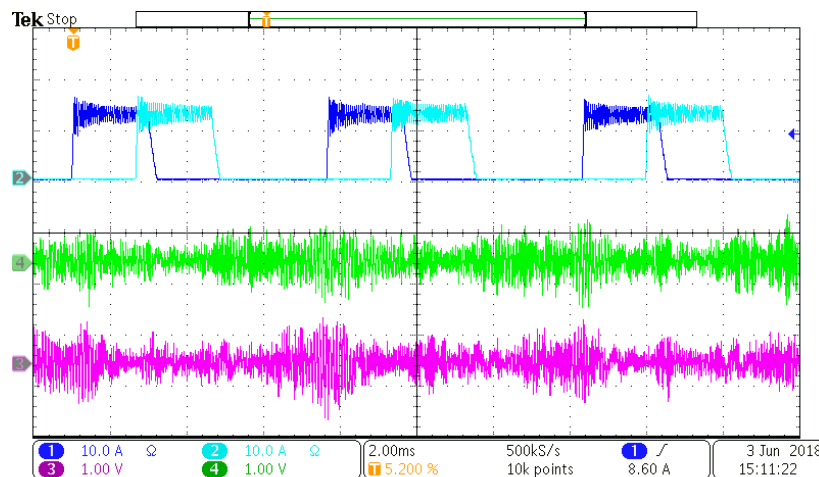
4.7.3   Acoustic noise reduction

The radial vibration radiates acoustic noise through the air and thus, by reducing the vibration amplitude, some acoustic noise reduction is also expected. To verify the acoustic noise reduction, an acoustic camera was used to capture the noise image from the SRM operating under conventional hysteresis current control and with the new proposed switching instants for the 900 rpm operation point. The camera is a 32 microphones array ring which was positioned 1 meter away from the SRM as shown in Figure 4.48. All the data was acquired using the NI PXI-1033 and the image generated by the software. Figure 4.49(a) shows the measured noise picture before optimization and Figure 4.49(b) shows the results for the optimized control.
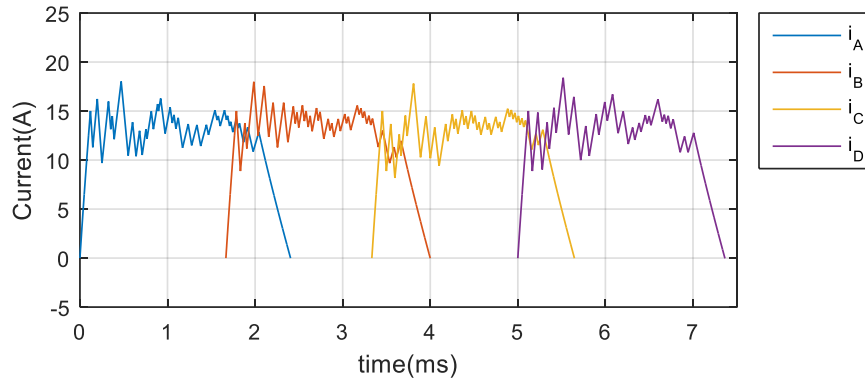
Figure 4.47. Experimental waveforms at 1500 rpm for optimized vibration. Ch1 and ch2 are the phase currents and ch3 and ch4 are the acceleration measured on the stator.
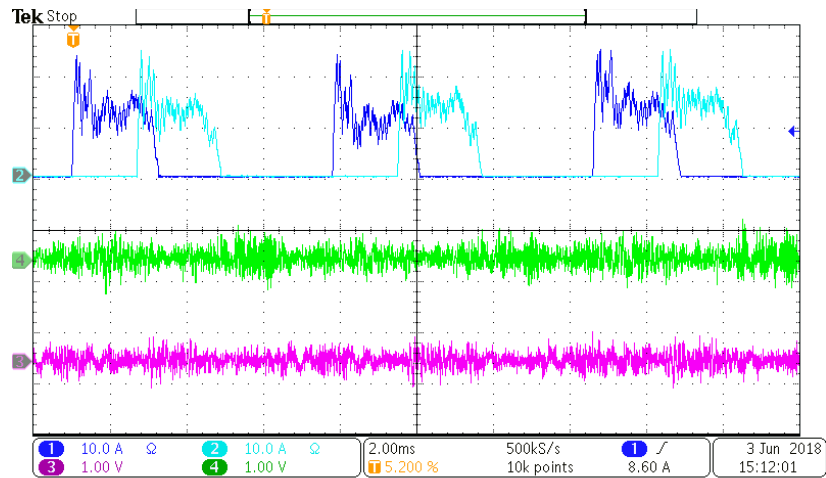
Figure 4.48. Noise measurement using an acoustic camera.

Comparing both figures the sound power level is found to be reduced by 6 dB. Similarly, in the case of running at 1500 rpm and phase overlap the measured noise shows a reduction of 7.1 dB after optimization. In this case, at higher speed, the back-emf helps to decrease the current rising/falling rate. Therefore, during the conduction period, a lower number of switchings occurs and optimizing these switchings a better performance unfolds.

Figure 4.49. Acoustic noise image. (a) Before optimization. (b) After optimization.
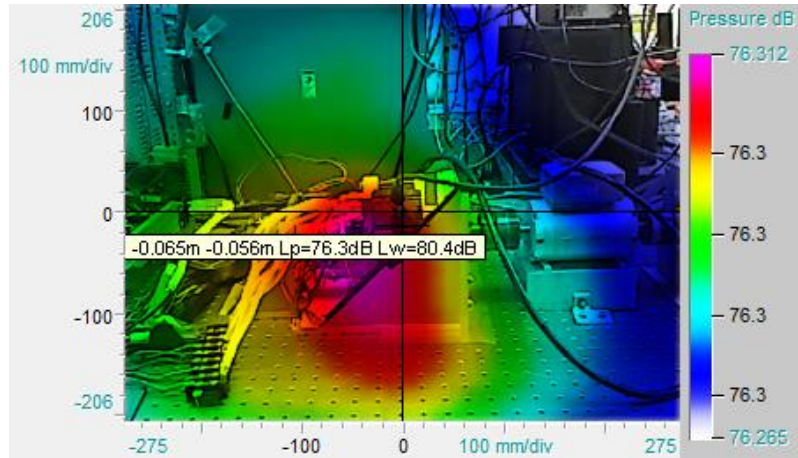
(a)
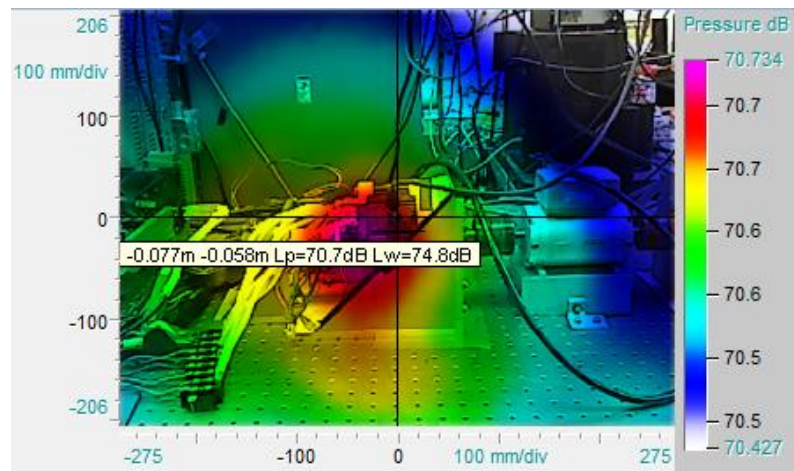
(b)

Chapter 5

Torque ripple mitigation

In this chapter, the mitigation of torque pulsation in SR drives is addressed based on current profiling. An iterative optimization procedure using the Field Reconstruction model is developed to find the current shape that minimizes the torque ripple. Simulation and experimental results are presented to verify the effectiveness of the proposed excitation in achieve a smooth profile. Furthermore, the effect of the new excitation in the structural vibration is also investigated and subsequently, a multi-objective optimization using an adaptive hysteresis current band is proposed aiming to simultaneously reduce vibration and torque pulsation. Experimental tests are conducted to validate the claims made in this strategy.

5.1   Origins of torque ripple in SRM

The electromagnetic torque in SRM is developed by the tendency of the rotor to adopt a position aligned to the excited stator pole, i.e. torque is generated towards the direction such that the reluctance is minimized (or maximum phase inductance). The instantaneous torque generated in each phase is time-varying, its magnitude is proportional to the slope of inductance and the square of the phase current, which is controlled by the converter and the torque control scheme. Since the torque is proportional to the square of current, it can be developed regardless of the direction of the current. The polarity of torque is changed due to the slope of inductance. During motoring mode of operation, a stator phase is excited when its self-inductance is increasing (i.e. rotor is moving from unaligned towards the aligned position) [3]:

$$T_e = \frac{1}{2} i^2 \frac{dL(\theta, i)}{d\theta} \tag{5.1}$$

For smooth and efficient performance at some particular speed and load condition the current must be initiated and commutated at certain rotor angles in relation to the rise and fall of the stator inductance [7]. Accordingly, if improvements in torque profile are to be achieved,

the excitation current (shape and turn-on/off angles) and /or the phase inductance $L(\theta, i)$ are to be modified.

In Chapter 3, the static torque profile was experimentally obtained over a rotation between 0° (unaligned) to 30° (fully aligned) for one of the phases. From Figure 3.7(b) it is observed that the instantaneous torque magnitude and its average depend on the profile of the excitation current waveform and its timing relative to the rotor position. It is noticeable that even for a constant current, the generated torque undergoes a reduction as the rotor approaches to the complete alignment with the stator pole (at 30°). This non-linear characteristic can contribute to the torque ripple formation.

In addition, the continuous rotation movement in SRM is obtained by exciting successive stator phase windings in sequence according to rotor position. The total output torque is the sum of the torque generated due to the currents in the outgoing phase and the current in the incoming phase, which are controlled independently. Although this characteristic provides the fault tolerant capability, this switched operation leads to a torque-dip that occurs near the commutation from one phase to the next. As a result, the total output torque developed at running condition presents a pulsating profile, as shown in Figure 5.1.

Figure 5.1. Experimental measurement of dynamic torque profile.
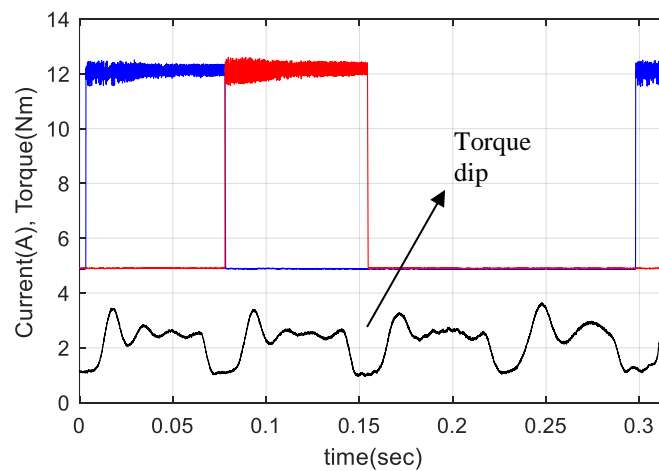
Mathematically, the ripple is defined as the difference between the maximum and minimum instantaneous torque expressed as a percentage of the average torque at steady state operation:

$$\Delta T = \frac{(T_{máx} - T_{mín})}{T_{av}} \cdot 100\% \qquad (5.2)$$

5.2 Torque Profile Optimization

There are many factors contributing to the development of ripple in the output torque of SR motors, among them, rotor and stator shape, air gap length, control and switching strategy, as well as the shape of the current applied to the phase windings. Accordingly, three main approaches can be adopted for the problem of the reduction of the torque oscillation: the first is to improve the magnetic design of the machine, the second is to control the on and off switching angles between the phases while the latter is based on controlling the excitation current waveform. In the following optimization proposal, the strategy is to act on the profile of the excitation current.

As already stated in this dissertation, for low speed region (up to base speed) the hysteresis current control is commonly adopted; the current is regulated to vary within upper and lower limits around a reference value. Accordingly, the current excitation approaches to a square-shaped waveform and it will naturally lead to torque ripple generation. To better observe this behavior, a conventional flat-top square current was applied in the stator phase windings in a co-simulation model developed in ANSYS Simplorer and showed in Figure 5.2. In this simulation the Maxwell 2D model developed in Chapter 3 is connected to the converter circuit, controlled by a logic dependent upon rotor position.

Figure 5.3 shows the simulated phase currents and the correspondent dynamic torque profile at 940 rpm. The conduction angle is 15° (stroke angle) and in this case one can note the presence of some pulsation in the torque. For a sensitive application, this kind of profile might not be acceptable.

In a simple way, an electric machine can be viewed as a current to torque transducer, thus it is intuitive that when the torque decreases, higher current is needed to produce more torque. Indeed, torque production in an SR motor is proportional to the amount of current put into the windings and an increase in the excitation will compensate the torque dip. Therefore, an optimization process is performed to find the current profile required to minimize torque oscillations. The optimization routine methodology is depicted graphically in Figure 5.4 [59].

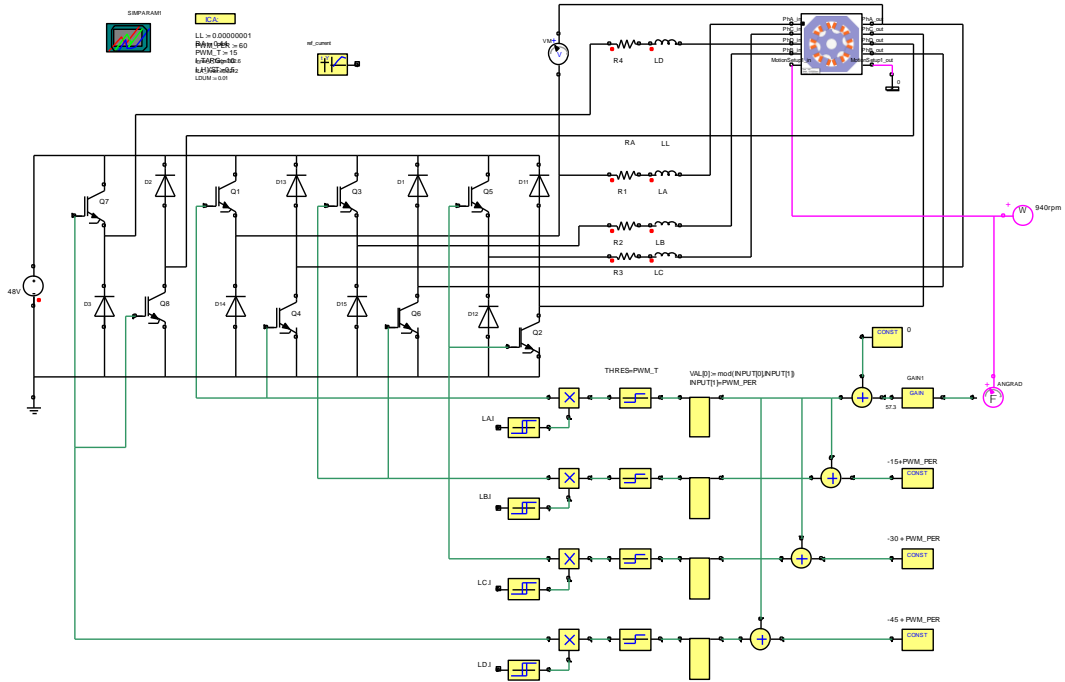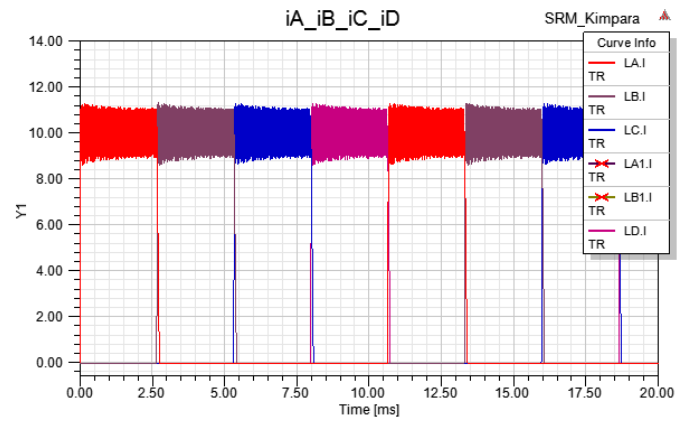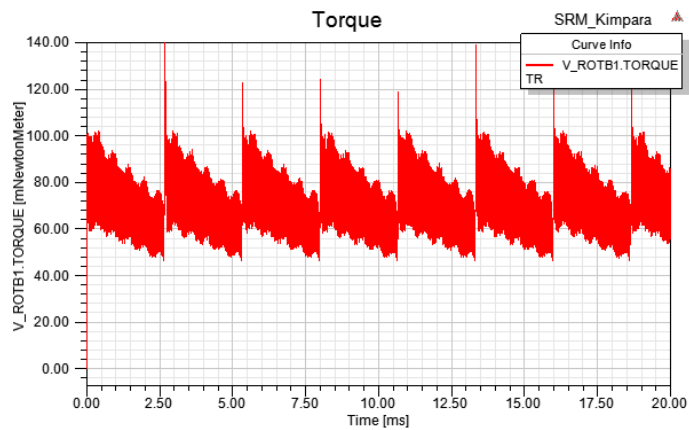Figure 5.2. SRM drive co-simulation.

Figure 5.3. Conventional excitation. (a) Phase currents. (b) Generated torque.

(a)

(b)

Figure 5.4. Optimization routine.
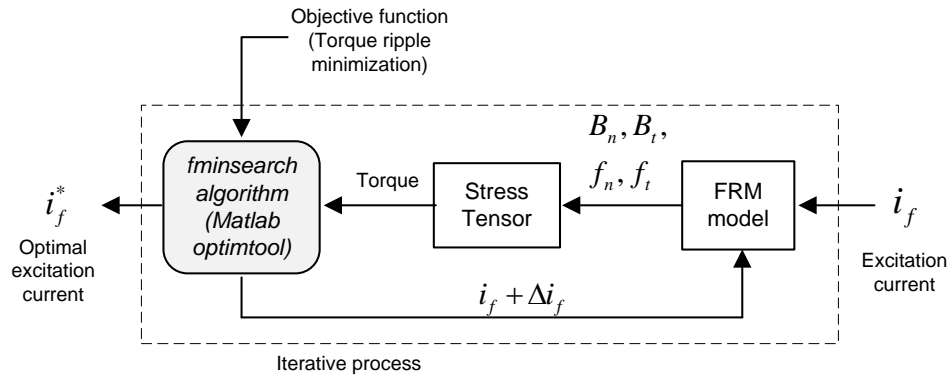
At a specific rotor position, a current excitation value is tested in the field reconstruction model and the torque is estimated. Later, a small perturbation is applied in the excitation current value and the torque is re-calculated and compared to the former value to check which current value is more beneficial. In each step, the optimal current value is the one that better satisfy the objective function:

$$f(i) = (T - T_{av})^2 \tag{5.3}$$

where T is the calculated torque in each iteration and T_{av} denotes the desired load torque.

The *fminsearch* algorithm in MATLAB optimization toolbox has been used to update the current value in each iteration. This process is evaluated off-line and the fire angle and dwell angle are kept constant.

Figure 5.5 shows the outcome phase current profile computed through this method. The overall process took approximately 3 minutes to generate the optimal reference current profile. The optimized excitation illustrated in Figure 5.5 presents an expected profile. As aforementioned, as the torque naturally decreases, the current must be increased to compensate it. A similar current profile has been found in [59], [60] and [61].

5.2.1 Simulation Results

The optimized reference current obtained for 940 rpm was imported to Simplorer using a look-up table and tested in the co-simulation model. Figure 5.6 depicts the phase currents and the generated torque using the proposed current waveform at 940 rpm.

As observed, the proposed current excitation is prone to generate a smoothly torque profile in comparison with the conventional square-wave excitation.

Figure 5.5. Optimized reference current for 940 rpm, turn-on angle is 12°.

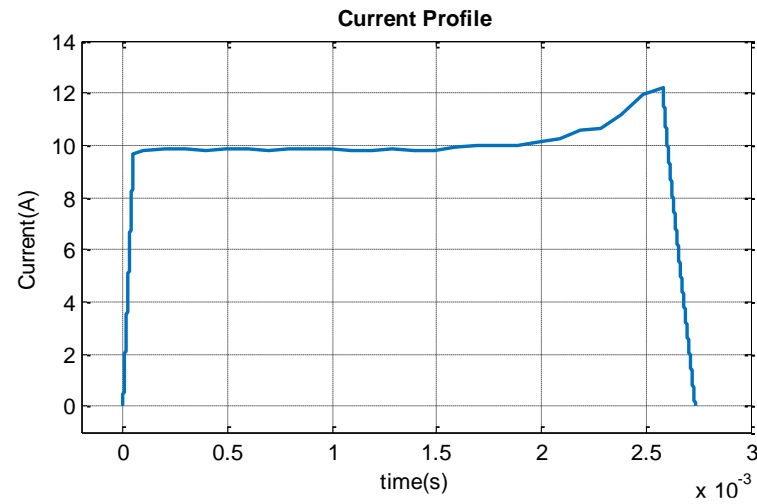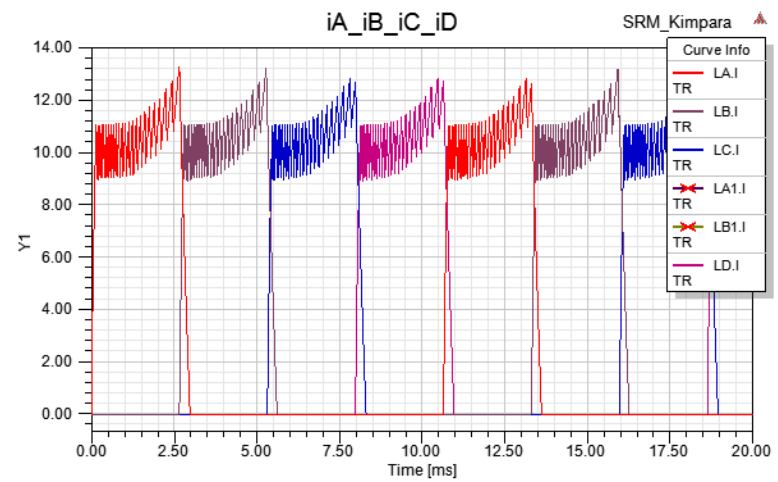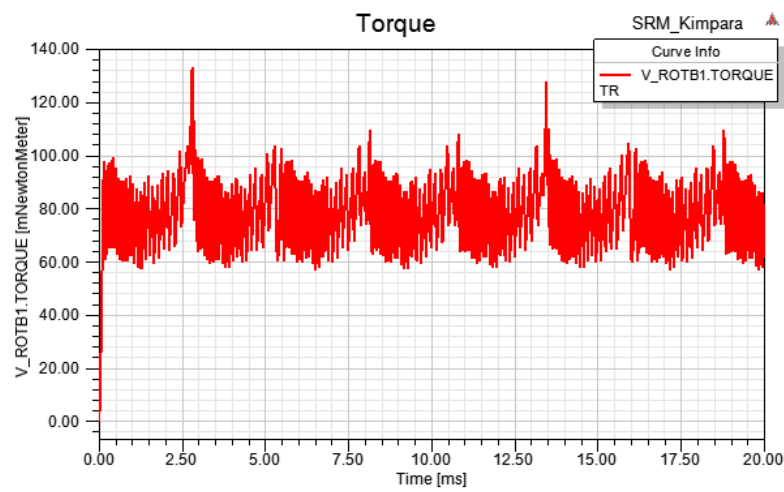Figure 5.6. Optimized excitation at 940 rpm. (a) Phase currents. (b) Generated torque.

(a)

(b)

5.2.2 Experimental implementation

The torque ripple mitigation was also confirmed experimentally. The test bench configuration is similar to that showed in Figure 4.40, with the torquemeter installed between the motor and the load (PMDC). The running speed was set to approximately 160 rpm because dynamic measurement of torque needs to be accomplished at very low speed due to the torque sensor bandwidth and also to reduce the impact of the mechanical coupling in the drive train. The load torque is aproximately 0.34 Nm.

Figure 5.7 shows the oscilloscope screenshot for the traditional square-wave current excitation. The torque measurement is the green signal. The same speed and load condition are used to test the optimized current excitation. Figure 5.8 depicts the results. As noticeable, the proposed current profile is capable of minimize the torque ripple successfully. Please, note that only the reference value is changing, the hysteresis limits are the same (uniform band). Quantitatively, expression (5.2) was used to compute the oscillation reduction from aproximately 60% (conventional) to 15% (optimized).

Analyzing the torque generated by an 8/6 SRM one can note 24 pulses per revolution (6 electric cicles and 4 phases). It means that the torque pulsations occur at a frequency 24 times higher than the frequency of rotation. For the tested speed of 160 rpm, torque profile exhibits non-zero components for orders multiple of 64 Hz. Figure 5.9 shows the comparison between the harmonic spectrum of the torque signal before and after optimization. As can be observed, the first component has been largelly reduced. The DC component was omitted to highlight the ripple components.

Figure 5.7. Oscilloscope screenshot using conventional excitation at 160rpm and 0.34 N.m.
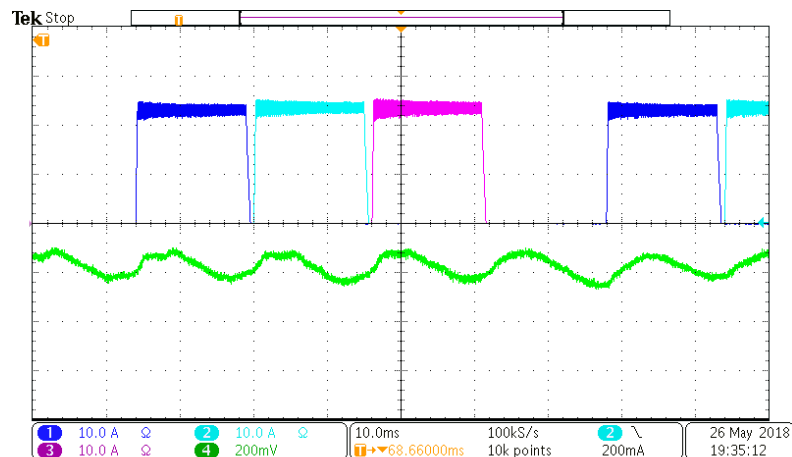
Figure 5.8. Oscilloscope screenshot using optimized excitation at 160rpm and 0.34 N.m.
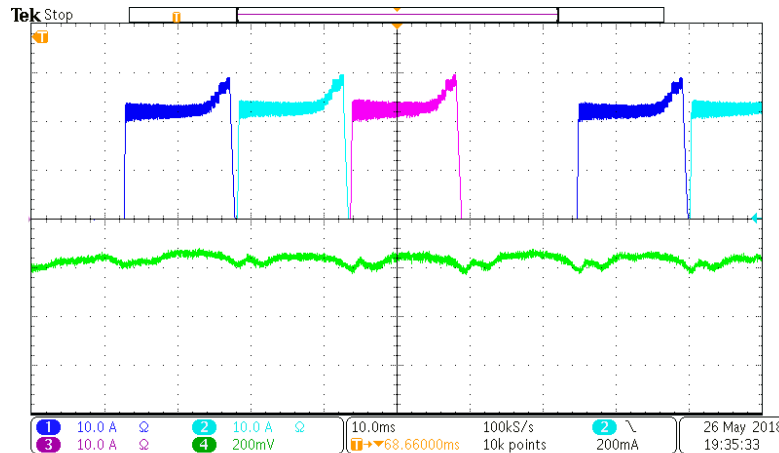
Figure 5.9. Comparison of the torque signal in frequency domain.
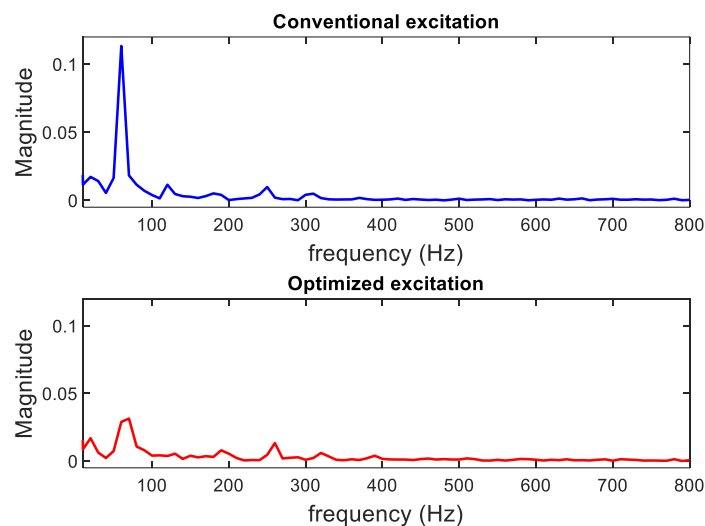
The proposed algorithm was also employed to obtain the current profile that mitigates the torque oscillation for another condition. In Figure 5.5 the turn-on angle was 12° and the excitation applied at this position will produce a reasonable amount of torque, please refer to the static torque profile. Therefore, the current was increased only close to the turn-off angle (27°) to compensate the drop in the torque generated. In the next test, the turn-on angle was choose to be smaller, around 5°.

Thus, the optimization routine given in Figure 5.4 has provided the current profile showed in Figure 5.10 for this new condition, at 80 rpm and load approximately 0.38 Nm. Once more, the current shape looks reasonable. At this turn-on angle, the developed torque is low, requiring a high current value to produce a value close to the desired one and, hence minimize

the torque ripple. Close to the turn-off angle, a similar analysis given in the previous study case, is applied.

Figure 5.11 illustrates the comparison between the experimental currents and torque using conventional hysteresis control and the optimized current shape. The ripple is clearly reduced.

Figure 5.10. Optimized reference current for 80 rpm, turn-on angle is 5°.
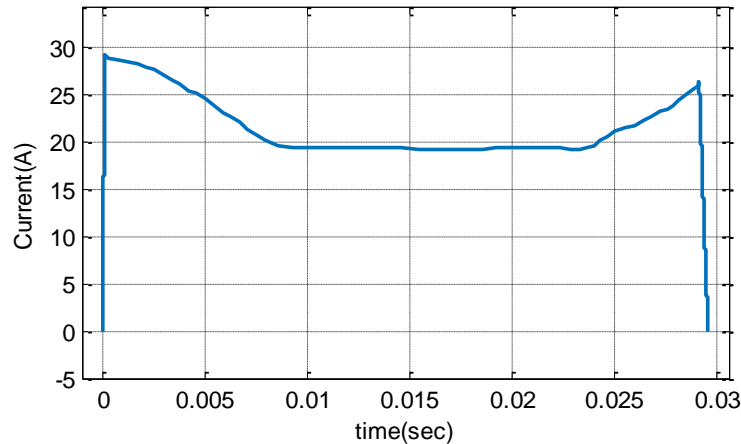
Although the torque ripple minimization has been observed, the proposed current shape in both cases might have a negative impact in the structural vibration. It is because the commutation occurs in the vicinity of alignment and, accordingly, the current was increased at this region to compensate the torque dropping. However, the radial forces exhibit its maximum value in the same region. Since the radial force is considered the main source of SRM vibration, the optimal current profile to improve the output torque will result in higher vibration and acoustic noise. Indeed, Figure 5.12 shows the vibration measurement before and after the torque optimization for the first studied case and confirms this fact. Likewise, Figure 5.13 also attests a higher vibration when the proposed excitation is applied for the second operational condition. However, it is important to mention that, in the latter case, since the turn-on angle is at 5°, the radial force component is low (misalignment) and the high current amplitude near the beginning of conduction does not affect the vibration.

In general, noise sensitive applications will be affected by the proposed currents profile, therefore in the following section an alternative mechanism to avoid the vibration increasing is presented.

Figure 5.11. Current and torque measurements at 80 rpm and 0.38 Nm. (a) Conventional excitation. (b) Optimized excitation.
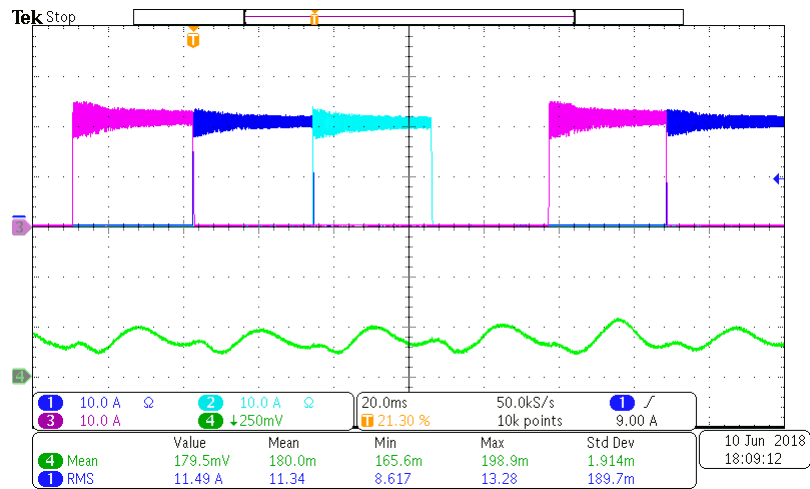
(a)
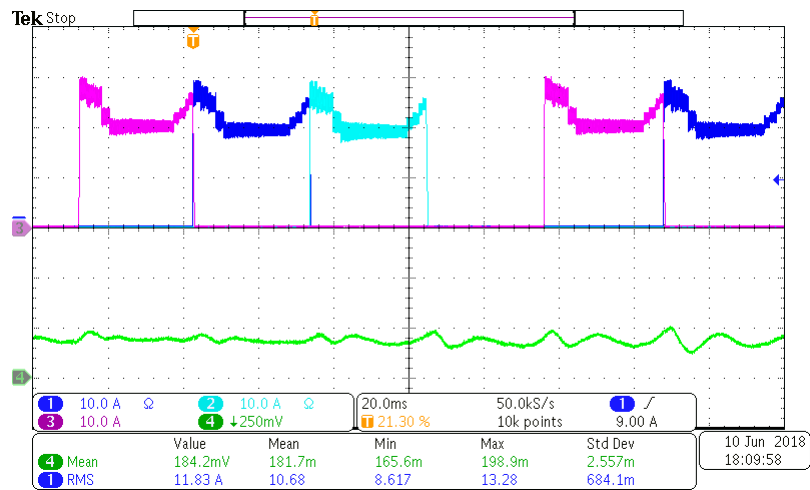
(b)

Figure 5.12. Vibration measurement at 160 rpm. (a) Conventional excitation. (b) Optimized excitation for smooth torque generation.
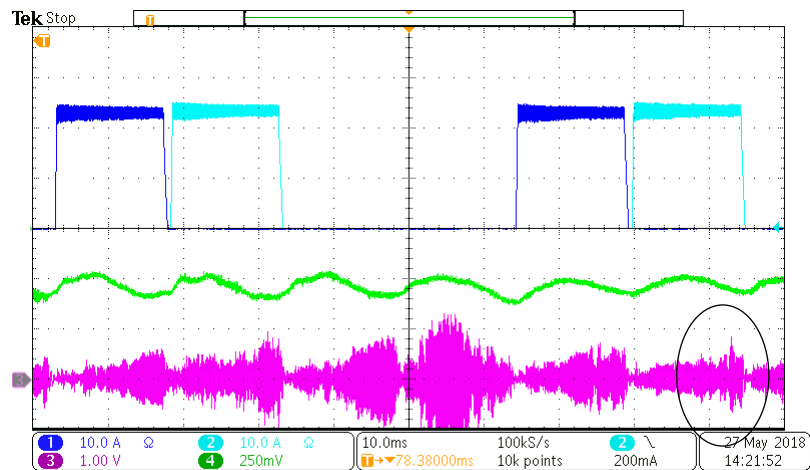
(a)
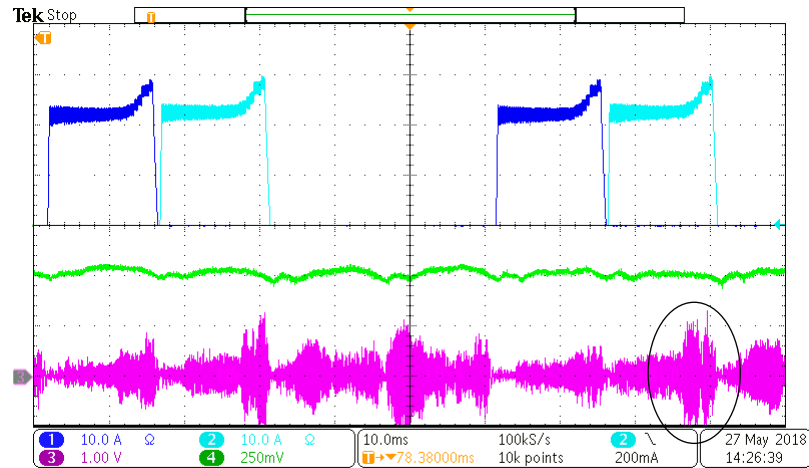
(b)

Figure 5.13. Vibration measurement at 80 rpm using optimal current excitation.
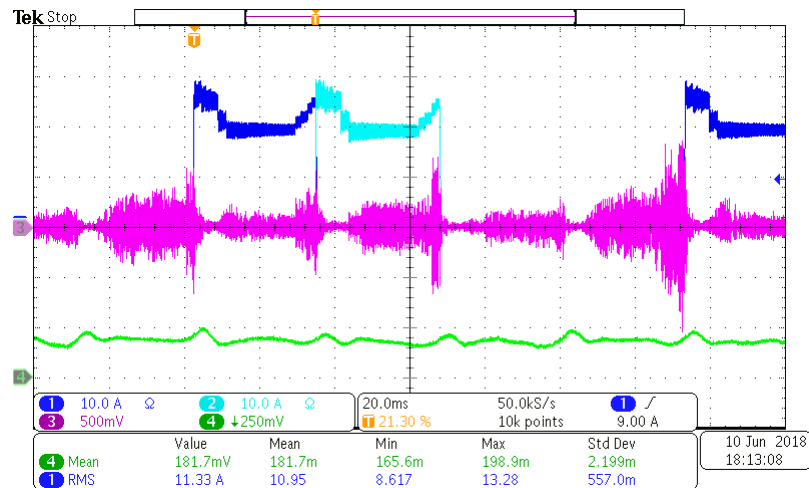
5.3 Torque and vibration optimization

It has been observed in the previous section that the torque optimization leads to a worse vibration response. However, in Chapter 4, a vibration reduction has been achieved by introducing the active cancellation in the switchings. Therefore, one possible solution for the vibration and torque issues in SRM drives is to combine both strategies, i.e., the active vibration cancellation will be incorporated in the current profile that minimizes the torque pulsation.

For simplicity, instead of tuning each single switching, herein, a variable hysteresis band is proposed. Basically, the region where vibration has been increased (within the conduction period) will be divided in small sections and an optimization routine will be developed to define the current band that introduces the vibration cancellation effect. This methodology has been

inspired by experimental observations and the tests conducted in [49], where a particle swarm optimization was applied to define different bands along the conduction period.

To search for the optimal hysteresis band, a new MATLAB routine is developed. The vibration prediction model based on MIR is, again, the key factor to compute the vibration according to the hysteresis band tested. The optimization process consists in test an initial current band (b_1) in the region $\Delta\theta_r^1$ showed in Figure 5.14. The resulting vibration is calculated in this interval and then, the *fminsearch* algorithm of MATLAB *optimtool* toolbox introduces a small perturbation in b_1 and the vibration is re-calculated and compared with the former estimated signal. The band value that produces lower overall vibration, i.e. the value that mostly accommodate active cancellation, is chosen. The same procedure is repeated over the other regions ($\Delta\theta_r^2$, $\Delta\theta_r^3$, ...) until the best current band is defined for each interval. Each region took in average around 1.2 minutes to be completed. Table 5.1 shows the calculated current bands.

After the whole optimization, the obtained current profile is shown in Figure 5.15. To validate the proposed current excitation, a comparison between the conventional waveform (flat-top current), the current profile after the torque optimization (Figure 5.5) and the final current profile with the adjustable hysteresis band (Figure 5.15) was analyzed experimentally, as showed in Figure 5.16. Please, note that with conventional excitation, the torque signal (green) presents an oscillation and the vibration (magenta) is normally increased as the rotor moves towards the alignment with stator pole. After the first optimization, the torque oscillation is reduced however the vibration is higher when compared to the conventional case. Finally, after the hysteresis band optimization, the proposed excitation provides simultaneously improvement with low torque ripple and reduced vibration operation.

Figure 5.14. Region of interest divided in small intervals.
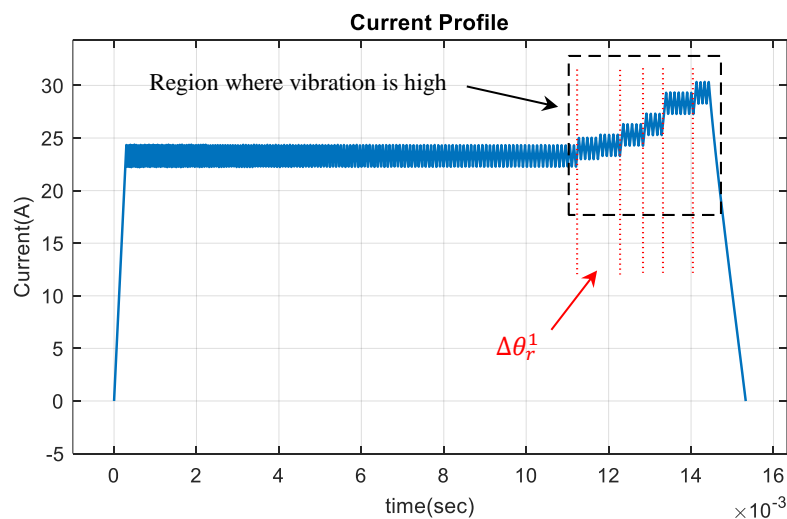
Figure 5.15. Optimized current profile for torque ripple and vibration mitigation at 160 rpm.
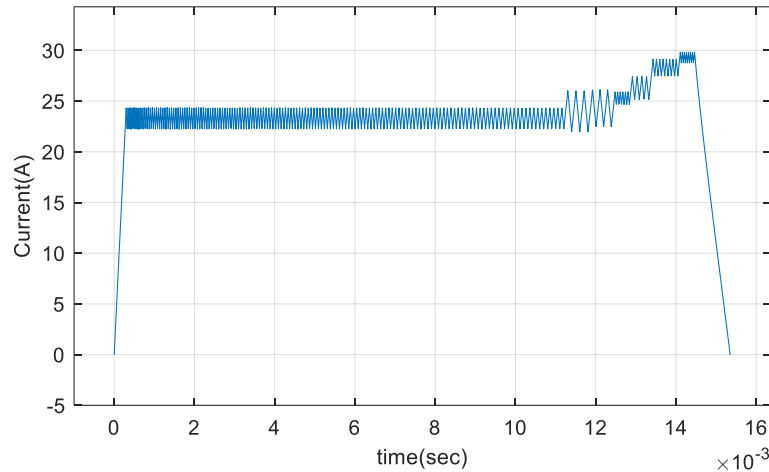
Table 5.1. Optimized hysteresis band according to the regions.

b_1	b_2	b_3	b_4	b_5
2.05	0.95	1.85	1.41	1.12

Figure 5.17 shows the experimental results for the motor running at 160 rpm after the combined (torque and vibration) optimization is performed. One can observe that the negative impact of the increasing in current amplitude has been attenuated by the variable hysteresis band. Figure 5.18 shows the comparison of the measured acceleration in the frequency domain considering the excitation after the torque optimization and the current profile with adjusted hysteresis band. The component around 2kHz is the first mode of vibration, according to what was found in Chapter 4, and it is noticeable reduced. The vibration improvement in the wide range of frequency is evaluated through eq. (4.11), which gives about 37% reduction in vibration energy when using the variable hysteresis band. Therefore, it has been demonstrated that the proposed strategy is prone to reduce the magnitude of acceleration, hence, mitigating the undesirable effects of noise.

Figure 5.16. Torque ripple and vibration comparison. (a) Conventional square-wave current excitation with uniform hysteresis band. (b) Optimized excitation for torque ripple reduction with uniform hysteresis band. (c) Current profile for simultaneous torque ripple
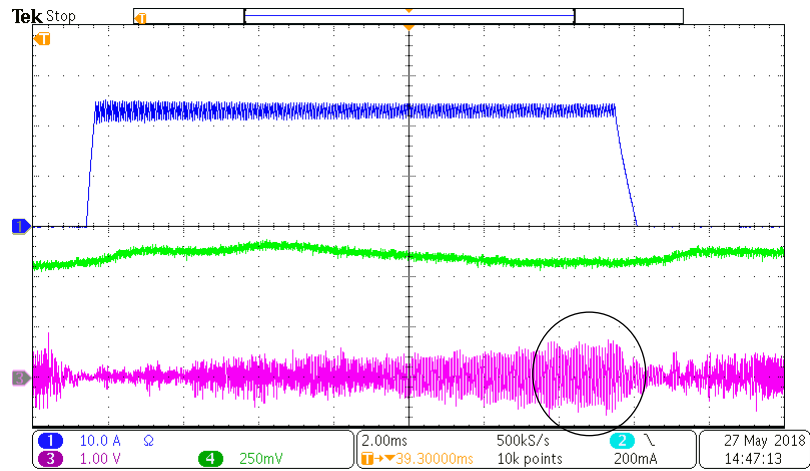
(a)
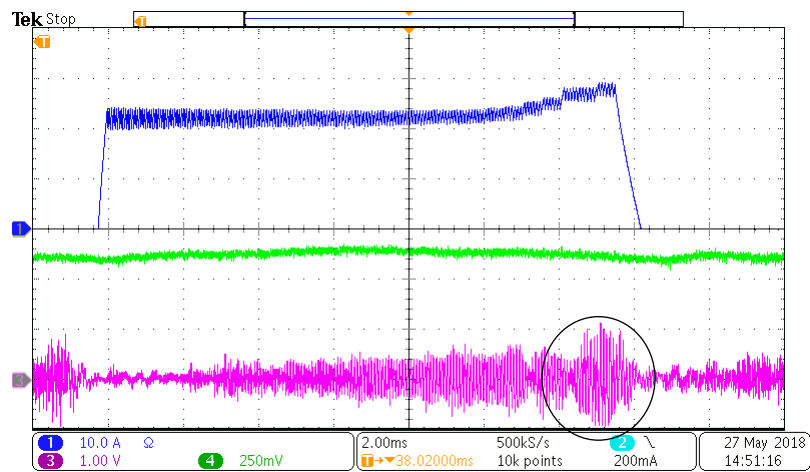
(b)
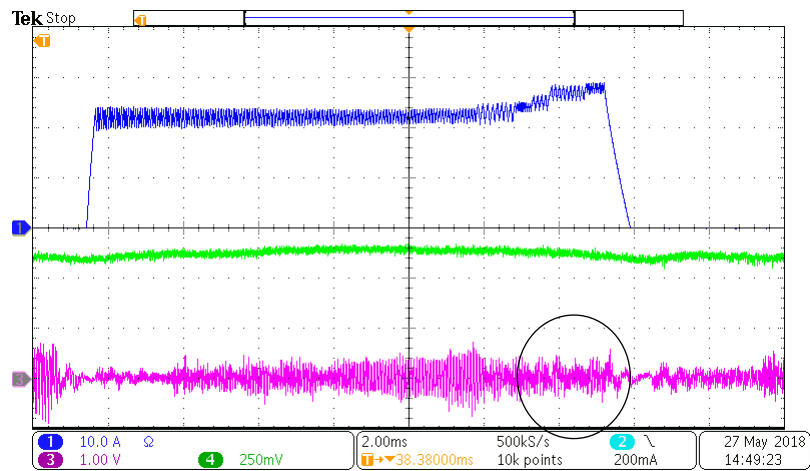
(c)

Figure 5.17. Torque and vibration performance due the proposed current profile at 160 rpm and 0.34 Nm.
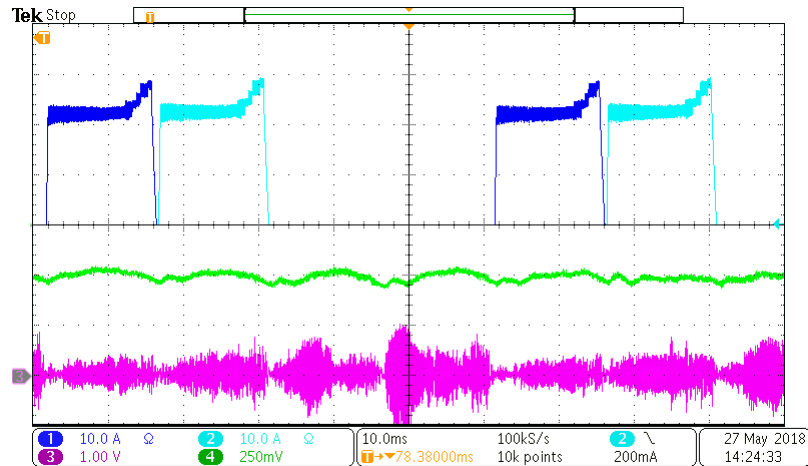
Figure 5.18. Comparison of the measured acceleration in frequency domain applying the excitation for optimized torque profile and the excitation with the adjustable hysteresis band for simultaneous torque and vibration optimization.
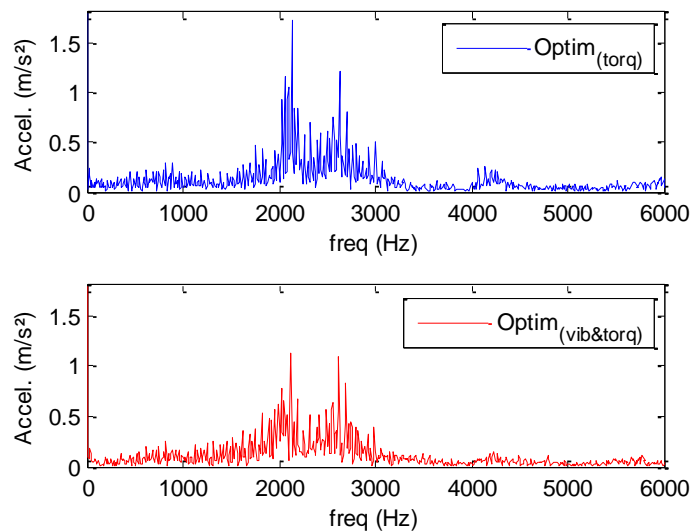
A similar optimization process has been conducted considering the case with small turn-on angle. Figure 5.19 shows the current profile after the optimization in the hysteresis band (only close to the turn-off angle). Figure 5.20 shows the comparison between the vibration measured when the SRM is excited with the current profile that minimizes the torque oscillation, however, using a uniform hysteresis band and the current with variable band (optimized values).

Figure 5.21 shows the oscilloscope screenshot for the SRM operating at 80 rpm and 0.38 Nm excited with the optimized current. A comparison of Figure 5.21 with Figure 5.11(a) and Figure 5.13 gives evidence that the torque ripple and vibration have been simultaneously

mitigated.

Figure 5.19. Optimized current profile for torque ripple and vibration mitigation at 80 rpm.
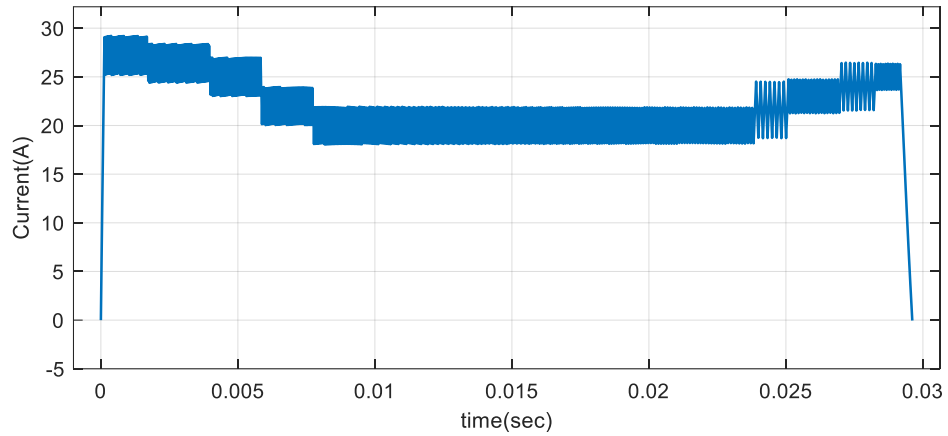
Figure 5.20. Comparison between the vibration measured according to the excitation profile. (a) Torque optimization. (b) Torque and vibration optimization.
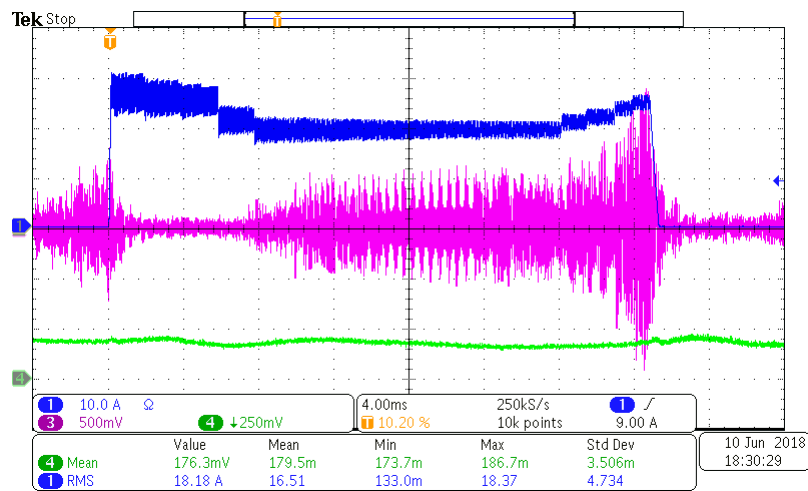
(a)
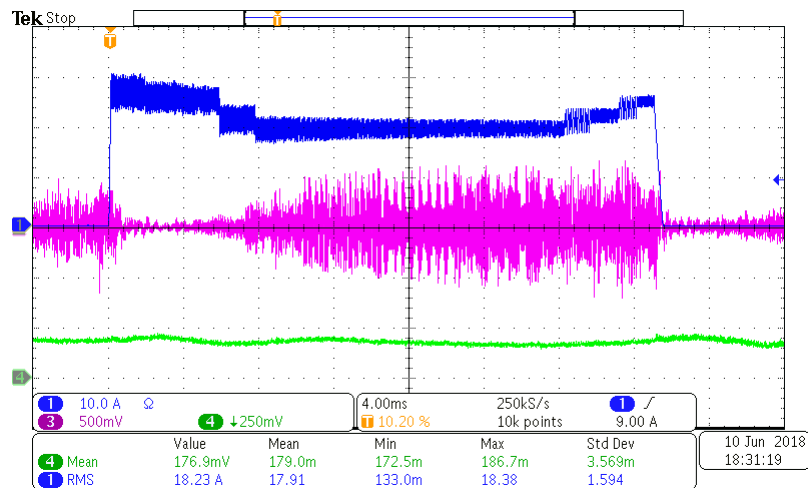
(b)

Figure 5.21. Torque and vibration performance due the proposed current profile at 80 rpm and 0.38 Nm.
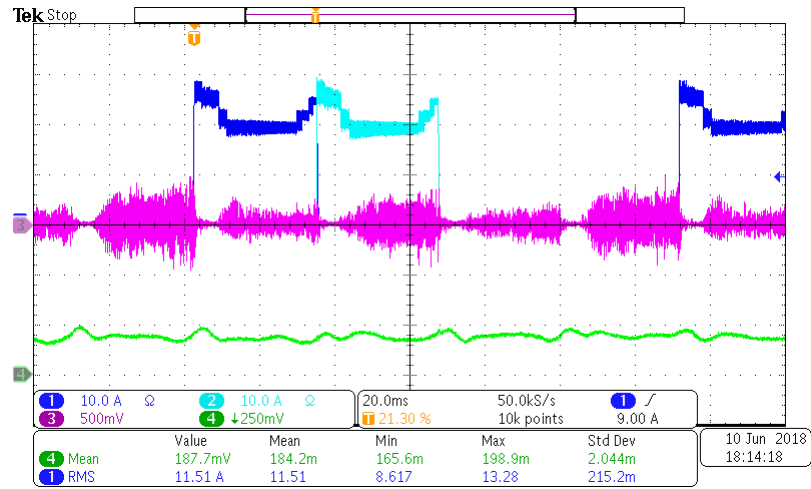
Chapter 6

Final Considerations

6.1 Conclusions

The physical principle of operation behind the switched reluctance motor allows a simple structure construction which gives it many attractive advantages. Nonetheless, the inherence operation is also responsible for torque pulsation and high acoustic noise level, considered the primary disadvantages of this motor. Requirements for motors are getting stricter. Vibration and noise become important metrics for many applications. Likewise, smooth torque generation is a desired characteristic in high performance drives.

Acoustic noise and vibration are considered a byproduct of the electromechanically energy conversion, thus in this research the active cancellation has been proposed, instead of trying to avoid it. An alternative switching pattern was designed to incorporate the AVC in every single switching. The method is valid for the low speed region. The experimental results showed a substantial reduction in stator vibration which is also helpful for acoustic noise reduction. Although the proposed switching instants yields a non-uniform current profile, it was found that the torque per Ampere is barely affected.

The torque ripple issue is also addressed considering the current profiling. In a first glance, the torque can be improved only adjusting the reference current according to static torque characteristic and the turn-on angle, however, after investigating the vibration using this methodology is was found that vibration has been increased. To deal with this shortcoming the hysteresis band is optimized to also incorporate some active cancellation. The outcome is a current profile optimized to this multi-objective problem, i.e., an excitation that simultaneously mitigates the torque ripple and vibration levels.

6.2 Future development

In this research new control strategies have been presented and opened the doors for further investigations based on the achievements reached. The history of SRM development has not been a continuous one. After a long period in background, the inherent advantages and potentials of the SRM drive have been recently investigated and explored. Yet, there is still a

lot that can be done in the design and control of the drive. As SRM has been treated as a potential candidate for many modern applications, research on vibration and noise as well as torque ripple tends to be kept hot for many years.

Hence, the contributions of this work can be extended through:

- Model improvements: The optimization routine uses a current estimation based on some inductance profile obtained experimentally and interpolated for other currents and rotor positions; thus, the resolution of the curves can be improved if new experiments are carried out. Likewise, the vibration prediction model uses MIR obtained with 1 mechanical degree as resolution, and can also be improved by extra experimental means;

- Saturation effects in the MIR: The saturation effect can be included in MIR to obtain a complete model over the wide range operation;

- Selective frequency cancelation: The optimization routine attempts to minimize the overall stator vibration; however, the switching instants can be designed focusing in the cancelation of a specific frequency component.

- Improve the optimization process: the best instant for switch has been defined through exhaustive search algorithm, however a more effective search mechanism based on artificial intelligence techniques may be considered;

- Insert the zero-voltage stage: the results are presented for the hard-chopping control, nonetheless, the incorporation of soft-chopping is also possible. Soft-switching will induce lower vibration because the step voltage is half of that applied in hard-chopping, hence, intercalating these controls, an optimized vibratory behavior can be reached;

- The insertion of the turn-on and turn-off angles in the optimization's routine: The algorithms developed to mitigates the vibration and torque ripple might include the optimization of turn on and off angles;

- In the hysteresis band optimization, a different number of regions need to be tested: The number of regions where the hysteresis band has been optimized can be increased. The

expectation is that with a higher number of optimal bands, better is the vibration response, once, more cancellation is experienced.

- The parameter t_{max} used as constrain to avoid torque ripple during the switching instants design must be optimized: In this research, this parameter was obtained by attempt and trial in simulations, however a relationship between current variation allows for an optimization procedure;

References

[1]   T. J. E. Miller, Switched Reluctance Motors and Their Control, Press Oxford, 1993.

[2]   B. Deepa e V. K. Jogi, "Brief History of Switched Reluctance Motor," *Journal of Electrical and Electronics Engineering (IOSR-JEEE),* vol. 13, nº 1, 2018.

[3]   R. Krishnan, Switched reluctance motor drives: modeling, simulation, analysis, design and applications, CRC Press LLC, 2001.

[4]   P. J. Lawrenson, J. M. Stephenson, P. T. Blenkinsop, J. Corda e N. N. Fulton, "Variable-speed Switched Reluctance Motors," em *Proc. IEEE*, 1980.

[5]   J. V. Bryne, J. B. O'Dwyer e M. F. McMullin, "A high performance variable reluctance drive: a new brushless servo," em *Motorcon Proceedings*, 1985.

[6]   S. A. Nasar, "DC Switched Reluctance Motor," *Proceeding IEEE,* vol. 116, nº 6, 1969.

[7]   M. Moallem, "Performance characteristics of switched reluctance motor drive," Purdue University, 1989.

[8]   A. Ahmad, High Performance AC Drives Modelling Analysis and Control, Springer, 2010.

[9]   V. Bernardeli, "Controle de Conjugado em Motores a Relutância Variável Multifásicos," Federal University of Uberlândia, 2008.

[10] R. J. Dias, "Motores a Relutância Variável 6x4 e 6x6 Estudo Comparativo de Operação e Desempenho," 2011.

[11] T. Skvarenina, S. Pekarek, O. Wasynczuk, P. Krause, R. Thibodeaux e J. Weimer, "Simulation of a switched reluctance, More Electric Aircraft power system using a graphical user interface," em *Energy Conversion Engineering Conference*, 1997.

[12] N. S. G. Gonçalves, "Tolerância a Falhas em Motores de Relutância Variável Comutados," University of Coimbra, 2013.

[13] A. Mohamed e Y. A. Mohd, "Maximum Efficiency Operation of Switched Reluctance Motor by Controlling Switching Angles," em *IEEE Power Electronics and Drive Systems*, 1997.

[14] J.-W. Ahn, "Switched Reluctance Motor," Kyungsung University Korea.

[15] D. Cameron, J. H. Lang e S. Umans, "The origin and reduction of acoustic noise in doubly salient variable-reluctance motors," *IEEE Trans. on Industry Applications,* vol. 28, nº 6, pp. 1250-1255, 1992.

[16] C. Pollock e C. Y. Wu, "Acoustic noise cancellation techniques for switched reluctance drives," *IEEE Trans. Industrial Applications,* vol. 33, nº 2, pp. 477-484, 1997.

[17] M. Elamin, Y. Yasa, Y. Sozer, J. Kutz, J. Tylenda e R. L. Wright, "Effects of window in stator and rotor poles of switched reluctance motors in reducins noise and vibration," em *IEEE International Electric Machine Drives Conferece*, 2017.

[18] H. Y. Yang, Y. C. Lim e H. C. Kim, "Acoustic noise/vibration reduction of a single-phase SRM using skewed stator and rotor," *IEEE Tans. Industrial Electronics,* vol. 60, nº 10, pp. 4292-4300, 2013.

[19] K. Edamura e I. Miki, "Design of stator and rotor for noise reduction of SRM," *IEEE International Conference on Electrical Machines and Systems,* 2014.

[20] B. Fahimi, G. Suresh e M. Ehsani, "Design considerations of switched reluctance motors: vibration and control issues," em *IEEE Industry Applications Conference*, 1999.

[21] J. B. Bartolo e C. Gerada, "The electromagnetic design of a high speed, 45kW, switched reluctance machine having a novel rotor geometry for aerospace application," em *International Conference on Electrical Machines (ICEM)*, 2014.

[22] G. Li, J. Ojeda, S. Hlioui, E. Hoang, M. Lecrivain e M. Gabsi, "Modification in Rotor Pole Geometry of Mutually Coupled Switched Reluctance Machine for Torque Ripple Mitigating," *IEEE Trans. on Magnetics,* vol. 48, nº 6, pp. 2025-2034, 2012.

[23] D. H. Lee, T. H. Pham e J. W. Ahn, "Design and Operation Characteristics of Four-Two Pole High-Speed SRM for Torque Ripple Reduction," *IEEE Trans. Industrial Electronics,* vol. 60, nº 9, pp. 3637-3643, 2013.

[24] A. Sheikhi, H. Oraee, S. Kaboli e M. Dorkhah, "A new configuration of switched reluctance motor for reducing the torque ripple," em *International Conference on Electric Power and Energy Conversion Systems (EPECS)*, 2009.

[25] B. Fahimi, G. Suresh, K. M. Rahman e M. Ehsani, "Mitigation of acoustic noise and vibration in switched reluctance motor drive using neural network based current profiling," em *IEEE Industrial Appl. Annual Meeting*, 1998.

[26] A. Ahn e D. Lee, "Hybrid excitation of SRM for reduction of acoustic noise and vibration," *IEEE Trans. Industrial Electronics,* vol. 51, nº 2, pp. 374-380, 2004.

[27] M. Takiguchi, H. Sugimoto e A. Chiba, "Acoustic noise and vibration reduction of SRM by elimination of third harmonic component in sum of radial forces," *IEEE Trans. on Energy Conversion,* vol. 30, nº 3, pp. 883-891, 2015.

[28] X. Mininger, E. Lefeuvre, M. Gabsi, C. Richard e D. Guyomar, "Semiactive and active piezoelectric vibration controls for switched reluctance machine," *IEEE Trans. on Energy Conversion,* vol. 23, nº 1, pp. 78-85, 2008.

[29] A. Shahabi, A. Rashidi e S. M. Saghaian-Nejad, "Torque ripple reduction of SRM drives below the base speed using commutation angles control," em *Iranian Conference on Electrical Engineering (ICEE)*, 2013.

[30] J. Gribble, P. Kjaer, C. Cossar e T. Miller, "Optimum Commutation Angles for Current Controlled Switched Reluctance Motors," em *6th Conference on Power Electronics and Variable Drives*, 1996.

[31] I. Husain e M. Ehsani, "Torque ripple minimization in switched reluctance motor drives by PWM current control," *IEEE Trans. on Power Electronics,* vol. 11, nº 1, pp. 83-88, 1996.

[32] D. Schramm, B. Williams e T. Green, "Torque ripple reduction of switched reluctance motors by PWM phase current optimal profiling," em *PESC*, 1992.

[33] Y. Cai e C. Gao, "Torque Ripple Minimization in Switched Reluctance Motor Based on BP Neural Network," em *IEEE Conference on Industrial Electronics and Applications*, Harbin, 2007.

[34] J. Lei, F. L. Wang, H. Deng e D. Miao, Emerging Research in Artificial Intelligence and Computational Intelligence, Springer, 2012.

[35] L. Henriques, L. Rolim, W. Suemitsu, P. Branco e J. Dente, "Torque ripple minimization in a switched reluctance drive by Neuro-Fuzzy compensation," *IEEE Trans. on Magnetics,* vol. 36, nº 5, pp. 3592-3594, 2000.

[36] C. Y. Wu e C. Pollock, "Analysis and reduction of acoustic noise in the switched reluctance drive," *IEEE Trans. Industrial Applications,* vol. 31, nº 1, pp. 91 - 98, 1995.

[37] D. G. Manzer, M. Varghese e J. S. Thorp, "Variable reluctance motor characterization," *IEEE Trans. on Industrial Electronics,* vol. 36, nº 1, pp. 55-63, 1989.

[38] Z. Lin, D. S. Reay e B. Zhou, "Experimental measurement of switched reluctance motor non-linear characteristics," em *Industrial Electronics Society Conference - IECON*, Vienna, 2013.

[39] A. D. Cheok e N. Ertugrul, "Computer-based automated test measurement system for determining magnetization characteristics of switched reluctance motor," *IEEE Trans. on Instrumentation and Measurement,* vol. 50, nº 3, pp. 690-696, 2001.

[40] W. Zhu, B. Fahimi e S. Pekarek, "A field reconstruction method for optimal excitation of permanent magnet synchronous machines," *IEEE Trans. on Energy Conversion,* 2006.

[41] D. Wu, S. Pekarek e B. Fahimi, "A Field Reconstruction Technique for Efficient Modeling of the Fields and Forces Within Induction Machines," *IEEE Trans. on Energy Conversion,* vol. 24, nº 2, pp. 366-374, 2009.

[42] M. L. M. Kimpara, B. Fahimi, L. E. B. Silva, P. E. M. J. Ribeiro, R. B. Godoy e J. O. P. Pinto, "A new synchronous machine modeling using the field reconstruction method," *Journal of Control, Automation and Electrical Systems,* vol. 25, 2014.

[43] M. L. M. Kimpara, B. Fahimi, P. E. M. J. Ribeiro, R. Godoy, J. O. P. Pinto e L. E. B. Silva, "Field reconstruction method applied for harmonic voltage mitigation in salient pole synchronous generators," em *Brazilian Power Electronics Conference*, Gramado, 2013.

[44] C. Lin, W. Wang, M. McDonough e B. Fahimi, "An Extended Field Reconstruction Method for Modeling of Switched Reluctance Machines," *IEEE Trans. on Magnetics,* vol. 48, nº 2, pp. 1051-1054, 2012.

[45] P. Pillay e W. Cai, "A investigation into Vibrations in Switched Reluctance Motors," *IEEE Trans. on Industry Applications,* vol. 35, nº 3, 1999.

[46] Agilent technologies, "The Fundamentals of Modal Testing - Application note 243".

[47] T. D. Rossing, Handbook of Acoustics, Springer, 2007.

[48] Prosig, Noise & Vibration measurement Handbook.

[49] S. Wang, "VIbration Analysis and Mitigation in Switched Reluctance Machine Drives," University of Texas at Dallas, 2017.

[50] T. Zhangjun, P. Pillay, A. M. Omekanda, C. Li e C. Cetinkaya, "Young's modulus for laminated machine structures with particular reference to switched reluctance motor vibrations," *IEEE Trans. Industrial Application,* vol. 40, nº 3, pp. 748-754, 2004.

[51] A. Saito, Y. Nishikawa, S. Yamasaki, K. Fujita, A. Kawamoto, M. kuroishi e H. Nakai, "Equivanlent orthotropic elastic moduli identification method for laminated electrical steel sheets," *Elsiever Mechanical Systems and Signal Processing,* pp. 607-628, 2016.

[52] M. van der Giet, K. Kasper, R. W. De Doncker e K. Hameyer, "Material parameters for the structural dynamic simulation of electrical machines," em *International Conference on Electrical Machines*, Marseille, 2012.

[53] J. Sun, H. Feng e C. Zhu, "Identification of Laminated Core and Winding's Physical Parameters by Stator's Modal Testing," em *International Conference on Electrical Machine and Systems (ICEMS)*, Hangzhou, 2014.

[54] W. Cai, P. Pillay e Z. Tang, "Impact of Stator Windings and End-Bells on Resonant Frequencies and Mode Shapes of Switched Reluctance Motors," *IEEE Trans. Industrial Applications,* vol. 38, nº 4, pp. 1027-1036, 2002.

[55] C. Lin, "Analysis and mitigation of vibration and acoustic noise in switched reluctance machines," University of Texas at Dallas, 2013.

[56] C. Lin e B. Fahimi, "Prediction of radial vibration in switched reluctance machines," *IEEE Trans. on Energy Conversion,* vol. 28, nº 4, pp. 1072-1081, 2013.

[57] M. Van der Giet, E. Lange, D. Correa, I. Chabu, S. Nabeta e K. Hameyer, "Acoustic simulation of a special switched reluctance drive by means of field–circuit coupling and multiphysics simulation," *IEEE Trans. on Industrial Electronics,* vol. 57, nº 9, pp. 2946-2953, 2010.

[58] A. Kolli, G. Krebs, X. Mininger e C. Marchand, "Impact of command parameters on efficiency, torque ripple and vibrations for switched reluctance motor," em *International Conference on Electric Machines IECM*, 2012.

[59] M. L. M. Kimpara, P. M. J. Ribeiro, J. O. P. Pinto, D. Andrade, B. Fahimi, L. E. B. Silva, B. Ozpineci e M. Kiani, "Improvement in torque profile of switched reluctance motors," em *IEEE International Symposium on Industrial Electronics (ISIE)*, 2017.

[60] C. Lin e B. Fahimi, "Reduction of Torque Ripple in Switched Reluctance Motor Drives using Field Reconstruction Method," em *Vehicle Power and Propulsion Conference (VPPC)*, Chicago, 2012.

[61] Z. Lin, D. S. Reay, B. W. Williams e X. He, "Torque Ripple Reduction in Switched Reluctance Motor Drives Using B-Spline Neural Networks," *IEEE Trans. on Industrial Applications,* vol. 42, nº 6, pp. 1445-1453, 2006.

APPENDIX I

DSP code

The following code lines are part of the main and main_isr functions.

```c
#include "F28x_Project.h"
#include<math.h>
#include "Declaration.h"

ADC_Results SMC_ADC=ADC_Results_Defaults;
Motor_Control SMC_Control=Motor_Control_Defaults;

// LUT – 1200 rpm
float32
Angle_PhaseA[34]={42,45.33,45.77,46.19,46.40,46.74,46.93,47.60,47.97,48.49,48.90,4
9.34,49.75,50.16,50.39,51.06,51.25,51.90,52.09,52.22,52.41,52.81,53.00,53.13,53.31
,53.67,53.84,53.97,54.34,54.74,54.96,55.31,55.47,55.80};
float32
Angle_PhaseB[34]={42,45.33,46.01,46.38,46.54,46.88,47.05,47.40,47.57,48.24,48.33,4
8.53,48.62,49.01,49.69,50.04,50.21,50.56,50.73,51.06,51.25,51.58,51.74,52.41,52.51
,52.71,52.81,53.20,53.67,54.17,54.68,55.18,55.43,55.77};
float32
Angle_PhaseC[42]={42,45.33,46.01,46.38,46.54,46.88,47.05,47.40,47.57,48.14,48.23,4
8.44,48.55,48.76,48.99,49.32,49.48,49.84,50.00,50.11,50.27,50.88,51.03,51.20,51.38
,51.75,51.92,52.09,52.22,52.39,52.56,52.89,53.08,53.25,53.42,54.04,54.21,54.36,54.
51,54.88,55.28,55.63};
float32
Angle_PhaseD[36]={42,45.33,46.01,46.34,46.58,46.91,47.10,47.50,47.62,48.11,48.20,4
8.87,49.39,49.90,50.31,50.69,50.85,51.18,51.38,51.77,51.94,52.34,52.44,52.98,53.13
,53.35,53.50,53.67,53.84,53.99,54.22,54.79,54.89,55.11,55.50,56.17};


volatile Uint16 PhaseControlA=1;
volatile Uint16 PhaseControlB=1;
volatile Uint16 PhaseControlC=1;
volatile Uint16 PhaseControlD=1;

void main(void)
{
//
// Step 1. Initialize System Control:
// PLL, WatchDog, enable Peripheral Clocks
// This example function is found in the F2837xS_SysCtrl.c file.
//
    InitSysCtrl();
    DINT;
//    memcpy(&RamfuncsRunStart,&RamfuncsLoadStart,(Uint32)&RamfuncsLoadSize);
    InitGpio();
    InitPieCtrl();
    IER = 0x0000;
    IFR = 0x0000;
    InitPieVectTable();
```

```
    ConfigureInterrupt();
    ConfigureGPIO();
    ConfigurePWM();
    ConfigureEQEP();

    ConfigureADC();
    SetupADCSoftware();
    ConfigureDAC();
    DELAY_US(10000L);

    while(SMC_ADC.Vdc<4)    //waiting for DC bus voltage to initialize position
    {
    }
    Position_Initialization(&SMC_Control);
    while(1)
    {
        sensorTemp = GetTemperatureC(AdcaResultRegs.ADCRESULT2);
    }
}
```

```
* Main_isr.c
 *
 *  Created on: Mar 3, 2018
 *      Author:  Marcio Kimpara
 *      8/6 LUT: Marcio
 */
extern float32 Angle_PhaseA[40];
extern float32 Angle_PhaseB[48];
extern float32 Angle_PhaseC[44];
extern float32 Angle_PhaseD[40];



#define Kp 0.05
//#define Tki 0.01
#define Tki 0.001

volatile float Iref_delta=0.4;


__interrupt void pwm6_isr(void)
{
    EPwm6Regs.ETCLR.bit.INT=1;
    SMC_Control.Mechanical_Angle=(float32)(0.021972656*(EQep3Regs.QPOSCNT+502.0));
    SMC_Control.Relative_Angle_A=SMC_Control.Mechanical_Angle-
(Uint16)(SMC_Control.Mechanical_Angle*0.0166667)*60.0;
    SMC_Control.Relative_Angle_B=SMC_Control.Relative_Angle_A+45.0-
(Uint16)((SMC_Control.Relative_Angle_A+45.0)*0.0166667)*60.0;
    SMC_Control.Relative_Angle_C=SMC_Control.Relative_Angle_A+30.0-
(Uint16)((SMC_Control.Relative_Angle_A+30.0)*0.0166667)*60.0;
    SMC_Control.Relative_Angle_D=SMC_Control.Relative_Angle_A+15.0-
(Uint16)((SMC_Control.Relative_Angle_A+15.0)*0.0166667)*60.0;

    SMC_ADC.Vdc=0.0336*AdcaResultRegs.ADCRESULT0;

    if(SMC_Control.Motor_Initialization_Pass==1 && SMC_Control.Motor_Run==1)
```

```
    {

//          SMC_Control.Imax=SMC_Control.Iref+Iref_delta; // Conv. Hysteresis
//          SMC_Control.Imin=SMC_Control.Iref-Iref_delta;

        if(optim==1)
        {

        if(AdcaResultRegs.ADCRESULT1<500)        // Over current protection
        {
            GpioDataRegs.GPACLEAR.bit.GPIO10=1;
            GpioDataRegs.GPACLEAR.bit.GPIO11=1;
        }
        else
        {

        if(SMC_Control.Relative_Angle_A>Angle_PhaseA[0] &&
SMC_Control.Relative_Angle_A<Angle_PhaseA[39])
        {

            if(PhaseControlA==1)
            {
                GpioDataRegs.GPASET.bit.GPIO10=1;
                GpioDataRegs.GPASET.bit.GPIO11=1;
            }
            if(SMC_Control.Relative_Angle_A<Angle_PhaseA[PhaseControlA])
            {

            }
            else
            {
                GpioDataRegs.GPATOGGLE.bit.GPIO10=1;
                GpioDataRegs.GPATOGGLE.bit.GPIO11=1;
                PhaseControlA++;
            }
        }
            else
            {
                GpioDataRegs.GPACLEAR.bit.GPIO10=1;
                GpioDataRegs.GPACLEAR.bit.GPIO11=1;
                PhaseControlA=1;
            }
        }
```

APPENDIX II

MATLAB code

The following code lines are part of the vibration estimation model and optimization routine developed in Matlab.

```matlab
% Algorithm to find instants --> Exhaustive Search

% load Impulse Response
load terminal_1_2.mat    % --> phase A

% Auxiliary calculus
w = speed*(pi/30);          % rad/s
deg_sec = speed*(360/60);   % deg/sec
t_onB = (15/deg_sec)+t_onA;
t_onC = (30/deg_sec)+t_onA;
t_onD = (45/deg_sec)+t_onA;

%% Experimental inductance
load L.mat


% PHASE_A
idA = 1;
time_a1 = t_onA;
positionA = thetaON_mech;
La = interp2(Xq,Yq,Zq,positionA,ia1,'cubic');
Vdc = Vdc_link*idA;

% first switch - current RISE estimation
index = 2;
while(ia1(index-1,1) < (i_ref+hysband))

    if positionA(index-1,1) < thetaON_mech
        ia1(index,1) = 0;
        positionA(index,1) = positionA(index-
1,1)+(step_sim*deg_sec);
        La(index,1) = 0;
        time_a1(index,1) = time_a1(index-1,1)+step_sim;
        index = index+1;
    end

    if positionA(index-1,1) >= thetaON_mech
        positionA(index,1) = positionA(index-
1,1)+(step_sim*deg_sec);
```

```matlab
        La(index,1) =
interp2(Xq,Yq,Zq,positionA(index,1),ia1(index-1,1),'cubic');
        dL_d0 = (La(index,1)-La(index-
1,1))/(positionA(index,1)-positionA(index-1,1));
        Req = Rs+(deg_sec*dL_d0);
        tau = La(index,1)/Req;
        ia1(index,1) = abs((ia1(index-1,1)*(exp(-
(step_sim/tau))))+((Vdc/Req)*(1-exp(-(step_sim/tau)))));
        time_a1(index,1) = time_a1(index-1,1)+step_sim;
        index = index+1;
    end
end
iA = ia1(end,1);
tA = time_a1(end,1);
positionA = positionA(end,1);

% PHASE A - Hard switching
impulses_1_2_n(:,round(positionA)+1).*iA.*(Vdc/Vimp)];
idA = [idA; -1];
La = interp2(Xq,Yq,Zq,positionA,iA,'cubic');

while(positionA(index-1,1) <= thetaOFF_mech)


    if iA(index-1,1)<=(i_min)  % bottom limit
        if idA(index,1)==-1
            lower_boundary = 10e-6;  % tmin
            upper_boundary = 30e-6;  % tmax
        end
        if idA(index,1)==1
            lower_boundary = 40e-6;  % tmin
            upper_boundary = 80e-6;  % tmax
        end
    end

    if iA(index-1,1)>=(i_max)  % upper limit
        if idA(index,1)==-1
            lower_boundary = 40e-6;  % tmin
            upper_boundary = 80e-6;  % tmax
        end
        if idA(index,1)==1
            lower_boundary = 10e-6;  % tmin
            upper_boundary = 30e-6;  % tmax
        end
    end


% current estimation
Vdc = Vdc_link*idA(index,1);
positionA(index,1) = positionA(index-1,1)+(dt*deg_sec);
```

```matlab
La(index,1) = interp2(Xq,Yq,Zq,positionA(index,1),iA(index-
1,1),'cubic');
dL_d0 = (La(index,1)-La(index-1,1))/(positionA(index,1)-
positionA(index-1,1));
Req = Rs+(deg_sec*dL_d0);
tau = La(index,1)/Req;
iA(index,1) = (iA(index-1,1)*(exp(-(dt/tau))))+((Vdc/Req)*(1-
exp(-dt/tau)));
tA(index,1) = tA(index-1,1)+dt;

% vibration
Vib_A =  [zeros((round(tA(index,1)*fs)),1);
impulses_1_2_n(:,round(positionA(index,1))+1).*iA(index,1).*(2
*Vdc/Vimp)];

        f(m,1) = var(Vib_A);

        if f(m,1)<=Fitness;
            Fitness = f(m,1);
        end
        m=m+1;

% current for optimal t
t_opt = inst(find(f==Fitness),1);
positionA(index,1) = positionA(index-1,1)+(t_opt*deg_sec);
La(index,1) = interp2(Xq,Yq,Zq,positionA(index,1),iA(index-
1,1),'cubic');
dL_d0 = (La(index,1)-La(index-1,1))/(positionA(index,1)-
positionA(index-1,1));
Req = Rs+(deg_sec*dL_d0);
tau = La(index,1)/Req;
iA(index,1) = (iA(index-1,1)*(exp(-
(t_opt/tau))))+((Vdc/Req)*(1-exp(-t_opt/tau)));
tA(index,1) = tA(index-1,1)+t_opt;

% vibration for optimal t
New_VibA =  [zeros((round(tA(index,1)*fs)),1);
impulses_1_2_n(:,round(positionA(index,1))+1).*iA(index,1).*(2
*Vdc/Vimp)];

Signal = [Signal;zeros((length(New_VibA)-
size(Signal,1)),size(Signal,2))]+[New_VibA;zeros((length(Signa
l)-size(New_VibA,1)),size(New_VibA,2))];

% Hard switching
    if idA(index-1,1) == 1
        idA(index,1) = -1;
    end
    if idA(index-1,1) == -1
        idA(index,1) = 1;
    end
```